NANOPARTICLE DESIGN AND NOVEL APPROACHES TO ENHANCE PHOTOTHERMAL CANCER THERAPY

by

Hayley J. S. Paholak

A dissertation submitted in partial fulfillment
of the requirements for the degree of
Doctor of Philosophy
(Pharmaceutical Sciences)
in the University of Michigan
2015

Doctoral Committee:

Professor Duxin Sun, Co-Chair
Professor Steven P. Schwendeman, Co-Chair
Professor David E. Smith
Professor Max S. Wicha

This project is particularly meaningful to me, as my maternal grandmother died at the age of 37 after a long fight with metastatic breast cancer. I know the impact that tragic loss due to cancer can have over multiple generations within a family. My grandmother didn't live long enough to raise her three children and watch them graduate high school or get married. For most of her memorable childhood my mother missed the maternal love and nurturing every child deserves. I never got to meet my grandmother, or experience the special relationship I know my friends have had with their grandmothers.

While I greatly appreciate the impact of developing novel cancer treatments to save human lives, as an animal lover I have been troubled by the extensive animal testing conducted in both rodents and non-rodents for pharmaceutical products to enter clinical trials and reach patients. It is my hope that advances in technology and methods of modeling systems of the human body will some day significantly reduce animal testing and change the process by which pharmaceuticals are approved by regulatory authorities. Here I would like to acknowledge the sacrifices of the many mice used in this project to help further the knowledge of treatment options for humans with metastatic breast cancer. I would also urge scientists to conduct animal research with as much empathy and compassion as possible and to work with programs that find homes for and rehabilitate research animals which are no longer needed for studies, such as Beagle Freedom Project.

To my family, and all those who have personally battled cancer

ACKNOWLEDGEMENTS

The number of people that have supported me throughout my life until this point is incalculable. I would like to start by thanking my advisor, Dr. Duxin Sun, for his personal and professional guidance. His encouragement brought me to the Pharmaceutical Sciences program. Under his leadership I was supported to pursue my passions to develop my own project. He taught me to be a confident, critical scientist who appreciates the value of collaboration to achieve a common goal. I would also like to thank my co-advisor Dr. Steven Schwendeman for his support and additional insight and perspective he contributed to my work.

Next I would like to thank my committee member Dr. Max Wicha, who gave me my first opportunity to participate in scientific research as a freshman in college. My experiences in his lab affirmed my dreams of pursuing cancer research and attaining a meaningful career striving to save and improve human lives. In graduate school my collaborations with his lab and his ideas regarding my project have been invaluable. To Dr. David Smith (and Dr. Mohammed El-Sayed) on my committee, thank you for your feedback to guide and shape my project. To Dr. Greg Amidon, thank you for supporting me through the navigation of the Pharmaceutical Engineering and Pharmaceutical Sciences dual master's degrees, and for offering your personal experiences in career development.

There are many wonderful faculty members from whom I gained scientific knowledge and career development opportunities. I would like to thank Dr. Henry Wang for attracting me

to the Pharmaceutical Engineering graduate program. For their support in the Pharmacological Sciences Training Program (P.S.T.P.) I would like to thank Dr. Ronald Woodard, Dr. Paul Hollenberg, and Dr. George Garcia. Of the Pharmaceutical Sciences, Pharmacology, and Chemical Engineering faculty, I would like to acknowledge Nair Rodriguez-Hornedo, Gus Rosania, Wei Cheng, Rose Feng, Ronald Holz, Yoichi Osawa, Lola Eniola, and Anna Schwendeman. Many others who have provided critical assistance in a range of daily functions and program requirements include Patrina Hardy, Gail Benninghoff, Jeanne Getty, Marisa Gies, Denise Poirier, Courtney Leblanc, Antoinette Hopper, Cherie Dotson, and Elaine Griffin. I would also like to thank the flow core staff members Aaron Robida, Mike Pihalja, and Ann Marie Deslauriers-Cox for their assistance and the knowledge they bestowed upon me.

There are many members in my lab who have throughout the years supported me with their friendship and my project with their insight and assistance. For this, I thank Jamie Connarn, Joseph Burnett, Kanokwan (Kate) Sansanaphongpricha, Xiaoqing (Lisa) Ren, Rebecca Reed, Peng Zou, Bryan Newman, Hsiu-Fang (Sarah) Lee, Yasuhiro Tsume, Feng Ni, Mike Bly, Miao He, Hebao Yuan, Ruijuan Li, Ting Zhou, Bo Wen, Chang-Ching (Albert) Lin, Mari Gasparyan, Alex Yu, Ila Myers, Miao-Chia Lo, Siwei Li, Lichao Sun, Nathan Truchan, and Yanke Yu. In particular I would like to thank Hongwei Chen, who has been outstanding as both a mentor and collaborator. His intellectual and experimental contributions have been invaluable to my project and professional growth. I would also like to especially thank Nicholas Stevers, who has provided daily assistance, day or night, for the last two years. His unwavering enthusiasm and exceptional work ethic have not only significantly contributed to the successes of this project but have also been truly inspiring.

I would like to acknowledge the many people who collaborated with our lab and contributed to my graduate school experience and research. First, in Dr. Wicha's lab, I would like thank Hasan Korkaya, April Davis, Gabriella Dontu, Suling Liu, Shawn Clouthier, Sean McDermott, Luo Wang, Khaled Hassan, Yad Deol, Michael Brooks, Ali Quraishi, Tahra Luther and Diane Argyle for their support over the years, going back to my first research opportunities. I would thank our collaborators at IMRA America, including Masayuki Ito, Wei Qian, Yong Che, Yuki Ichikawa, Bing Liu, Kevin Hagadorn and Andrius Marcinkevicius. I am also grateful to Shaomeng Wang, Xu Ran, Hacer Karatas, Qiao Li, Greg Thurber, Liang Zhang, Mitchell Smith, and Anne McNeil for their collaborations. Additionally, I would like to thank the Unit for Laboratory Animal Medicine veterinarians, particularly Felicia Duke, technicians, and husbandry staff for assisting me and teaching me how to provide the best possible care for my mice.

Numerous friends and colleagues have impacted my graduate experience for the better. In particular I would like to thank Emily Rabinsky, Adam Cole, Maria Posada, Yehua Xie, Brittany Bailey, Brian Krieg, Seyi Adeniyi, Ronak Shah, Yajun Liu, Maya Lipert, Kefung Sun, Jason Baik, Neal Huang, Cara Hartz Nelson, Karthik Pisupati, Allison Matyas, Amy Doty, Rae Sung Chang, Xiaomei Chen, Kellisa Hansen, Kari Blain, Rui Kuai, Lukasz Ochyl, Nicholas Waltz, Joe Bazzill, Patrick Sinko, Misha Mikhail, Anthony Emanuele, Melissa Holt,Vesna Milacic, Rahul Keswani, Karl Olsen, Meong Cheol Shin, and Gi Sang Yoon, Mitchell Smith, Kylee Smith, Uli Betz, Klaus-Dieter Franz, and the other participants in the 2014 Merck-Serono Innovation Cup.

I would like to recognize those who influenced my decision to go to graduate school and played a role in my efforts to get there. In addition to those mentioned above from Dr. Wicha's

lab, I would like to thank James Wilkes and Barry Barkel in the Chemical Engineering Department, Elijah Petersen and Roger Pinto from Dr. Walter Weber's lab, and Rick St. John, Michael Lee and many others in the Late Stage Purification Department at Genentech. I must also mention Flojaune Griffin and Elijah Petersen for exposing me to graduate student life and for being an inspiration, and Chris Muhich and Ashley Velez for their friendship and support in getting through the chemical engineering undergraduate program at Michigan.

While I cannot possibly include all of the friends and family who have supported me throughout my life, I would like to mention Sara Feeney, Amber Myers, John Unger, and the Morris, Smith, Bow, and Paholak families. To my in-laws, Karen, Dave, and Helen – each day I am grateful for having you in my life. None of this would be possible without the support of my loving parents, Tammy and Kevin, who would give anything in the world for me. Thank you for your sacrifices, the examples you set, and for encouraging me to follow my dreams. Finally, to my husband Tom – you, and the family we have created, have brought me indescribable joy. Growing up with you has made me who I am today. I am eternally grateful for your love, faith, and undying support – past, present, and future.

TABLE OF CONTENTS

LIST OF TABLES

LIST OF FIGURES

ABSTRACT

Rapid advances in bioinformatics and nanotechnology have sparked pre-clinical development of innovative therapies with potential to transform approaches to non-specific clinical practices such as chemotherapy and radiation. One of few nanoparticle-based treatments in clinical trials is photothermal therapy (PTT), which is localized by near infrared light activation of heat-producing gold nanoshells. Here we demonstrate nanoparticle-mediated PTT as a multifunctional platform to address key challenges of cancer medicine, to improve patient tolerance and long-term survival. We present our work in two sections: enhancing efficacy in metastatic settings, and increasing specificity to reduce associated toxicity.

In the first section, we focus on the efficacy of PTT against breast cancer stem cells (BCSCs) and tumor-mediated immunosuppressive signaling – vital drivers of cancer growth and metastasis. First we study PTT via highly crystallized iron oxide nanoparticles (HCIONPs) in human breast cancer cells in immune-compromised mice. PTT inhibits both epithelial-like (ALDH+) and mesenchymal-like (CD44+/CD24-) BCSCs and BCSC-driven secondary tumor formation. PTT prior to surgery prevents lymph node metastasis. Next we evaluate HCIONP-mediated PTT and cancer immunotherapy (PD-L1 antibody) in immune-competent mice. PTT significantly reduces mouse ALDH+ BCSCs when given alone and in combination with PD-L1 antibody. Combination treatment reveals promising reductions in tumor growth and formation of lung macrometastases. Furthermore, increases of key inflammatory cytokines and immune

cell-attracting chemokines suggest the potential to enhance T-cell tumor infiltration to trigger a systemic, cancer (stem) cell-specific immune response.

In the second section, we focus on development of optimized targeted nanoparticle formulations, applicable for PTT, to improve specificity and efficiency of cancer therapy. First we report a new technique – 'living' PEGylation – to control the density and composition of heterobifunctional poly(ethylene glycol) (HS-PEG-R) on gold nanoparticles. Applications we demonstrate include control of targeting ligand (HS-PEG-RGD) density to maximize nanoparticle targeting efficiency, and development of double-charged, stealthy nanoparticles (optimal HS-PEG-NH_2 to HS-PEG-COOH ratio) to minimize immune cell uptake. Lastly, we describe targeted, theranostic nanocomposites with a core-satellite structure for PTT and magnetic resonance imaging. A facilely produced "clickable" targeting peptide enables precise control over attachment to the nanoparticles to prevent steric hindrance and optimize binding to the target receptor.

CHAPTER 1. INTRODUCTION

1.1 The challenges posed by the complexity of cancer, and strategies to overcome them with novel approaches and optimal formulations of nanoparticles for photothermal therapy

While cancer is primarily described as uncontrolled cell growth, it is an extremely heterogeneous disease with many types and subtypes [1]. It can occur in the blood (e.g., lymphoma, leukemia) or as a solid tumor, defined as a carcinoma when originating from epithelial tissues and as a sarcoma when originating from connective tissues [2]. Solid cancers can occur in non-vital organs, such as the breast or skin, or vital organs such as brain, lung, and liver. According to the "two hit" theory, whether arising from heritable genetic mutations, environmental exposures, or a virus, cancer progresses when both copies of a gene become mutated [3]. Such genes are known as oncogenes (often dubbed "gas pedals") when driving proliferative and survival pathways, or as tumor suppressor genes (dubbed "brakes") when driving inhibitory pathways such as cell cycle arrest and apoptosis [4].

On the path to achieving a unified definition of cancer, Weinberg and Hanahan famously published the "Hallmarks of Cancer;" it was followed by an additional publication in 2011 to include emerging hallmarks and enabling characteristics [1, 5]. Their six original hallmarks of acquired capabilities included 1) sustaining proliferative signaling, 2) evading growth suppressors, 3) resisting cell death (evading apoptosis), 4) enabling replicative immortality, 5) inducing angiogenesis, and 6) activating invasion and metastasis. To this they added

deregulating cellular energetics and avoiding immune destruction as emerging hallmarks. Finally, the authors attributed two enabling characteristics that allow cancer cells to acquire such capabilities: genome instability and mutation, and tumor-promoting inflammation driven by immune cells that normally function to fight infections and heal wounds. With these in mind we discuss here some of the features of cancer that pose key challenges for developing effective therapies, and propose strategies that form the basis of this dissertation.

First, along the lines of Weinberg's and Hanahan's first hallmark of sustaining proliferative signaling, cancer cells are highly adaptable for survival. Functional redundancy, crosstalk, and feedback loops in pathways driving cancer cell growth and survival often allow them to rely on alternate signaling in response to cancer therapy, leading to acquired resistance [6-8]. Second, cells comprising solid tumors can be heterogeneous in type(e.g., cancer-associated fibroblasts) or differ more subtly in terms of genetic of epigenetic changes that alter phenotype and can lead to varying functional roles to sustain tumors [9, 10]. Consequently, these cellular differences may necessitate more than one therapeutic target for effective elimination [11]. For instance, cancer-associated fibroblasts (CAFs) in the tumor stroma are similar to normal fibroblasts that offer structural support in most epithelial tissues, but have become activated by cancer cells to release soluble factors that facilitate cancer growth and angiogenesis [5, 12]. Of (arguably) more significance are cancer stem cells (CSCs), a small population of cancer cells with defining stem cell features including the ability to self-renew and differentiate. These long-lived cells have an increased likelihood of acquiring mutations, and growing evidence suggests they are responsible for tumor initiation and are key drivers of tumor growth and metastasis [13, 14].

Efficacy of treatment is severely impaired when cancer cells are no longer localized but have disseminated from the primary tumor site and established metastatic growths [15]. Many localized cancers caught early enough are not fatal. However, more advanced cancers can metastasize to vital organs and interfere with their function and the body's ability to make white blood cells and fight infections [16, 17]. In order for tumors to grow and metastasize, however, they must be able to escape recognition by immune cells [18, 19]. The ability of cancer to upset the immune system's delicate balance of self-tolerance and maintaining tissue homeostasis by monitoring for signs of distress is a crucial factor for tumor-initiating cells to develop into macroscopic growths and establish growths at metastatic sites [20].

Here we propose a nanomedicine platform to develop a cancer therapy that encompasses multiple strategies to overcome these challenges that stem from the inherent properties of cancer cells. In the first section of this dissertation we focus on the efficacy of employing nanoparticle-mediated hyperthermia, photothermal therapy (PTT) specifically, in the fight against cancer stem cells and tumor-mediated immunosuppressive signaling – vital drivers of cancer growth and metastasis. Combination therapy incorporating nanoparticle-mediated PTT, as we present here, or modification of the nanoparticles themselves for multimodal therapy (e.g., PTT and drug delivery) may be utilized to enhance treatment efficacy and mitigate acquired resistance. In addition to serving as a multifunctional platform to address key challenges cancer cells pose, another major advantage of nanoparticle-mediated PTT is its potential to improve the specificity and efficiency of cancer cell destruction by being localized and targeted. Given the lack of specificity and off-target toxicity of mainstream cancer therapy (e.g., chemotherapy), we thus dedicated the second section of this dissertation to the development of optimized formulations of targeted nanoparticles for photothermal cancer therapy.

1.2 Targeting signaling pathways of CSCs driving tumor growth and metastasis

Cancer cells with stem cell characteristics were first discovered in acute myeloid leukemia by John Dick's group [21], and soon evidence for the cancer stem cell (CSC) model began to arise in many solid cancers [22-26]. According to the model, tumors are initiated by stem (or progenitor) cells normally responsible for tissue maintenance and repair but, by their long-lived nature, have a greater susceptibility to acquiring mutations [13]. Dysregulation of stem cell self-renewal results in transformed CSCs with the ability to drive tumor formation enabled by their pluripotent differentiation capacity [13, 14]. In line with their enhanced propensity to initiate tumors in immune-compromised mice [22, 27], CSC literature suggests that only disseminated CSCs have the capabilities to become activated and drive growth of macrometastases at distal sites [13, 28, 29]. Weinberg's group reported an association between CSCs and epithelial-to-mesenchymal transition (EMT) [30], which results in phenotypic changes that could facilitate dissemination and metastasis such as loss of cell-to-cell contact and loss of polarity [31]. While CSCs have been credited as the drivers of metastasis in multiple cancers [31-36], CSCs of the breast remain among the most extensively studied largely in part to the work of Wicha and colleagues to elucidate the roles of breast CSCs (BCSCs) in tumor growth, dissemination, and metastasis formation.

CSCs were first reported in solid tumors in 2003 when Al-Hajj et al. identified them in breast cancer by the surface receptor phenotype CD44+/CD24- [22], and in 2007 Ginestier et al. also identified breast cancer cells with high levels of aldehyde dehydrogenase (ALDH+) [27] as meeting the functional CSC requirements according to mammosphere and secondary implantation assays [37]. Recently the Wicha group conducted genetic profiling revealing that the two BCSC populations are distinct and yet plastically transition from one form to the other as

signaled by the tumor microenvironment [31]. The authors report that the ALDH+ BCSCs exist in a mesenchymal-to-epithelial (MET) state and are primarily proliferative and concentrated at the tumor's interior. In contrast, the CD44+/CD24- BCSCs exist in an epithelial-to-mesenchymal (EMT) state and are primarily quiescent and concentrated at the tumor's invasive edge. Their findings suggest that ALDH+ epithelial-like BCSCs may play a more dominant role in tumor growth, while metastasis may be more driven by CD44+/CD24- mesenchymal-like BCSCs that are less dependent on cell-to-cell contact for survival.

Given the crucial role of cancer stem cells in tumor and metastasis development and the increasing evidence of their resistance to traditional therapies that can lead to recurrence [38-43], innovative therapies that are effective against CSCs will be crucial to enhance long-term patient survival. Several pathways have been reported to regulate CSCs in multiple cancer types and have been the subjects of targeted therapies, some advancing to human clinical trials. The first three heavily studied pathways were Wnt, Hedgehog, and Notch, which regulate self-renewal in normal stem cells [13, 14, 44, 45]. Reya et al. were among the first to demonstrate the critical role of the Wnt pathway in haematopoietic stem cell (HSC) regulation [46]; it has since been implicated in regulating CSCs in a variety of cancers including colon [47]. Key players in the Wnt signaling pathway include the Frizzled and lipoprotein receptor-related protein (LRP) receptor families on the cell surface and the downstream target β-catenin, which translocates to the nucleus to activate gene transcription [48, 49]. B-catenin is also influenced by crosstalk signaling from Akt (protein kinase B) and phosphoinositide 3-kinase (PI3-K) pathways to regulate CSCs [50]. Two clinically approved nonsteroidal anti-inflammatory drugs (NSAIDs) have begun clinical trials for Wnt targeting: Celecoxib for inhibition of β-catenin and Sulindac to block Dishevelled (DSH, DVL), which normally functions to prevent β-catenin from being

degraded following ubiquitination. Among other agents being investigated in clinical trials are ones targeting β-catenin, and monoclonal antibodies targeting either Wnt ligands or the Frizzled and LRP receptors [45]. Sonic hedgehog (SHH) is the best studied of the three mammalian Hedgehog pathways [51-53].Hedgehog ligand binding to the Patched (PTCH) receptor allows Smoothened (SMO) to associate with the cell membrane, leading to GLI-mediated activation of transcription of genes such as *GLI1* and *PATCH1* [48, 49]. Vismodegib (Genentech), an inhibitor of SMO, was approved in 2012 by the Food and Drug Administration (FDA) for basal-cell carcinoma (BCC) [45]. Like Vismodegib, most other agents in clinical trials are cyclopamine-competitive antagonists of SMO, including Sonidegib and Saridegib.

Following the discovery of breast CSCs as the first solid tumor CSCs, Dontu et al. demonstrated the involvement of Notch signaling in mammary stem/progenitor cell self-renewal and differentiation and proposed that dysregulation of the pathway could give rise to breast CSCs [54]. Additional studies since have demonstrated a crucial role for Notch signaling in other types of CSCs [55-57]. The Notch receptor family is composed of four mammalian homologs (Notch 1-4). Signaling can be activated by binding of Delta-like (DLL-1, DLL-3, DLL-4) or Jagged (Jagged-1, Jagged-2) ligands on a neighboring cell. This induces a series of receptor cleavage events involving A Disintegrin and Metalloproteinase (ADAM) and γ-secretase enzymes, resulting in release of the Notch Intracellular Domain (NICD) which traffics to the nucleus and relieves repression of transcription factors for genes such as those in the *HES* family [54, 58, 59]. Clinical trials of Notch-targeting agents include several γ-secretase inhibitors (GSIs) produced by various companies as well as monoclonal antibodies to block ligand binding, including anti-Notch 1, 2, and 3 antibodies and multiple anti-DLL-4 antibodies [45].

Aside from the three classic CSC-regulating pathways, Wnt, Hedgehog, and Notch, therapeutics for additional targets have been explored and discussed in detail in the literature. These include but are not limited to Perifosine to inhibit AKT, inhibitors of IL-6 and IL-8 cytokine signaling such as Repertaxin for CXCR1, and blocking of Her2 signaling (that occurs through PTEN and PI3-K) for which Trustuzumab is the pioneer Her2 inhibitor [49, 50]. Monoclonal antibodies have also been developed against various stem cell surface markers expressed on CSCs, such as CD44 and CD133 [60-62]. While few nanoparticle-based therapies, and none targeting CSCs, have advanced to clinical trials, recent advances in nanoparticle development offer great potential to combine strategies to enhance cancer treatment efficacy against CSCs.

1.3 Cancer evasion of immune surveillance and approaches for cancer immunotherapy

In 1909 Paul Ehrlich first proposed a connection between immune system function and cancer development, suggesting the importance of immune suppression of cancer growth [63-66]. Decades later experimental models began to confirm the ability of the immune system to suppress tumors, and in 1957 Burnet published the theory of immune surveillance of tumor-associated antigens [64-68]. Later development of immunodeficient mouse models eventually led to definitive data supporting the theory. In 2001 Shankaran et al. showed that mice lacking T-cells, B-cells, and natural killer T (NKT) cells experienced a greater incidence of 3-methylcholanthrene (MCA)-induced sarcomas and spontaneous epithelial carcinomas compared to control mice [64, 66, 69]. A year later Dunn et al. published a review in which they outlined cancer immunosurveillance as part of a larger process termed immunoediting, broken down into

three components: elimination, equilibrium, and escape [18, 70]. As they describe it, "elimination represents the classical concept of cancer immunosurveillance, equilibrium is the period of immune-mediated latency after incomplete tumor destruction in the elimination phase, and escape refers to the final outgrowth of tumors that have outstripped immunological restraints of the equilibrium phase" [64].

The main idea behind cancer immunotherapy is to restore the balance of power in favor of the immune system and induce cancer cell destruction in a process like the elimination phase of immunoediting. In the elimination (immunosurveillance) phase, the innate immune system, which includes natural killer (NK) cells and antigen-presenting cells (APCs) such as dendritic cells (DCs) and macrophages, detects the growing tumor; through antigen presentation it alerts cells of the adaptive immune system such as CD8+ and CD4+ T-cells. These cells then home to the tumor site to attack the tumor cells expressing the recognized antigens. However, the exact process by which the innate and adaptive immune system becomes alerted remains the subject of further study [18, 19]. The first mechanisms proposed came from Dunn et al., who suggested that chemokines released by tumor cells combined with proinflammatory molecules, present from structural remodeling in the stroma to support tumor growth, act as a danger signal that alerts cells of the innate immune system. Upon detection of the tumor cells, an interferon-γ (IFN-γ)-dependent and NK cell-dependent mechanism triggers initial killing of tumor cells by the innate immune system. As a result, APCs are exposed to tumor antigens and migrate to the tumor draining lymph nodes [18]. There, cross-presentation of antigenic tumor peptides displayed on MHC class I molecules on APCs activates CD8+ cytotoxic T-cells of the adaptive immune system [18, 71]. At the tumor the activated CD8+ T-cells bind MHC molecules on cancer cells via their T-cell receptors (TCRs). The T-cells mediate cancer cell death by

exocytosis of perforin, which forms pores in the cell membrane and allows granzymes, also released by the T-cells, to induce apoptosis by caspase-dependent and caspase-independent mechanisms [72, 73]. CD4+ T-helper cells release IL-2 to promote CD8+ T-cell function and viability. Furthermore, the dying tumor cells release IFN-γ which triggers additional mechanisms of cell death, such as apoptosis [18]. If total cancer cell destruction occurs in the elimination phase, then the immunoediting process is complete. However, tumor cell variants arising from genetic or epigenetic changes that are missed during the elimination phase and develop immune resistance in the equilibrium phase enter the escape phase and may expand to become clinically detectable tumors [18].

In 2013, Science Magazine named cancer immunotherapy as the Breakthrough of the Year; however, clinical investigations of this therapeutic approach had begun decades earlier. In 1992 IL-2, which promotes activation and proliferation of T-cells and NK cells, became one of the first FDA-approved immunotherapies, indicated for metastatic melanoma and renal cell carcinoma [74]. Some immunotherapy efforts have focused on therapeutic vaccines, in contrast to prophylactic vaccines such as the human papillomavirus (HPV) vaccine approved in 2006, to trigger T-cell responses. However, this approach using peptides or proteins to generate effector T-cells did not prove to be very fruitful, and scientists considered other approaches such as cell-based vaccines. In 2010 the FDA approved the cell-based vaccine Provenge for advanced prostate cancer [75]. In this individualized therapy, APCs from the patient's blood are co-cultured with the prostate cancer antigen prostatic acid phosphatase (PAP) before being returned to the patient.

More recent T-cell-focused cancer immunotherapies include adoptive cell transfer (ACT), genetic engineering of T-cells, and immune checkpoint inhibition. In adoptive cell

transfer, a patient's T-cells are first removed to culture and expand *ex vivo* and then reintroduced into the patient to expand the pool of viable tumor-infiltrating lymphocytes (TILs). IL-2 may be included in either the culture or reintroduction steps following lymphodepletion in the patient by chemotherapy to facilitate engraftment [75-77]. Complete durable responses were observed when ACT was tested in melanoma patients for whom other therapies did not work [75, 78]. Building off his pioneering successes with ACT, Rosenberg began to work with Eshhar to engineer the T-cells harvested from patients. Known as CAR T-cells, they are genetically engineered to produce chimeric antigen receptors (CARs) on their surface to recognize tumor cells through the CAR's affinity domain (usually a single chain variable fragment (scFv) antibody). CAR technologies have been commercialized and shown marked results in Phase I clinical trials of patients with refractive acute lymphoblastic leukemia (ALL); second generation molecules are already in development [75, 79-81].

Development of therapeutic antibodies for immune checkpoint inhibition focuses on the breakdown of the Cancer-Immunity Cycle at different steps. This cycle was defined in 2013 by Chen and Mellman, dividing it into seven steps essentially mirroring Dunn's 2002 description of the elimination phase of immunoediting [82, 83]. As a mechanism to maintain balance of immune function, T-cells have coregulatory inhibitory signals that occur during the TCR-MHC-mediated priming by APCs (step 3 of the cycle) and TCR-MHC-mediated recognition of tumor cells (step 6). Inhibitory signaling through the cytotoxic T-lymphocyte-associated protein 4 (CTLA-4) receptor on CD8+ T-cells during priming by APCs may function to dampen T-cell activation. Anti-CTLA-4 antibodies block this first T-cell checkpoint. Inhibitory signaling through the programmed death 1 (PD-1) receptor on activated CD8+ T-cells during binding to target cells in response to inflammation or infection may act to regulate T-cell activity in

peripheral tissues. PD-1 expression has been found to be higher on tumor-infiltrating T-cells than those that infiltrate normal tissues. Furthermore, studies have shown that various types of cancer cells, including melanoma, have elevated expression of the programmed death ligand 1 (PD-L1) receptor that activates this second inhibitory T-cell checkpoint through PD-1; this has been correlated with poor clinical outcome [84, 85].

Antibodies targeting both PD-L1 and PD-1 have advanced to clinical trials in patients with melanoma, renal cell carcinoma (RCC), and non-small cell lung cancer (NSCLC), and are sometimes used in combination with an anti-CTLA-4 antibody [82, 83, 85]. In a phase Ib clinical trial, Nivolumab (anti-PD-1) and Ipilimumab (anti-CTLA-4) were given to advanced melanoma patients either concurrently or sequentially. Patient survival rates were an astonishing 94% and 88% after one and two years, respectively, considering that the median survival of patients with metastatic melanoma is less than one year [86-88]. Various clinical trials have been conducted for anti-CTLA-4 antibodies as well. After conclusive data of improved median survival in metastatic melanoma patients receiving Ipilimumab in phase III clinical trials, the treatment received FDA approval as either initial therapy or treatment after relapse in patients with metastatic melanoma [75, 87, 88]. However, given the decrease in specificity of T-cell inhibition by inhibiting the checkpoint during the priming phase rather than the effector phase at the tumor site, immune-related adverse reactions were observed in patients treated with Ipilimumab anti-CTLA-4 therapy [75, 87, 88]. Other immune checkpoint inhibitors have recently gained FDA approval as well, including Nivolumab for melanoma in 2014 and NSCLC in 2015 [89]. While not yet at the point of clinical investigation, the potential to improve long-term survival in cancer patients receiving immunotherapy may be enhanced by combination with

treatments that kill cancer stem cells and result in a T-cell response that specifically recognizes cancer cells and also CSCs [90-94].

1.4 Cancer nanomedicine design strategies, and advantages and approaches to nanoparticle-mediated photothermal cancer therapy

While still in its infancy, research in the field of nanomedicine is booming with potential to develop innovative solutions to solve current limitations of cancer therapies. The diversity of nanoparticle design significantly enhances the ability to develop specialized therapies not possible with conventional chemotherapy alone. Biodegradable or biocompatible nanoparticles, including those composed of polymers, carbon, iron oxide, and gold [95-98], can function themselves as therapeutics or imaging agents, serve as vessels for therapeutic drugs, and be modified to facilitate control over interactions in biological systems. Iron oxide nanoparticles are capable of magnetic resonance imaging and gold-based nanoparticles of photoacoustic, Raman, and other imaging techniques; furthermore, both types of nanoparticles can be exploited to induce localized hyperthermia [96, 99-101]. Polymer-based nanoparticles such as liposomes and micelles can be encapsulated with therapeutics to improve their formulation; such designs may overcome poor solubility or protect and sustain delivery of biologic therapeutics, such as proteins and siRNA [102-105]. Similarly, drugs can be appended to and released from the surface of nanoparticles. Through size-based passive targeting such as the enhanced permeability and retention (EPR) effect, drug delivery via nanoparticles can enhance control over drug distribution (tumor uptake), improve pharmacokinetic (PK) properties such as half-life, and reduce off-target toxicity.

Nanoparticles may also be modified to impart features such as stealth or active targeting capabilities. Stealth to minimize recognition by immune cells may be granted by coating the surface of nanoparticles with the hydrophilic polymer poly(ethylene glycol) (PEG) or zwitterionic molecules to create a neutral surface charge [106-108]. PEG is also frequently used to improve nanoparticle stability and solubility. Ligands may be added to enhance uptake by cancer cells with certain phenotypes (e.g., Her2+ breast cancer) or specific populations of cancer cells (CD44+ breast cancer stem cells), or to target drugs to subcellular locations (e.g., cell nuclei) [62, 109, 110]. Finally, nanoparticles have been used in different capacities to stimulate an immune response, for instance by directly delivering antigen as with traditional vaccine development or more indirectly by triggering a T-cell attack in response to nanoparticle-mediated death of tumor cells as previously discussed [111-115]. A summary of the various pre-clinical strategies for which nanoparticles may be used to address limitations of conventional cancer therapy and representative literature is included in Table 1.1 below.

Table 1.1. Nanoparticle-based pre-clinical strategies to improve conventional cancer therapy

Cancer Nanomedicine Pre-Clinical Research Strategies	**References**
Improving formulation of therapeutics	[102-105]
Externally triggering drug release	[116, 117]
Increasing drug uptake at the tumor site	[118, 119]
Controlling intracellular drug localization	[110, 120]
Reducing off-target toxicity	[121, 122]
Offering multimodal treatment	[123, 124]
Non-invasive imaging to track particle or drug localization	[125, 126]
Stimulating immune response	[111-115]

Few nanoparticle formulations have been approved for market use in cancer patients. Two more commonly known are Abraxane, albumin-bound Paclitaxel, and Doxil, Doxorubicin encapsulated into polymer-coated liposomes. These passively targeted nanoparticle formulations have an improved therapeutic index, enhancing the efficacy-to-toxicity profile, compared to their drug-only counterparts [127]. A few iron oxide-based nanoparticles have been approved for diagnostic cancer imaging, such as Feridex [127]. Other nanoparticle-based therapies have advanced to clinical trials, but these have currently been limited to relatively simple formulations. Examples include Aurimune, precisely sized, PEG-coated gold nanoparticles (AuNPs) for passive targeting of tumor necrosis factor (TNF) [128], and AuroLase, PEG-coated gold nanoshells that kill cancer cells through light-activated thermal ablation (i.e., photothermal therapy). Biodegradable or biocompatible nanoparticle formulations with simple designs can be most easily translated from pre-clinical research to clinical trials in humans because they are easier to characterize, and the production process is more reproducible and scalable for mass manufacturing. A more complex formulation may be denied FDA approval if the safety and efficacy of each component (e.g., polymer coating, targeting ligand) cannot be verified from clinical trials.

For our studies, our goal was to develop nanoparticles to improve current cancer therapy approaches by enhancing efficacy in metastatic settings and increasing specificity to reduce associated toxicity. Our work described here focuses on nanoparticle-mediated photothermal therapy (PTT), as it presents a multifunctional platform for localized, targeted therapies with potential to inhibit metastasis through multiple approaches. PTT is also one of few examples of nanoparticle-mediated treatments to enter clinical trials in human cancer patients [127, 129]. PTT produces hyperthermic cell destruction dependent upon application of near infrared (NIR)

laser light to tumor tissue containing nanoparticles which convert the light into heat. While PTT offers multiple advantages of nanomedicine-based cancer treatments, possibly most significant is external control of localized hyperthermia to reduce off-target toxicity compared to other intravenously injected therapies such as conventional chemotherapy. Other localized cancer therapies studied in pre-clinical research can be more difficult to precisely control, being dependent upon a tumor-specific trigger. Examples include drug-loaded nanoparticles for which release is pH-dependent and activated by the slightly acidic tumor environment, or mediated by specific enzymes such as extracellular matrix (ECM)-degrading matrix metalloproteinases (e.g., MMP-2) with high extracellular expression in tumor tissue [126, 130-134].

PTT-mediating nanoparticles can be formulated for active targeting in addition to passive targeting to improve the therapeutic window (efficacy-to-toxicity profile). Passive targeting relies on physical properties of the nanoparticles, such as size or surface charge, that enhance physiological characteristics such as half-life in the bloodstream (i.e., rate of elimination), plasma protein binding, recognition by immune cells, and the ability to exploit the enhanced permeability and retention (EPR) effect resulting from the relatively leaky vasculature and poor drainage of the tumor environment. Actively targeted therapeutics incorporate receptor-homing ligands designed to increase cellular uptake once nanoparticles have accumulated at the tumor site through passive targeting. Various approaches have been taken to develop actively targeted cancer therapeutics and become clinically available, including monoclonal antibodies (e.g., Herceptin for Her2+ breast cancer) and antibody-drug conjugates (e.g., Herceptin-containing Kadcyla). Actively targeted nanoparticles are formulated using monoclonal antibodies and peptides. The gold nanoshells used for clinical trials of AuroLase PTT solely rely on passive targeting; development of actively targeted nanoparticles may reduce the intravenous dose

required to achieve a similar intratumoral nanoparticle concentration, potentially benefiting the patient and lowering the cost of treatment.

Another advantage of nanoparticle-mediated PTT is that cancer cell death by hyperthermia may be less likely to result in development of treatment resistance, compared to nanoparticles delivering biologics and small molecule drugs that rely on inhibition of a particular molecular pathway; the latter can be faced with development of resistant cancer cells that have learned to rely on alternative survival pathways [43, 135]. As PTT isn't pathway specific it is applicable to a wider variety of patients, including difficult-to-treat subtypes such as triple negative breast cancer which lacks estrogen, progesterone, and Her2 receptors exploited for targeted therapy. Perhaps most exciting is the potential employ nanoparticle-mediated PTT in combination therapy that can be applied to metastatic cancer settings. Initial research has shown nanoparticle-mediated PTT has applications in enhancing therapies to target cancer stem cells [40, 136] suggested to be responsible for driving tumor growth and metastasis. Development of imagable, targeted nanoparticles may allow for localized PTT at sites of macrometastases. Inhibition of both micro- and macrometastases may also be possible in light of recent findings that nanoparticle-mediated hyperthermia induces a systemic cancer-specific immune response in which cytotoxic T-cells are trained to recognize and inhibit distal cancer cells [113], a response that may be strengthened by coupling with immunotherapy [137, 138].

Gold-based nanoparticles are the gold standard for nanoparticle mediators of photothermal cancer therapy [99, 100, 129, 139-144], following the pioneering research of Mostafa El-Sayed's group with gold nanorods (AuNRs) and Jennifer West's group that developed the silica-core gold nanoshells (AuNSs) commercialized into AuroLase therapy [99, 100, 110, 140, 144]. These particular gold structures have a peak absorbance of near infrared

(NIR) light, which allows for maximal tissue penetration and selective heating of nanoparticles due to the low light absorbance by tissue chromophores at this wavelength [145]. Gold efficiently converts light irradiation into heat by causing oscillations of electrons at the nanoparticle surface, a phenomenon known as surface plasmon resonance [146]. In addition to being biocompatible, an advantage of gold nanoparticles (AuNPs) is gold's affinity to form covalent Au-S bonds for facile surface modification (with polymer coatings, targeting ligands, therapeutic agents, etc) using thiol functional groups [106]. Various types of imaging are possible with AuNPs, including photoacoustic, Raman, and computed tomography (CT), although clinical nanoparticle-based cancer imaging has been predominantly magnetic resonance imaging (MRI) via magnetic nanoparticles [147-149].

Following gold nanoparticles, carbon nanotubes have become more commonly selected for pre-clinical PTT research [61, 136, 138, 150-155]. Among their chief attributes for PTT is the ability of NIR light to induce single-walled and multi-walled carbon nanotubes composed of graphene to enter an excited state, resulting in release of vibrational energy that produces heat [156]. Like gold-based nanoparticles they can be produced in ideal size ranges for circulation in the blood stream and for passive tumor targeting via the EPR effect, and can be modified for loading of therapeutics or active targeting agents. Formulation strategies to maximize carbon nanotube (CNT) biocompatibility and minimize off-target toxicity remain the subject of further investigation. Other types of nanomaterials have been investigated to a lesser extent for photothermal therapy, including copper sulfide nanoparticles and nanographene sheets [111, 157].

Iron-oxide containing nanoparticles have traditionally been used for cancer hyperthermia controlled by an alternating magnetic field (AMF) [101, 113, 129, 158]. However, all

intravenously injected nanoparticles will undergo significant uptake in off-target organs, particularly the liver, due to the reticuloendothelial system (RES) or mononuclear phagocyte system (MPS) [159-161]. Many iron oxide nanoparticle (IONP) formulations for cancer hyperthermia are intratumorally injected [101, 113] to avoid off-target heating in other organs; consequently, this form of hyperthermia is less translatable for human clinical trials than PTT. Our group recently reported that production of highly crystallized iron oxide nanoparticles (HCIONPs) in organic solvent via thermal decomposition results in significant and selective heating capabilities not attainable with all IONP formulations [96]. Synchotron x-ray diffraction (XRD) revealed significantly stronger peaks in the 400 and 440 planes for our HCIONPs compared to commercial IONPs produced in aqueous solution, indicating a preferred lattice orientation despite both IONP formulations having the Fe_3O_4 chemical composition. Iron levels of HCIONPs in different tissues of mice returned to background levels within three months of intravenous injection, suggesting their ability to biodegrade. Their ability to image tumors via MRI, a method currently used clinically, gives the HCIONPs another distinct advantage. Furthermore, the relatively small size (< 20 nm) of our stealthy, polymer-coated HCIONPs facilitates efficient tumor accumulation after intravenous injection. Consequently, we employ these HCIONPs for our work in subsequent chapters to investigate novel applications of nanoparticle-mediated PTT in metastatic breast cancer: inhibiting cancer stem cells and eliciting a T-cell-mediated immune response. These HCIONPs also function as a component of the nanoparticle formulation we develop for targeted photothermal therapy.

1.5 Specific Aims

The overall goal of this work was to develop a nanoparticle approach to address two key challenges of cancer medicine: enhancing efficacy in metastatic settings and increasing specificity to reduce associated toxicity. As such, we developed two objectives utilizing nanoparticle-mediated photothermal therapy as a multifunctional platform: 1) to inhibit cancer stem cells and tumor-mediated immunosuppressive signaling as vital drivers of tumor growth and metastasis, and 2) to enhance targeting specificity of therapy. The work described here is divided into two parts and an appendix.

- Part I: Novel approaches to nanoparticle-mediated photothermal therapy in metastatic breast cancer
    - Aim 1: To inhibit epithelial-like and mesenchymal-like breast cancer stem cells via nanoparticle-mediated photothermal therapy to prevent metastasis of human breast cancer in immune-compromised mice
    - Aim 2: To inhibit breast cancer stem cells and metastasis in immune-competent mice via nanoparticle-mediated photothermal therapy, and investigate photothermal therapy conditions that will trigger a tumor-specific T-cell attack to enhance immune checkpoint blockade efficacy against metastatic breast cancer
- Part II: Engineering nanoparticles for targeted photothermal cancer therapy
    - Aim 3: To optimize cancer cell uptake of gold nanoparticles by 'Living' PEGylation to control targeting ligand and charge densities
    - Aim 4: To develop an optimal, stable formulation for peptide-targeted theranostic nanoparticles for localized PTT

- Appendix A: Evaluation of Jagged1 peptides to target breast cancer stem cells through Notch receptor expression

1.6 References

1. Hanahan, D. and R.A. Weinberg, *The hallmarks of cancer.* Cell, 2000. **100**(1): p. 57-70.
2. *Types of Cancer.* Cancer Research UK, 2014.
3. Russo, E., *'Two-Hit' Hypothesis.* The Scientist, 1999.
4. Ozono, E.Y., Shoji; Ohtani, Kiyoshi *To Grow, Stop or Die? – Novel Tumor-Suppressive Mechanism Regulated by the Transcription Factor E2F.* Future Aspects of Tumor Suppressor Gene, 2013.
5. Hanahan, D. and R.A. Weinberg, *Hallmarks of cancer: the next generation.* Cell, 2011. **144**(5): p. 646-74.
6. Logue, J.S. and D.K. Morrison, *Complexity in the signaling network: insights from the use of targeted inhibitors in cancer therapy.* Genes Dev, 2012. **26**(7): p. 641-50.
7. Yamaguchi, H., et al., *Signaling cross-talk in the resistance to HER family receptor targeted therapy.* Oncogene, 2014. **33**(9): p. 1073-81.
8. Ribeiro, J.R. and R.N. Freiman, *Estrogen signaling crosstalk: Implications for endocrine resistance in ovarian cancer.* J Steroid Biochem Mol Biol, 2014. **143**: p. 160-73.
9. Marusyk, A., V. Almendro, and K. Polyak, *Intra-tumour heterogeneity: a looking glass for cancer?* Nat Rev Cancer, 2012. **12**(5): p. 323-34.
10. Zellmer, V.R. and S. Zhang, *Evolving concepts of tumor heterogeneity.* Cell Biosci, 2014. **4**: p. 69.
11. Korkaya, H. and M.S. Wicha, *Selective targeting of cancer stem cells: a new concept in cancer therapeutics.* BioDrugs, 2007. **21**(5): p. 299-310.
12. Aboussekhra, A., *Role of cancer-associated fibroblasts in breast cancer development and prognosis.* Int J Dev Biol, 2011. **55**(7-9): p. 841-9.
13. Wicha, M.S., S. Liu, and G. Dontu, *Cancer stem cells: an old idea--a paradigm shift.* Cancer Res, 2006. **66**(4): p. 1883-90; discussion 1895-6.
14. Reya, T., et al., *Stem cells, cancer, and cancer stem cells.* Nature, 2001. **414**(6859): p. 105-11.

15. Hunter, K.W., N.P. Crawford, and J. Alsarraj, *Mechanisms of metastasis.* Breast Cancer Res, 2008. **10 Suppl 1**: p. S2.

16. *How can cancer kill you?* Cancer Research UK.

17. Margolese, R., Hortobagyi, GN, Buchholz, TA., *Management of Metastatic Breast Cancer.* Holland-Frei Cancer Medicine, 2003.

18. Dunn, G.P., L.J. Old, and R.D. Schreiber, *The three Es of cancer immunoediting.* Annu Rev Immunol, 2004. **22**: p. 329-60.

19. Schreiber, R.D., L.J. Old, and M.J. Smyth, *Cancer immunoediting: integrating immunity's roles in cancer suppression and promotion.* Science, 2011. **331**(6024): p. 1565-70.

20. de Visser, K.E., A. Eichten, and L.M. Coussens, *Paradoxical roles of the immune system during cancer development.* Nat Rev Cancer, 2006. **6**(1): p. 24-37.

21. Bonnet, D. and J.E. Dick, *Human acute myeloid leukemia is organized as a hierarchy that originates from a primitive hematopoietic cell.* Nat Med, 1997. **3**(7): p. 730-7.

22. Al-Hajj, M., et al., *Prospective identification of tumorigenic breast cancer cells.* Proc Natl Acad Sci U S A, 2003. **100**(7): p. 3983-8.

23. Singh, S.K., et al., *Identification of a cancer stem cell in human brain tumors.* Cancer Res, 2003. **63**(18): p. 5821-8.

24. Prince, M.E., et al., *Identification of a subpopulation of cells with cancer stem cell properties in head and neck squamous cell carcinoma.* Proc Natl Acad Sci U S A, 2007. **104**(3): p. 973-8.

25. Li, C., et al., *Identification of pancreatic cancer stem cells.* Cancer Res, 2007. **67**(3): p. 1030-7.

26. Collins, A.T., et al., *Prospective identification of tumorigenic prostate cancer stem cells.* Cancer Res, 2005. **65**(23): p. 10946-51.

27. Ginestier, C., et al., *ALDH1 is a marker of normal and malignant human mammary stem cells and a predictor of poor clinical outcome.* Cell Stem Cell, 2007. **1**(5): p. 555-67.

28. Liao, W.T., et al., *Metastatic cancer stem cells: from the concept to therapeutics.* Am J Stem Cells, 2014. **3**(2): p. 46-62.

29. Li, F., et al., *Beyond tumorigenesis: cancer stem cells in metastasis.* Cell Res, 2007. **17**(1): p. 3-14.

30. Mani, S.A., et al., *The epithelial-mesenchymal transition generates cells with properties of stem cells.* Cell, 2008. **133**(4): p. 704-15.

31. Liu, S., et al., *Breast cancer stem cells transition between epithelial and mesenchymal states reflective of their normal counterparts.* Stem Cell Reports, 2014. **2**(1): p. 78-91.

32. Michl, M., et al., *Expression of cancer stem cell markers in metastatic colorectal cancer correlates with liver metastasis, but not with metastasis to the central nervous system.* Pathol Res Pract, 2015. **211**(8): p. 601-9.

33. Liu, C., et al., *The microRNA miR-34a inhibits prostate cancer stem cells and metastasis by directly repressing CD44.* Nat Med, 2011. **17**(2): p. 211-5.

34. Varnat, F., et al., *Human colon cancer epithelial cells harbour active HEDGEHOG-GLI signalling that is essential for tumour growth, recurrence, metastasis and stem cell survival and expansion.* EMBO Mol Med, 2009. **1**(6-7): p. 338-51.

35. Mulholland, D.J., et al., *Pten loss and RAS/MAPK activation cooperate to promote EMT and metastasis initiated from prostate cancer stem/progenitor cells.* Cancer Res, 2012. **72**(7): p. 1878-89.

36. Sarkar, F.H., et al., *Pancreatic cancer stem cells and EMT in drug resistance and metastasis.* Minerva Chir, 2009. **64**(5): p. 489-500.

37. Dontu, G., et al., *In vitro propagation and transcriptional profiling of human mammary stem/progenitor cells.* Genes Dev, 2003. **17**(10): p. 1253-70.

38. Bao, S., et al., *Glioma stem cells promote radioresistance by preferential activation of the DNA damage response.* Nature, 2006. **444**(7120): p. 756-60.

39. Creighton, C.J., et al., *Residual breast cancers after conventional therapy display mesenchymal as well as tumor-initiating features.* Proc Natl Acad Sci U S A, 2009. **106**(33): p. 13820-5.

40. Atkinson, R.L., et al., *Thermal enhancement with optically activated gold nanoshells sensitizes breast cancer stem cells to radiation therapy.* Sci Transl Med, 2010. **2**(55): p. 55ra79.

41. Li, X., et al., *Intrinsic resistance of tumorigenic breast cancer cells to chemotherapy.* J Natl Cancer Inst, 2008. **100**(9): p. 672-9.

42. Phillips, T.M., W.H. McBride, and F. Pajonk, *The response of CD24(-/low)/CD44+ breast cancer-initiating cells to radiation.* J Natl Cancer Inst, 2006. **98**(24): p. 1777-85.

43. Korkaya, H., et al., *Activation of an IL6 inflammatory loop mediates trastuzumab resistance in HER2+ breast cancer by expanding the cancer stem cell population.* Mol Cell, 2012. **47**(4): p. 570-84.

44. Takebe, N., et al., *Targeting cancer stem cells by inhibiting Wnt, Notch, and Hedgehog pathways.* Nat Rev Clin Oncol, 2011. **8**(2): p. 97-106.

45. Takebe, N., et al., *Targeting Notch, Hedgehog, and Wnt pathways in cancer stem cells: clinical update.* Nat Rev Clin Oncol, 2015. **12**(8): p. 445-64.

46. Reya, T., et al., *A role for Wnt signalling in self-renewal of haematopoietic stem cells.* Nature, 2003. **423**(6938): p. 409-14.

47. Vermeulen, L., et al., *Wnt activity defines colon cancer stem cells and is regulated by the microenvironment.* Nat Cell Biol, 2010. **12**(5): p. 468-76.

48. Burnett, J., B. Newman, and D. Sun, *Targeting cancer stem cells with natural products.* Curr Drug Targets, 2012. **13**(8): p. 1054-64.

49. McDermott, S.P. and M.S. Wicha, *Targeting breast cancer stem cells.* Mol Oncol, 2010. **4**(5): p. 404-19.

50. Liu, S. and M.S. Wicha, *Targeting breast cancer stem cells.* J Clin Oncol, 2010. **28**(25): p. 4006-12.

51. Tang, S.N., et al., *Inhibition of sonic hedgehog pathway and pluripotency maintaining factors regulate human pancreatic cancer stem cell characteristics.* Int J Cancer, 2012. **131**(1): p. 30-40.

52. Song, Z.Y., Wen; Wei, Bo; Wang, Ning; Li, Tao; Guan, Lidong; Shi, Shuangshuang; Zeng, Quan; Pei, Xuetao; Chen, Lin, *Sonic Hedgehog Pathway Is Essential for Maintenance of Cancer Stem-Like Cells in Human Gastric Cancer.* PLoS One, 2011. **6**(3).

53. Heiden, K.B., et al., *The sonic hedgehog signaling pathway maintains the cancer stem cell self-renewal of anaplastic thyroid cancer by inducing snail expression.* J Clin Endocrinol Metab, 2014. **99**(11): p. E2178-87.

54. Dontu, G., et al., *Role of Notch signaling in cell-fate determination of human mammary stem/progenitor cells.* Breast Cancer Res, 2004. **6**(6): p. R605-15.

55. Bao, B., et al., *Notch-1 induces epithelial-mesenchymal transition consistent with cancer stem cell phenotype in pancreatic cancer cells.* Cancer Lett, 2011. **307**(1): p. 26-36.

56. Hovinga, K.E., et al., *Inhibition of notch signaling in glioblastoma targets cancer stem cells via an endothelial cell intermediate.* Stem Cells, 2010. **28**(6): p. 1019-29.

57. McAuliffe, S.M., et al., *Targeting Notch, a key pathway for ovarian cancer stem cells, sensitizes tumors to platinum therapy.* Proc Natl Acad Sci U S A, 2012. **109**(43): p. E2939-48.

58. Garvalov, B.K. and T. Acker, *Cancer stem cells: a new framework for the design of tumor therapies.* J Mol Med (Berl), 2011. **89**(2): p. 95-107.

59. Fortini, M.E., *Notch signaling: the core pathway and its posttranslational regulation.* Dev Cell, 2009. **16**(5): p. 633-47.

60. Galanzha, E.I., J.W. Kim, and V.P. Zharov, *Nanotechnology-based molecular photoacoustic and photothermal flow cytometry platform for in-vivo detection and killing of circulating cancer stem cells.* J Biophotonics, 2009. **2**(12): p. 725-35.

61. Wang, C.H., et al., *Photothermolysis of glioblastoma stem-like cells targeted by carbon nanotubes conjugated with CD133 monoclonal antibody.* Nanomedicine, 2011. **7**(1): p. 69-79.

62. Wang, L., et al., *CD44 antibody-targeted liposomal nanoparticles for molecular imaging and therapy of hepatocellular carcinoma.* Biomaterials, 2012. **33**(20): p. 5107-14.

63. Ehrlich, P., *Ueber den jetzigen stand der karzinomforschung.* Ned Tijdschr Geneeskd, 1909. **5**: p. 273-290.

64. Dunn, G.P., L.J. Old, and R.D. Schreiber, *The immunobiology of cancer immunosurveillance and immunoediting.* Immunity, 2004. **21**(2): p. 137-48.

65. Kim, R., M. Emi, and K. Tanabe, *Cancer immunoediting from immune surveillance to immune escape.* Immunology, 2007. **121**(1): p. 1-14.

66. Rezaei, N., *Cancer Immunology: A Translational Medicine Context.* 2015.

67. Burnet, M., *Cancer: a biological approach. III. Viruses associated with neoplastic conditions. IV. Practical applications.* Br Med J, 1957. **1**(5023): p. 841-7.

68. Burnet, M., *Cancer; a biological approach. I. The processes of control.* Br Med J, 1957. **1**(5022): p. 779-86.

69. Shankaran, V., et al., *IFNgamma and lymphocytes prevent primary tumour development and shape tumour immunogenicity.* Nature, 2001. **410**(6832): p. 1107-11.

70. Dunn, G.P., et al., *Cancer immunoediting: from immunosurveillance to tumor escape.* Nat Immunol, 2002. **3**(11): p. 991-8.

71. Rabinsky, E.F., *Effect of protein coatings on the delivery performance of liposomes.* 2011.

72. Trapani, J.A. and M.J. Smyth, *Functional significance of the perforin/granzyme cell death pathway.* Nat Rev Immunol, 2002. **2**(10): p. 735-47.

73. Voskoboinik, I., et al., *Perforin: structure, function, and role in human immunopathology.* Immunol Rev, 2010. **235**(1): p. 35-54.

74. Lee, S. and K. Margolin, *Cytokines in cancer immunotherapy.* Cancers (Basel), 2011. **3**(4): p. 3856-93.

75. Mellman, I., G. Coukos, and G. Dranoff, *Cancer immunotherapy comes of age.* Nature, 2011. **480**(7378): p. 480-9.

76. Restifo, N.P., M.E. Dudley, and S.A. Rosenberg, *Adoptive immunotherapy for cancer: harnessing the T cell response.* Nat Rev Immunol, 2012. **12**(4): p. 269-81.

77. Kalos, M. and C.H. June, *Adoptive T cell transfer for cancer immunotherapy in the era of synthetic biology.* Immunity, 2013. **39**(1): p. 49-60.

78. Rosenberg, S.A., et al., *Durable complete responses in heavily pretreated patients with metastatic melanoma using T-cell transfer immunotherapy.* Clin Cancer Res, 2011. **17**(13): p. 4550-7.

79. Brower, V., *The CAR T-Cell Race.* The Scientist, 2015.

80. Hwu, P., et al., *Lysis of ovarian cancer cells by human lymphocytes redirected with a chimeric gene composed of an antibody variable region and the Fc receptor gamma chain.* J Exp Med, 1993. **178**(1): p. 361-6.

81. Hwu, P., et al., *In vivo antitumor activity of T cells redirected with chimeric antibody/T-cell receptor genes.* Cancer Res, 1995. **55**(15): p. 3369-73.

82. Chen, D.S. and I. Mellman, *Oncology meets immunology: the cancer-immunity cycle.* Immunity, 2013. **39**(1): p. 1-10.

83. *The Role of Anti-PD-L1 Immunotherapy in Cancer.* OncLive, 2014.

84. Shi, L., et al., *The role of PD-1 and PD-L1 in T-cell immune suppression in patients with hematological malignancies.* J Hematol Oncol, 2013. **6**(1): p. 74.

85. Kim, J.W. and J.P. Eder, *Prospects for targeting PD-1 and PD-L1 in various tumor types.* Oncology (Williston Park), 2014. **28 Suppl 3**: p. 15-28.

86. Agnew, V., *Long-term results encouraging for combination immunotherapy for advanced melanoma.* Yale News, 2014.

87. Hodi, F.S., et al., *Improved survival with ipilimumab in patients with metastatic melanoma.* N Engl J Med, 2010. **363**(8): p. 711-23.

88. Fellner, C., *Ipilimumab (yervoy) prolongs survival in advanced melanoma: serious side effects and a hefty price tag may limit its use.* P T, 2012. **37**(9): p. 503-30.

89. Chustecka, Z., *FDA Approves Nivolumab, First Immunotherapy for Lung Cancer.* MedScape, 2015.

90. Pan, Q., et al., *Concise Review: Targeting Cancer Stem Cells Using Immunologic Approaches.* Stem Cells, 2015. **33**(7): p. 2085-92.

91. Lu, L., et al., *Cancer stem cell vaccine inhibits metastases of primary tumors and induces humoral immune responses against cancer stem cells.* Oncoimmunology, 2015. **4**(3): p. e990767.

92. Zhou, L., et al., *Promise of cancer stem cell vaccine.* Hum Vaccin Immunother, 2015: p. 0.

93. Ning, N., et al., *Cancer stem cell vaccination confers significant antitumor immunity.* Cancer Res, 2012. **72**(7): p. 1853-64.

94. Teitz-Tennenbaum, S., et al., *Targeting cancer stem cells via dendritic-cell vaccination.* Oncoimmunology, 2012. **1**(8): p. 1401-1403.

95. Dreaden, E.C., et al., *Beating cancer in multiple ways using nanogold.* Chem Soc Rev, 2011. **40**(7): p. 3391-404.

96. Chen, H.W., et al., *Highly crystallized iron oxide nanoparticles as effective and biodegradable mediators for photothermal cancer therapy.* Journal of Materials Chemistry B, 2014. **2**(7): p. 757-765.

97. Makadia, H.K. and S.J. Siegel, *Poly Lactic-co-Glycolic Acid (PLGA) as Biodegradable Controlled Drug Delivery Carrier.* Polymers (Basel), 2011. **3**(3): p. 1377-1397.

98. S.K. Smart, A.I.C., G.Q. Lu, D.J. Martin, *The biocompatibility of carbon nanotubes.* Carbon, 2006. **44**(6): p. 1034-1047.

99. Hirsch, L.R., et al., *Nanoshell-mediated near infrared photothermal tumor therapy.* Proceedings of the 25th Annual International Conference of the Ieee Engineering in Medicine and Biology Society, Vols 1-4, 2003. **25**: p. 1230-1231.

100. Huang, X.H., et al., *Cancer cell imaging and photothermal therapy in the near-infrared region by using gold nanorods.* Journal of the American Chemical Society, 2006. **128**(6): p. 2115-2120.

101. Zhao, Q., et al., *Magnetic nanoparticle-based hyperthermia for head & neck cancer in mouse models.* Theranostics, 2012. **2**: p. 113-21.

102. Jiang, W. and S.P. Schwendeman, *Stabilization of tetanus toxoid encapsulated in PLGA microspheres.* Mol Pharm, 2008. **5**(5): p. 808-17.

103. Chen, J., et al., *Preparation, characterization and transfection efficiency of cationic PEGylated PLA nanoparticles as gene delivery systems.* J Biotechnol, 2007. **130**(2): p. 107-13.

104. Morgen, M., et al., *Polymeric nanoparticles for increased oral bioavailability and rapid absorption using celecoxib as a model of a low-solubility, high-permeability drug.* Pharm Res, 2012. **29**(2): p. 427-40.

105. Gursoy, R.N. and S. Benita, *Self-emulsifying drug delivery systems (SEDDS) for improved oral delivery of lipophilic drugs.* Biomed Pharmacother, 2004. **58**(3): p. 173-82.

106. Chen, H.W., et al., *Living' PEGylation on gold nanoparticles to optimize cancer cell uptake by controlling targeting ligand and charge densities.* Nanotechnology, 2013. **24**(35).

107. Liu, X.S., et al., *Minimizing nonspecific phagocytic uptake of biocompatible gold nanoparticles with mixed charged zwitterionic surface modification.* Journal of Materials Chemistry, 2012. **22**(5): p. 1916-1927.

108. Arvizo, R.R., et al., *Effect of nanoparticle surface charge at the plasma membrane and beyond.* Nano Lett, 2010. **10**(7): p. 2543-8.

109. Adolphi, N.L., et al., *Imaging of Her2-targeted magnetic nanoparticles for breast cancer detection: comparison of SQUID-detected magnetic relaxometry and MRI.* Contrast Media Mol Imaging, 2012. **7**(3): p. 308-19.

110. Oyelere, A.K., et al., *Peptide-conjugated gold nanorods for nuclear targeting.* Bioconjugate Chemistry, 2007. **18**(5): p. 1490-1497.

111. Guo, L., et al., *Combinatorial photothermal and immuno cancer therapy using chitosan-coated hollow copper sulfide nanoparticles.* ACS Nano, 2014. **8**(6): p. 5670-81.

112. Chong, C.S., et al., *Enhancement of T helper type 1 immune responses against hepatitis B virus core antigen by PLGA nanoparticle vaccine delivery.* J Control Release, 2005. **102**(1): p. 85-99.

113. Toraya-Brown, S., et al., *Local hyperthermia treatment of tumors induces CD8(+) T cell-mediated resistance against distal and secondary tumors.* Nanomedicine, 2014. **10**(6): p. 1273-85.

114. van Broekhoven, C.L., et al., *Targeting dendritic cells with antigen-containing liposomes: a highly effective procedure for induction of antitumor immunity and for tumor immunotherapy.* Cancer Res, 2004. **64**(12): p. 4357-65.

115. Hamdy, S., et al., *Co-delivery of cancer-associated antigen and Toll-like receptor 4 ligand in PLGA nanoparticles induces potent CD8+ T cell-mediated anti-tumor immunity.* Vaccine, 2008. **26**(39): p. 5046-57.

116. Braun, G.B., et al., *Laser-Activated Gene Silencing via Gold Nanoshell-siRNA Conjugates.* ACS Nano, 2009. **3**(7): p. 2007-15.

117. Rapoport, N.Y., et al., *Ultrasound-triggered drug targeting of tumors in vitro and in vivo.* Ultrasonics, 2004. **42**(1-9): p. 943-50.

118. Lowery, A., et al., *Tumor-targeted delivery of liposome-encapsulated doxorubicin by use of a peptide that selectively binds to irradiated tumors.* J Control Release, 2011. **150**(1): p. 117-24.

119. Kunii, R., et al., *Particle characteristics and biodistribution of camptothecin-loaded PLA/(PEG-PPG-PEG) nanoparticles.* Drug Deliv, 2008. **15**(1): p. 3-10.

120. Murthy, N., et al., *Design and synthesis of pH-responsive polymeric carriers that target uptake and enhance the intracellular delivery of oligonucleotides.* J Control Release, 2003. **89**(3): p. 365-74.

121. Cai, S., et al., *Localized doxorubicin chemotherapy with a biopolymeric nanocarrier improves survival and reduces toxicity in xenografts of human breast cancer.* J Control Release, 2010. **146**(2): p. 212-8.

122. Hadjipanayis, C.G., et al., *Metallic iron nanoparticles for MRI contrast enhancement and local hyperthermia.* Small, 2008. **4**(11): p. 1925-9.

123. Purushotham, S. and R.V. Ramanujan, *Thermoresponsive magnetic composite nanomaterials for multimodal cancer therapy.* Acta Biomater, 2010. **6**(2): p. 502-10.

124. Zhang, Z., et al., *Mesoporous silica-coated gold nanorods as a light-mediated multifunctional theranostic platform for cancer treatment.* Adv Mater, 2012. **24**(11): p. 1418-23.

125. Choi, H., et al., *Iron oxide nanoparticles as magnetic resonance contrast agent for tumor imaging via folate receptor-targeted delivery.* Acad Radiol, 2004. **11**(9): p. 996-1004.

126. Zou, P., et al., *Superparamagnetic iron oxide nanotheranostics for targeted cancer cell imaging and pH-dependent intracellular drug release.* Mol Pharm, 2010. **7**(6): p. 1974-84.

127. Wang, R.B., P.S. Billone, and W.M. Mullett, *Nanomedicine in Action: An Overview of Cancer Nanomedicine on the Market and in Clinical Trials.* Journal of Nanomaterials, 2013.

128. Powell, A.C., G.F. Paciotti, and S.K. Libutti, *Colloidal gold: a novel nanoparticle for targeted cancer therapeutics.* Methods Mol Biol, 2010. **624**: p. 375-84.

129. Day, E.S., J.G. Morton, and J.L. West, *Nanoparticles for Thermal Cancer Therapy.* Journal of Biomechanical Engineering-Transactions of the Asme, 2009. **131**(7).

130. Hua, D., et al., *Potent tumor targeting drug release system comprising MMP-2 specific peptide fragment with self-assembling characteristics.* Drug Des Devel Ther, 2014. **8**: p. 1839-49.

131. Roomi, M.W., et al., *Patterns of MMP-2 and MMP-9 expression in human cancer cell lines.* Oncol Rep, 2009. **21**(5): p. 1323-33.

132. Foda, H.D. and S. Zucker, *Matrix metalloproteinases in cancer invasion, metastasis and angiogenesis.* Drug Discov Today, 2001. **6**(9): p. 478-482.

133. Murthy, N., et al., *Bioinspired pH-responsive polymers for the intracellular delivery of biomolecular drugs.* Bioconjug Chem, 2003. **14**(2): p. 412-9.

134. Muhammad, F., et al., *pH-Triggered controlled drug release from mesoporous silica nanoparticles via intracelluar dissolution of ZnO nanolids.* J Am Chem Soc, 2011. **133**(23): p. 8778-81.

135. Narayan, M., et al., *Trastuzumab-induced HER reprogramming in "resistant" breast carcinoma cells.* Cancer Res, 2009. **69**(6): p. 2191-4.

136. Burke, A.R., et al., *The resistance of breast cancer stem cells to conventional hyperthermia and their sensitivity to nanoparticle-mediated photothermal therapy.* Biomaterials, 2012. **33**(10): p. 2961-70.

137. Bear, A.S., et al., *Elimination of metastatic melanoma using gold nanoshell-enabled photothermal therapy and adoptive T cell transfer.* PLoS One, 2013. **8**(7): p. e69073.

138. Wang, C., et al., *Immunological Responses Triggered by Photothermal Therapy with Carbon Nanotubes in Combination with Anti-CTLA-4 Therapy to Inhibit Cancer Metastasis.* Advanced Materials, 2014. **26**(48): p. 8154-8162.

139. Hirsch, L.R., et al., *Nanoshell-mediated near-infrared thermal therapy of tumors under magnetic resonance guidance.* Proceedings of the National Academy of Sciences of the United States of America, 2003. **100**(23): p. 13549-13554.

140. Loo, C., et al., *Immunotargeted nanoshells for integrated cancer imaging and therapy.* Nano Letters, 2005. **5**(4): p. 709-711.

141. Li, J.L. and M. Gu, *Gold-Nanoparticle-Enhanced Cancer Photothermal Therapy.* Ieee Journal of Selected Topics in Quantum Electronics, 2010. **16**(4): p. 989-996.

142. Hauck, T.S., et al., *Enhancing the Toxicity of Cancer Chemotherapeutics with Gold Nanorod Hyperthermia.* Advanced Materials, 2008. **20**(20): p. 3832-+.

143. Huang, H.C., K. Rege, and J.J. Heys, *Spatiotemporal temperature distribution and cancer cell death in response to extracellular hyperthermia induced by gold nanorods.* ACS Nano, 2010. **4**(5): p. 2892-900.

144. Huang, X.H., et al., *Determination of the minimum temperature required for selective photothermal destruction of cancer cells with the use of immunotargeted gold nanoparticles.* Photochemistry and Photobiology, 2006. **82**(2): p. 412-417.

145. Mahmood, U. and R. Weissleder, *Near-infrared optical imaging of proteases in cancer.* Molecular Cancer Therapeutics, 2003. **2**(5): p. 489-496.

146. Eustis, S. and M.A. El-Sayed, *Why gold nanoparticles are more precious than pretty gold: Noble metal surface plasmon resonance and its enhancement of the radiative and nonradiative properties of nanocrystals of different shapes.* Chemical Society Reviews, 2006. **35**(3): p. 209-217.

147. Curry, T., et al., *Multifunctional theranostic gold nanoparticles for targeted CT imaging and photothermal therapy.* Contrast Media Mol Imaging, 2014. **9**(1): p. 53-61.

148. Wang, R., P.S. Billone, and W.M. Mullett, *Nanomedicine in Action: An Overview of Cancer Nanomedicine on the Market and in Clinical Trials.* Journal of Nanomaterials, 2013. **2013**: p. 12.

149. Cai, W., et al., *Applications of gold nanoparticles in cancer nanotechnology.* Nanotechnol Sci Appl, 2008. **2008**(1).

150. Robinson, J.T., et al., *High Performance In Vivo Near-IR (> 1 mu m) Imaging and Photothermal Cancer Therapy with Carbon Nanotubes.* Nano Research, 2010. **3**(11): p. 779-793.

151. Zhou, F.F., et al., *Cancer photothermal therapy in the near-infrared region by using single-walled carbon nanotubes.* Journal of Biomedical Optics, 2009. **14**(2).

152. Zhou, F.F., et al., *Mitochondria-Targeting Single-Walled Carbon Nanotubes for Cancer Photothermal Therapy.* Small, 2011. **7**(19): p. 2727-2735.

153. Iancu, C. and L. Mocan, *Advances in cancer therapy through the use of carbon nanotube-mediated targeted hyperthermia.* International Journal of Nanomedicine, 2011. **6**: p. 1675-1684.

154. Moon, H.K., S.H. Lee, and H.C. Choi, *In vivo near-infrared mediated tumor destruction by photothermal effect of carbon nanotubes.* ACS Nano, 2009. **3**(11): p. 3707-13.

155. Huang, N., et al., *Single-wall carbon nanotubes assisted photothermal cancer therapy: animal study with a murine model of squamous cell carcinoma.* Lasers Surg Med, 2010. **42**(9): p. 638-48.

156. Singh, R. and S.V. Torti, *Carbon nanotubes in hyperthermia therapy.* Adv Drug Deliv Rev, 2013. **65**(15): p. 2045-60.

157. Yang, K., et al., *Graphene in mice: ultrahigh in vivo tumor uptake and efficient photothermal therapy.* Nano Lett, 2010. **10**(9): p. 3318-23.

158. Yallapu, M.M., et al., *Multi-functional magnetic nanoparticles for magnetic resonance imaging and cancer therapy.* Biomaterials, 2011. **32**(7): p. 1890-1905.

159. Storm, G., et al., *Surface Modification of Nanoparticles to Oppose Uptake by the Mononuclear Phagocyte System.* Advanced Drug Delivery Reviews, 1995. **17**(1): p. 31-48.

160. Dreaden, E.C., et al., *Size matters: gold nanoparticles in targeted cancer drug delivery.* Ther Deliv, 2012. **3**(4): p. 457-78.

161. Guo, S.T. and L. Huang, *Nanoparticles Escaping RES and Endosome: Challenges for siRNA Delivery for Cancer Therapy.* Journal of Nanomaterials, 2011.

CHAPTER 2. INHIBITION OF EPITHELIAL-LIKE AND MESENCHYMAL-LIKE BREAST CANCER STEM CELLS TO PREVENT METASTASIS THROUGH IRON OXIDE NANOPARTICLE-MEDIATED PHOTOTHERMAL THERAPY

2.1 Abstract

Increasing evidence suggesting breast cancer stem cells (BCSCs) drive metastasis and evade traditional therapies underscores a critical need to exploit the untapped potential of nanotechnology to develop innovative therapies that will significantly improve patient survival. Photothermal therapy (PTT) to induce localized hyperthermia is one of few nanoparticle-based treatments to enter clinical trials in human cancer patients, and has recently gained attention for its ability to induce a systemic response targeting distal cancer cells in mouse models. Here, translational models of triple negative breast cancer are used to demonstrate PTT, mediated by highly crystallized iron oxide nanoparticles, targets two populations of BCSCs and can be combined with surgery to prevent metastasis formation. First, PTT preferentially targets epithelial-like ALDH+ BCSCs compared to mesenchymal-like CD44+/CD24- BCSCs and bulk cells *in vitro*. Second, PTT inhibits breast cancer stem cell self-renewal through reduction of mammosphere formation in primary and secondary generations. Third, secondary implantation reveals the ability of PTT to impede BCSC-driven tumor formation. Finally, PTT before surgery can significantly reduce metastasis to lymph nodes and other distal sites. These results suggest

the feasibility of incorporating PTT into standard clinical treatments such as surgery to enhance BCSC destruction and prevent metastasis, and provide impetus to investigate the potential for PTT to induce systemic BCSC immunity and improve long-term survival in patients with metastatic breast cancer.

2.2 Introduction

Cancer stem cells (CSCs) pose what is arguably the greatest challenge in developing therapies that will truly cure cancer patients. First discovered in 1997 in acute myeloid leukemia by Dick and colleagues [1], soon evidence for a small population of stem-like cells with the ability to drive tumor formation began to arise in solid cancers [2-6].For more than a decade Wicha and others have conducted extensive studies to characterize breast cancer stem cell (BCSC) populations identified by either the Aldefluor enzymatic assay (ALDH+) or the surface receptor phenotype CD44+/CD24- [2, 7-11]. In an effort to better understand the role of BCSCs in tumor growth, dissemination, and metastasis formation, recent genetic profiling by the Wicha group revealed the two BCSC populations are distinct and yet plastically transition from one form to the other as signaled by the tumor microenvironment [12]. The authors report that the ALDH+ BCSCs exist in a mesenchymal-to-epithelial (MET) state and are primarily proliferative and concentrated at the tumor interior. In contrast, the CD44+/CD24- BCSCs exist in an epithelial-to-mesenchymal (EMT) state and are primarily quiescent and concentrated at the tumor invasive edge. Their findings suggest that ALDH+ MET BCSCs and EMT CD44+/CD24- BCSCs may have distinct roles in driving tumor growth and metastasis.

In light of this recent discovery it remains pertinent that future breast cancer therapies not only account for the BCSCs in addition to the differentiated cancer cells [13], but also distinguish the two distinct BCSC populations. However, for most patients it is unlikely the BCSCs will be localized to the primary tumor at the time of treatment. Up to 30% of Stage I breast cancer patients already have micrometastases detectable from bone marrow biopsies [14]. With metastasis being the primary cause of death in breast cancer patients [15, 16], to be most effective future therapies must perform essential two roles: act locally against all populations of cancer cells to prevent future metastasis, and act systemically against all populations of cancer cells in existing metastases. However the resistance of CSCs to traditional therapy such as chemotherapy or radiation, which when used alone can enrich the CSC population [17-19], remains a significant challenge. Therapeutic regimens exploiting advances in nanoparticle development offer a tremendous potential to enhance treatment efficacy against CSCs.

Photothermal therapy (PTT) is one of the few examples of nanoparticle-mediated treatments to enter clinical trials in human cancer patients [20, 21].Gold-based nanoparticles and carbon nanotubes have been the predominant subjects of laboratory investigation to produce heat targeted to kill cancer cells in response to near infrared (NIR) light [21-34]. Similarly, in the presence of an alternating magnetic field, iron oxide nanoparticles have been explored for cancer hyperthermia [21, 35-37]. Such therapy offers several advantages to cancer patients. External control of localized hyperthermia translates to reduced off-target toxicity compared to other intravenously injected therapies (e.g., chemotherapy). Biologics and many small molecule drugs rely on inhibition of a particular molecular pathway, which limits the patient population who will respond to such therapy and can even lead to development of resistant cancer cells that have learned to rely on alternative survival pathways [9, 38]. In contrast, nanoparticle-mediated PTT

offers broader applicability, including difficult-to-treat subtypes such as triple negative breast cancer which lacks estrogen, progesterone, and Her2 receptors exploited for targeted therapy. Development of imagable, targeted nanoparticles may even allow for localized PTT at sites of macrometastases. Perhaps most promising are the initial findings that nanoparticle-mediated hyperthermia induces a systemic cancer-specific immune response in which cytotoxic T-cells are trained to recognize and inhibit distal cancer cells [36], a response that may be strengthened by coupling with immunotherapy [32, 39], suggesting the potential to inhibit already formed micro- and macrometastases in human patients.

Extensive research into the effects of photothermal therapy on CSCs will become critical as basic research and clinical studies suggest its feasibility in human patients with local and metastatic cancers. PTT was first realized into a commercial therapy applicable to cancer patients through AuroLase Therapy, which uses silica-cored gold nanoshells [40]. Clinical trials began in patients with head and neck cancer and more recently expanded to patients with primary and/or metastatic lung tumors [41, 42]. In *Science Translational Medicine* Atkinson et al conducted an elaborate study using patient-derived xenografts, revealing that mild hyperthermia (42 °C) via Aurolase therapy can sensitize MET ALDH+ BCSCs to ionizing radiation (IR). They found PTT impairs their ability to repair double-stranded breaks in DNA caused by IR, which was suggested to be the result of changes in heat shock protein expression caused by PTT [18]. However, it remains unclear whether differences exist in the sensitivities of MET and EMT BCSCs to PTT alone.

Previous studies examining the effects of nanoparticle-mediated hyperthermia alone on CSCs have been conducted using models that are more difficult to interpret whether the results would translate to human cancers: using a Ecadherin knockdown model to examine CSCs

separately rather than grown in the presence of differentiated cancer cells [43], exposing cells to nanoparticles *in vitro* before injecting them to mice for *in vivo* hyperthermia [26], or evaluating tumor growth on cells that received nanoparticle-mediated hyperthermia *in vitro* before implantation into mice [44]. There is a need for rigorous analysis using functional assays to evaluate treatment effect on stem cell properties such as self-renewal and tumor initiating frequency of treated tumors. Further investigation, particularly using translational *in vivo* models, is required to better characterize the effect of photothermal therapy on BCSCs and, consequently, to inhibit cancer metastasis to ultimately improve survival.

Photothermal therapy may be a prime candidate for inclusion in cancer therapy that is effective in the two essential roles to eliminate both MET and EMT BCSCs as well as differentiated cancer cells, both locally and systemically. Here we sought to establish the efficacy of PTT in this first role, laying the foundation for future investigations into its systemic potential. We conduct a rigorous analysis of the local effects of PTT, providing rationale for incorporating it into standard breast cancer therapy – to inhibit BCSCs at the primary tumor site to prevent future metastasis. As such, we sought to discern the sensitivities of both MET and EMT BCSCs to various clinically relevant PTT conditions. Our lab has previously demonstrated the ability to treat mice bearing orthotopic tumors derived from human breast cancer cells via photothermal therapy mediated by biodegradable highly crystallized iron oxide nanoparticles (HCIONPs). In contrast to most PTT mediators, the HCIONPs produced by our lab are capable of magnetic resonance imaging (MRI) and efficient intratumoral accumulation following tail vein injection [45]. Here we conduct translational studies to evaluate the effect of PTT via HCIONPs on BCSCs in order to prevent the spread of metastasis from the primary tumor site. Our work focuses on triple negative breast cancer (TNBC), which is generally more aggressive

and metastatic than other subtypes. We reveal *in vitro* that PTT eliminates MET BCSCs with the greatest sensitivity and identify conditions in which EMT BCSCs are also eliminated preferentially to differentiated cancer cells. For the first time, we show that PTT inhibits breast cancer stem cell self-renewal *in vitro*. Through secondary implantation we demonstrate the ability of *in vivo* PTT to inhibit BCSCs in triple negative breast tumors. Finally, we show *in vivo* that addition of PTT to standard surgical treatment can reduce metastasis formation in TNBC. Combining these results with further studies to employ PTT to induce a systemic immune response capable of inhibiting BCSCs at metastatic sites could address an unmet need in breast cancer to develop novel therapies that effectively eradicate existing micro- and macrometastases and prevent future metastasis.

2.3 Results

HCIONPs enable selective hyperthermia of cell culture medium under near-infrared laser light: Our lab previously demonstrated the ability to use biodegradable, highly crystallized iron oxide nanoparticles (HCIONPs) coated with antifouling polymer for photothermal therapy *in vivo* [45]. The intravenously injected HCIONPs effectively accumulate in breast cancer tumors via the enhanced permeation and retention (EPR) effect [45-47], and their highly crystallized structure enables effective tumor heating upon stimulation by near infrared (NIR) light.

Here we compared heating curves on 96-well plates containing cell culture medium spiked with HCIONPs or PBS (Laser Only control). We hypothesized that conducting PTT at increasing laser powers for our *in vitro* studies would allow us to determine whether a difference

exists in the sensitivities of BCSCs and differentiated cancer cells. As shown in Figure 2.1A, laser powers less than 0.5 W, designated P1, P2, and P3, are sufficient to trigger hyperthermia up to 42, 45, and 48 °C after 10 minutes of laser irradiation in medium containing HCIONPs. In contrast, the same laser powers result in minimal temperature increases in control media without HCIONPs.

PTT by HCIONPs inhibits cell viability of triple negative breast cancer cells: The majority of our studies were conducted using the human SUM159 breast cancer cell line, which is triple negative and has quantifiable populations of both ALDH+ and CD44+/CD24-/EpCAM+ BCSCs [48]. For our first *in vitro* study we investigated the effect of HCIONP-mediated photothermal therapy (10 min) at P1, P2, and P3 laser powers on SUM159 cell viability after 72 h, as shown in Figure 2.1B. Control treatments tested include Laser Only (P1, P2, P3), HCIONPs Only, and Non-Treated. While cell viabilities after Laser Only and HCIONPs Only control treatments are not statistically different from the Non-Treated group, a dose-dependent decrease is observed for PTT-treated cells irradiated at increasing laser powers in the presence of HCIONPs. Significant decreases in viability are observed after irradiation at power levels P1 and P2, but some cells are able to survive and proliferate within 72 h. This capacity is abrogated by PTT at P3, for which the relative number of viable cells is 4.7% of the Non-Treated control.

MET BCSCs are preferentially sensitive to PTT: Next we performed flow cytometry on PTT-treated SUM159 cells to examine the relative sensitivities of the ALDH+ epithelial-like (MET) BCSCs and CD44+/CD24-/EpCAM+ mesenchymal-like (EMT) BCSCs to each other and the bulk cancer cells. Cells were counted and bulk viability determined 24 hours following PTT, prior to quantification of each BCSC population by flow cytometry. As shown in Figure 2.2A, a dose-dependent decrease the ALDH+ MET BCSC percentage occurs for 10 min PTT at

increasing laser powers. PTT significantly decreases the percentage of ALDH+ BCSCs using the P2 laser power while the P3 power is required to significantly decrease cell viability (Figure 2.2C), suggesting an increased sensitivity compared to bulk cancer cells. The significant decrease in CD44+/CD24-/EpCAM+ EMT BCSC absolute number, but not percentage, at the P3 laser power (Figure 2.2B) suggests that the sensitivity of EMT CSCs is similar to the bulk cancer cells after 10 min PTT. Control treatments with P3 Laser Only and HCIONPs Only do not affect either BCSC population (Figure 2.S1).

An enhancement of BCSC sensitivity to PTT relative to bulk cancer cells is more apparent after 20 min irradiation using the same laser powers. Hyperthermia at the P1 laser power reveals that a significant decrease in the percentage of ALDH+ MET CSCs (Figure 2.2D) occurs without a significant decrease in the overall cell viability (Figure 2.2F). Increasing the irradiation time to 20 minutes also enhances the sensitivity of EMT CSCs, for which a significant difference in percentage and absolute number is observed after P2 PTT compared to the Non-Treated group (Figure 2.2E).

Mammosphere formation reveals PTT inhibits BCSC self-renewal: We next employed the mammosphere assay, the classic *in vitro* functional BCSC assay, to evaluate the effect of HCIONP-mediated PTT on BCSC self-renewal. Treatment is performed in non-adherent conditions in medium lacking serum, and stem cells that survive form three-dimensional mammospheres. These primary spheres are then passaged and re-plated, without further treatment, to form secondary mammospheres. A reduction in secondary mammosphere formation suggests inhibition of CSC self-renewal.

Here, for the first time, the effect of PTT on BCSC self-renewal is studied based on the formation of secondary mammospheres. Our lab has found that the SUM159 cell line is one of few not ideally suited for the mammosphere assay, as nearly all cells able to survive and form spheres (data not shown). Instead, MCF7 breast cancer cells were selected to assess the effect of PTT on mammosphere formation by BCSCs [49, 50]. Primary mammospheres were quantified and imaged seven days after treatment of single cells (10 min). As shown in Figure 2.3A, only PTT treatment with both HCIONPs and laser irradiation results in a significant decrease in primary mammosphere formation, which occurs in a dose-dependent manner with increasing laser power. Furthermore, increases in laser power reduce mammosphere size in addition to mammosphere number, as shown in Figure 2.3B. Control treatments with P3 Laser Only and HCIONPs Only do not affect mammosphere formation or size (Figure 2.S2).

Following counting and imaging, the primary mammospheres were collected, dissociated into single cells, and re-plated to quantify CSC self-renewal to form secondary mammospheres over seven days. As shown in Figures 2.3C and 2.3D, secondary spheres are significantly reduced in number and size in the P1 PTT treatment group. Most secondary spheres from the P2 PTT treatment group just met the size threshold for counting (45 μM). In the P3 PTT treatment group, of the few primary spheres large enough to be collected and re-plated as single cells their ability to form secondary spheres was completely abrogated.

PTT delays BCSC-driven tumor formation after secondary implantation: The functional assay for inhibition of CSCs *in vivo* is secondary implantation, which assesses the degree to which treatment affects the CSCs' ability to self-renew and differentiate to drive tumor formation in immunodeficient mice. Treated tumors are removed from primary mice and isolated as single cells for implantation at limiting dilutions into non-treated secondary mice, to

calculate a tumor initiating cell frequency [2, 7, 9]. Here we performed PTT in mice bearing orthotopic SUM159 tumors as previously described by our lab [45] using immunodeficient NOD/SCID mice. Tumors of primary mice were subjected to 1.0 W and 0.5 W PTT (10 min), resulting in final tumor temperatures of 60 ± 5 °C and 42 ± 2 °C, respectively. Mice were sacrificed 72 h after PTT to remove tumors for secondary implantation at dilutions of 50, 500, and 5,000 cells per injection per treatment group.

Secondary tumor volumes up to 50 days post-implantation of 500 and 5,000 cells are shown in Figures 2.4A-B. The data clearly show that both 1.0 W and 0.5 W PTT delay secondary tumor formation and result in smaller tumor sizes than in secondary mice in the Non-Treated group, as also demonstrated by the representative images in Figures 2.4C-D. At the 50 cell dilution secondary tumors only formed in Non-Treated mice. As shown in Figure 2.4E, extreme limiting dilution analysis [51] of secondary tumor formation for all three dilutions reveals a significant difference among treatment groups at Day 30 ($p < 0.01$) and Day 40 ($p < 0.001$). However, optimization of PTT conditions (e.g., increasing irradiation time) may be required to enhance the effect on ultimate tumor formation and tumor initiating cell frequency.

PTT reduces metastasis formation in axillary lymph nodes: Based on our observations that SUM159 cells can metastasize to axillary lymph nodes, for our final study we sought to demonstrate that PTT can be used to perform the previously described first essential role of cancer therapy – to act locally against all populations of cancer cells to prevent future metastasis. Wanting to incorporate PTT into a clinically relevant model, we hypothesized that inhibition of BCSCs by PTT would prevent metastasis from spreading from the primary tumor when applied before surgery. Accordingly, NOD/SCID mice were inoculated with Luciferase-transfected SUM159 cells and monitored via an *in vivo* imaging system (IVIS) to track primary tumor and

metastatic development after treatment. Mice received either PTT (0.5 W, 10 min) ten days prior to surgical tumor resection (PTT + SR), or surgery without PTT (SR Only). As denoted in the bioluminescence imaging scheme in Figure 2.5A, mice in both treatment groups (n=8) were imaged immediately following PTT (Figure 2.5B) and weekly following removal of surgical wound clips. Despite our best efforts to remove all tumor tissue during surgery, initial imaging following surgery revealed virtually all tumors growing back in both groups (Figure 2.S3). Metastasis formation was tracked by IVIS for six weeks following PTT and confirmed via necropsy and staining for AE-1/AE-3 to detect the presence of human SUM159 cells (Figure 2.S4) [52]. As shown in Figures 2.5B – 2.5D, PTT before surgery significantly reduces the proportion of mice that ultimately develop metastases ($p < 0.05$), presumably by reducing the proportion of EMT BCSCs within the residual primary tumor. The incidence of lymph node metastasis was 25% in mice that received PTT versus 62.5%, with the majority of these mice containing additional metastatic growths (1/2 in PTT+SR, 4/5 in SR Only).

2.4 Discussion

Here we conduct translational studies to rigorously analyze the ability of PTT via highly crystallized iron oxide nanoparticles to inhibit two breast cancer stem cell populations (ALDH+, CD44+/CD24-/EpCAM+) in TNBC *in vitro* and *in vivo*, to prevent metastasis spread from primary tumors when used in combination with surgery. The use of HCIONPs for PTT via NIR laser light is beneficial for clinical translation for multiple reasons. Compared to the AuroLase gold nanoshells that are 150 nm in diameter, the smaller size of our stealthy HCIONPs facilitates efficient tumor accumulation after intravenous injection due to the enhanced retention and

permeability (EPR) effect [53, 54]. However, all nanoparticles will undergo significant uptake in off-target organs due to the reticuloendothelial system (RES) or mononuclear phagocyte system (MPS) [54-56], suggesting another advantage of the biodegradable HCIONPs [45] over biocompatible gold-based nanoparticles [18, 57, 58]. While iron oxide nanoparticles (IONPs) have been more often investigated for cancer hyperthermia by employing an alternating magnetic field, the translation of this approach to humans is limited. The inability to localize this therapy to the tumor tissue generally requires the particles be intratumorally injected [36, 37] to avoid off-target heating in other organs where IONPs accumulate after intravenous injection.

Here we show that HCIONPs enable selective heating of cell culture medium in response to near infrared (885 nm) laser irradiation, which can be tuned to precisely control PTT temperatures to kill cancer cells. A dose-dependent inhibition of SUM159 cell viability is observed with increasing PTT laser power (P1 – P3) 72 h after treatment. PTT at P3 reduces the viability to 4.7% of the Non-Treated control, suggesting that HCIONP-mediated hyperthermia for only 10 minutes can eliminate proliferation of triple negative breast cancer cells *in vitro*. This is not surprising considering the findings by Burke et al, who compared carbon nanotube-mediated PTT and conventional hyperthermia by water bath. Investigating two settings for rate of temperature increase (ROTI) by water bath on a suspension of breast cancer stem-like cells ($HMLER^{shEcaderin}$), they showed that hyperthermia induced by NIR-responsive nanoparticles enhances cytotoxicity compared to water bath-mediated hyperthermia at equivalent exposure times and temperatures [43]. While rapid heat transfer from PTT causes the overall solution temperature to become mildly hyperthermic [59], the cytotoxic effect will be amplified by the presence of HCIONPs in close proximity to the cells as the heat transfer is significantly greater at the nanoparticle surface [60].

Next we sought to evaluate the effect of HCIONP-mediated PTT on the distinct epithelial-like and mesenchymal-like BCSCs [12]. Decreases in the percentages of SUM159 ALDH+ MET BCSCs after 10 and 20 min PTT at increasing laser powers (P1-P3) reveals an increased sensitivity of this highly proliferative BCSC population to HCIONP-mediated hyperthermia compared to the bulk cell line. While Atkinson et al demonstrated that gold nanoshell-mediated PTT and ionizing radiation together reduce the percentage of ALDH+ BCSCs in patient-derived xenografts [18], this is the first report that PTT alone can reduce ALDH+ CSCs in human breast cancer cells. When we examined the CD44+/CD24-/EpCAM+ EMT BCSCs, we found their number decreases in proportion to bulk cancer cells after 10 min PTT. A significant decrease in EMT BCSC percentage is observed at the P2 laser power after 20 min PTT; this suggests preferential elimination of both BCSC populations is possible within breast tumors with optimization of PTT conditions, especially considering recent findings that EMT BCSCs are more localized at the invasive edge [12] where the nanoparticles will easily accumulate within the tumor tissue. Hyperthermia has been known to trigger several cellular and molecular changes, including impairment of protein and DNA/RNA synthesis, protein denaturation and aggregation, inhibition of repair enzymes, and induction of heat shock protein synthesis [30, 61]. Due to their highly proliferative nature, as determined by elevated ki-67 expression [7, 12], it is conceivable that the enhanced sensitivity of the ALDH+ BCSCs to hyperthermia is due to damaged proteins necessary to meet high metabolic demands and to coordinate DNA replication and repair. Further investigations into the response of heat shock proteins within each breast cancer cell subtype may also provide insight into differences in sensitivity to nanoparticle-mediated hyperthermia [18].

Previous studies of nanoparticle-mediated hyperthermia have yet to examine the treatment's effect on CSC self-renewal by evaluating mammosphere formation beyond the primary generation. In the assay adapted by Dontu and colleagues [62, 63], single cells are plated at clonal densities in non-adherent conditions in medium containing growth factors but lacking serum. The result is massive anoikis. The surviving cells grow in three-dimensional colonies, termed mammospheres, that are enriched in stem cells. First studied using human mammary epithelial cells, the cells from these colonies are able to differentiate into all three types of mammary epithelial lineages and able to self-renew to form mammospheres after serial passaging. To suggest inhibition of BCSC self-renewal, treatment applied to the primary generation of sphere-forming cells must result in a decrease in mammosphere formation in subsequent generations.

By conducting PTT at increasing laser powers, we show that PTT reduces both the number and size of primary MCF7 mammospheres formed in a dose-dependent manner. This observation is most apparent after heating at P3, which after seven days resulted in few primary mammospheres large enough to collect and passage for the second generation. For the first time we demonstrate the ability of PTT to inhibit secondary mammosphere formation, showing that the effect is again dose-dependent. Most secondary spheres in the P2 PTT treatment group are just larger than our 45 μm threshold. Consistent with the proliferation study, P3 PTT treatment is the most drastic; it completely abrogates self-renewal to form secondary spheres.

Removal of treated primary tumor cells for secondary implantation at limiting dilutions into immune-compromised mice has become the gold standard for *in vivo* efficacy of treatment on CSCs [64, 65]. Here we conduct the first study of secondary implantation from mice solely treated with nanoparticle-mediated hyperthermia, using NOD/SCID mice bearing SUM159

tumors subjected to 10 min PTT. While significant decreases are observed in secondary tumor volumes and tumor formation rates at 30 and 40 days post-implantation of PTT-treated primary tumor cells, ultimate secondary tumor formation rates may have been affected by a very small population of residual progenitor or cancer stem cells. While PTT conditions may need to be fine-tuned (e.g., increase laser irradiation time) to obtain optimal results, it is clear the ability of BCSCs to drive tumor formation is hindered following PTT. Interestingly, in contrast to our previous study in nude mice [45], with all other variables the same except tumor size at the time of treatment (100 vs 40 mm^3), 1.0 W PTT was unable to reduce tumor growth in primary NOD/SCID mice (data not shown). Despite repeating treatment in NOD/SCID mice with smaller tumors, 1.0 W PTT was unable to prevent tumor growth. These contrasting effects in secondary versus primary mice are consistent with observations made for primary tumor treatments that specifically target CSCs [66]. Taken together, this *in vivo* data suggests two important features of PTT treatment: 1) consistent with our *in vitro* data, BCSCs are more sensitive to PTT *in vivo* than differentiated cancer cells comprising the bulk of the primary tumor, and 2) PTT alone is not sufficient to eliminate the bulk of differentiated cancer cells in mice with highly compromised immune systems.

Several factors beyond application time and temperature may play a role in the degree of response observed after PTT treatment of primary tumors. For instance, the ability of the photo-responsive nanoparticles to extravasate deep into tumor tissue will affect the heating distribution by the laser light. Likewise, in terms of clinical translation, the depth of laser light penetration will dictate the efficiency to heat various types of tumors depending on their location within the human body. In our current study, the variable that differed from our previous study, in which significant tumor reduction was observed following PTT in nude mice, was the immune

functionality of the mice. Our data combined suggest that the immune function of the mice plays a role in the ability to shrink primary tumors following PTT. Others have recently reported that in immune-competent mice proinflammatory cytokines and chemokines released by dying cells after nanoparticle-mediated hyperthermia trigger a tumor-specific immune response [36, 39], suggesting the importance of mouse model selection given the purpose of the intended study. While future studies of photothermal cancer therapy alone may be more efficacious in immune-competent mice, and in fact may be enhanced if coupled with immunotherapy [32, 39], immune-compromised NOD/SCID mice make it possible to discern the effect strictly from hyperthermia on both stem-like and differentiated cancer cells.

The advancement to a metastatic disease, which eventually occurs for many women diagnosed with early stage breast cancer, is the primary cause of death in women with breast cancer [15, 67]. While patients diagnosed with metastatic breast cancer are currently considered incurable, palliative treatment options exist [15, 67, 68]. For breast cancer patients with less advanced disease, first-line therapy generally includes surgery and depends on factors such as the type of breast cancer, stage, and grade; preceding or following surgery, patients may also receive radiation, chemotherapy, hormone/endocrine therapy, or biologics (Herceptin). Given the evidence suggesting that CSCs are the culprit responsible for metastasis and are resistant to and possibly enriched by chemotherapy and radiation [17-19, 69], there is a critical need to develop first-line breast cancer therapy that is effective in two roles: eliminating all types of cancer cells, including CSCs, at the primary tumor site to prevent future metastases, and eliminating all types of cancer cells at existing metastatic sites. While extensive research is still required, initial reports that nanoparticle-mediated PTT can inhibit CSCs and induce a systemic cancer-specific immune response [32, 36, 39] suggest it may be a prime candidate to meet both components of

this critical unmet need. In light of our results demonstrating PTT inhibition of MET and EMT BCSCs, we sought to demonstrate that PTT could prevent metastasis after treatment of the primary tumor.

In our final study, we examined metastasis development in NOD/SCID mice containing Luciferase-transfected SUM159 tumor xenografts treated with PTT ten days before surgical resection. IVIS imaging revealed PTT before surgery significantly reduces the percentage of mice with macrometastases, presumably by reducing the proportion of BCSCs within the residual primary tumor. Considering these and the findings by Atkinson and colleagues, incorporating nanoparticle-mediated PTT into routine breast cancer therapy such as surgery may improve long-term patient outcomes by avoiding sparing or enriching the CSC population. However, it will be critical to conduct future studies in immune-competent mice to demonstrate the potential to combine PTT with clinically-used therapies to inhibit not only BCSCs located at the primary tumor site but those at distal sites by evoking a cancer/CSC-specific immune response.

2.5 Conclusions

In this study we evaluate the ability of photothermal therapy via highly crystallized iron oxide nanoparticles to inhibit breast cancer stem cells to prevent metastasis following treatment of the primary tumor. Here we conduct rigorous, translational studies to evaluate the effect of PTT via HCIONPs on BCSCs, including both MET and EMT BCSC populations, in triple negative breast cancer *in vitro* and *in vivo*, and combine PTT with surgical resection to prevent lymph node and other metastasis. We reveal *in vitro* that PTT eliminates MET BCSCs with the

greatest sensitivity and identify conditions in which EMT BCSCs are also eliminated preferentially to differentiated cancer cells. For the first time, we show that PTT inhibits breast cancer stem cell self-renewal *in vitro*. Through secondary implantation we demonstrate that PTT impedes BCSC-driven tumor formation. Finally, we show that PTT before surgery significantly reduces metastasis development in TNBC. Taken together, these results suggest the potential to combine nanoparticle-mediated photothermal therapy with current clinical treatments such as surgery to enhance CSC destruction and improve long-term survival in breast cancer patients.

2.6 Materials and Methods

Preparation of HCIONPs: Polymer-coated HCIONPs were prepared as previously described by our lab. Briefly, HCIONPs (15 nm diameter) were synthesized in organic solvent by thermal decomposition [45]. Single core nanocrystals were rendered soluble in aqueous solution after coating with diblock copolymer poly(ethylene oxide)-b-poly(γ-methacryloxypropyl trimethoxysilane)(PEO-b- PγMPS), which is synthesized by reversible addition fragmentation chain transfer (RAFT) polymerization, and purifying by a magnetic separator (Frantz laboratory) [45, 70]. The iron concentration of the resultant solution was determined using o-phenanthroline as previously described [45]. HCIONPs were diluted in phosphate buffered saline (PBS) for *in vitro* and *in vivo* studies.

Photothermal effect of HCIONPs in vitro: For all *in vitro* studies, HCIONPs were suspended in cell culture medium (0.1 mg Fe/mL, 200 μL/well) on a 96-well plate resting on a hot plate set to 37 °C. The solution was heated by a NIR laser (885 nm, spot size 5x8 mm^2, MDL-III-885, OPTO Engine LLC, Midvale, UT) at increasing powers for 10 minutes and the

temperature recorded each minute using an infrared camera (FLIR Systems, i7, Boston,MA). Laser powers were identified to produce heating curves achieving final temperatures of 42, 45, and 48 °C (0.34, 0.42, and 0.49 W, respectively).

Cell Culture: SUM159 and MCF7 breast cancer cells were grown as adherent monolayers incubated at 37 °C with 5% CO_2. Ham's F12 medium was supplemented with 5% fetal bovine serum, 1% antibiotic-antimycotic, 5 µg/mL insulin, 1 µg/mL hydrocortisone, and 4 µg/mL gentamicin for SUM159 cell culture. Eagle's Minimum Essential Medium (EMEM) was supplemented with 10% fetal bovine serum, 1% antibiotic-antimycotic, and 10 µg/mL insulin for MCF7 culture.

Alamar Blue Cell Viability Studies: SUM159 cells were seeded at 1,000 cells/well in 200 µL on a 96-well plate and were treated the following day. After returning to the incubator for 72 h, 20 µL of alamarBlue reagent (AbD Serotec, Raleigh, NC) were added to each well and the fluorescence was measured 4 h later (540/25 nm excitation, 590/20 nm emission, 570 nm mirror) using a BioTek micro-plate reader (Synergy 2).

Flow Cytometry: Suspensions of SUM159 cells (500,000/well) were treated (0.34, 0.42, 0.49 W) in a 96-well plate. After PTT the cells were collected, added to 25 cm^2 flasks, and allowed to recover overnight. The following day cells were collected and counted using Trypan Blue before dividing into separate tubes to stain for ALDH+ CSCs and CD44+/CD24-/EpCAM+ CSCs. The Aldefluor Assay (StemCell Technologies, Durham, NC) was conducted according to the manufacturer's instructions. Antibodies used were CD44-APC, CD24-FITC, EpCAM-PE-Cy7 (BD), which incubated for 30 min on ice with cells in HBSS + 2% FBS. DAPI was used for cell viability. Samples were run on a FACSCanto II (BD) to collect 10,000 live cells, and

analyzed using Flowing Software 2.5.1 (Perttu Terho, Turko Centre for Biotechnology, University of Turko, Finland).

Mammosphere Assay: Mammosphere culture was conducted in Mammary Epithelial Basal Medium (MEBM) supplemented with 1% antibiotic-antimycotic, 5 μg/mL insulin, 1 μg/mL hydrocortisone, and 4 μg/mL gentamicin, 0.02 μg/mL epidermal growth factor (EGF), 0.02 μg/mL basic fibroblast growth factor (bFGF), B27 (Invitrogen), 1:25,000,000 β-mercaptoethanol [49]. For PTT, suspensions of MCF7 cells (100,000/well) were heated in an ultralow adhesion 96-well plate. To achieve final temperatures of 42, 45, and 48 °C on the ultralow plate required laser powers, designated P1-P3, of 0.37, 0.52, and 0.66 W, respectively. After PTT the cells were collected and added to an ultralow adhesion 6-well plate at a density of 6,000 cells in 2 mL mammosphere medium per well. Primary spheres were allowed to form for seven days and then were counted and imaged using an inverted microscope (Nikon TE 2000S). The medium from each well was then passed through a 40 μM strainer to collect the mammospheres, which were dissociated into single cells. The single cells were counted and re-plated on a fresh ultralow adhesion 6-well plate (non-treated, 42 °C PTT, and 45 °C PTT treatment groups) or 96-well plate (48 °C PTT treatment group). Secondary mammospheres were allowed to form for seven days before counting and imaging.

Mouse Models for PTT: All mouse studies were conducted in accordance with a standard animal protocol approved by the University of Michigan University Committee on the Use and Care of Animals. Five week old NOD/SCID (non-obese diabetic/severe combined immunodeficient) mice were obtained from Harlan laboratories. Primary xenograft tumors were formed in the no 4 inguinal mammary pad by orthotopic injection of $0.5x10^6$ SUM159 cells suspended in matrigel. Upon the detection of palpable tumors, tumor volumes were calculated

according to the following equation: volume = 0.5 x length x (width)^2. Mice were divided into treatment groups (n = 5) once tumor volumes reached ~100 mm^3. PTT for all *in vivo* studies was conducted as previously described [45]. Briefly, mice were intravenously injected with HCIONPs by tail vein (20 mg Fe per kg mouse body weight). Following anesthesia 48 h later, the NIR laser was applied for 10 min. Tumor surface temperatures were continuously monitored using an infrared camera (FLIR Systems, i7, Boston, MA).

Secondary Implantation Studies: Primary mice were subjected to ten minute PTT using laser powers of 1.0 W or 0.5 W (2.5 W/cm^2 or1.25 W/cm^2 irradiance, respectively). Mice were humanely euthanized 72 h after PTT, and tumors were harvested and digested using a gentleMACS Octo Dissociator (MACS Miltenyi Biotec, San Diego, CA) according to the manufacturer's protocol. Single tumor cells were counted, stained with DAPI to isolate viable cells and H2K[d]-APC to discriminate mouse cells, and sorted on a FACSAria III (BD). DAPI-/H2K[d]- cells were pooled from each tumor per treatment group and injected double-sided into the no 4 mammary fat pads of secondary NOD/SCID mice (five weeks) in limiting dilutions (5,000, 500, 50 cells).

Metastasis Studies: Luciferase-expressing SUM159 cells [9] were used for xenograft tumor formation. Mice were randomly divided into treatment groups (n = 8) once tumor volumes reached ~75 mm^3. Mice were imaged using an IVIS 200 and Living Image software (PerkinElmer, Waltham, MA) one day following PTT (0.5 W). Ten days following PTT (tumors < 1 cm diameter), tumor resections were performed using a high temperature cauterizer (Bovie Change-A-Tip, Clearwater, FL). Mice were monitored weekly by IVIS for metastasis formation following removal of surgical wound clips, and sacrificed at six weeks post-PTT due to tumor burden. Results of IVIS bioluminescence images were confirmed via necropsy and Pan-

cytokeratin (AE1/AE3) staining of metastatic tissues following fixation in formalin and embedding in paraffin.

Statistical Analysis: All data are represented as mean ± standard deviation. The significance values of data sets with more than two groups were calculated using Minitab software via one-way analysis of variance (ANOVA) followed by Dunnett's post-hoc comparisons to the non-treated control, and proportions were compared via the Chi-square test [71]. Statistical analysis of limiting dilution transplantation data was conducted using Extreme Limiting Dilution Analysis (ELDA) software as described by Hu and Smith [18, 51]. A $p < 0.05$ was considered statistically significant.

2.7 Figures

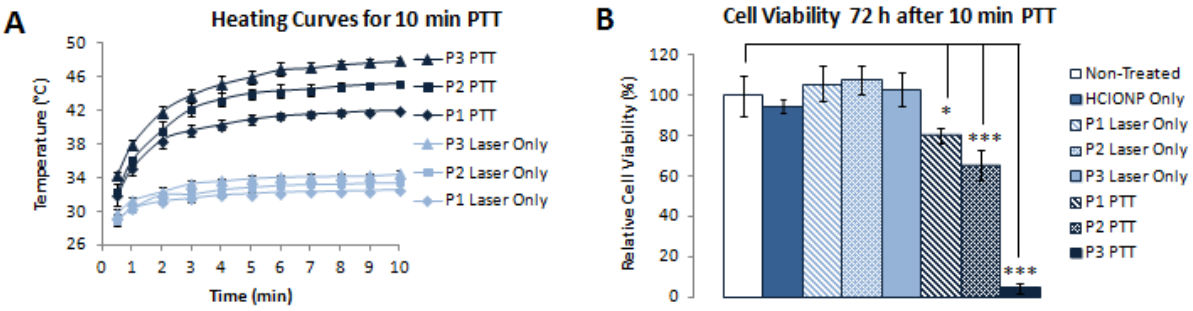

Figure 2.1. (A) Ten minute heating curves of SUM159 medium subjected to PTT (Laser + HCIONPs), compared to Laser Only controls. Laser powers tested were 0.34, 0.42, 0.49 W, designated P1, P2, P3, respectively. Solutions were spiked with HCIONPs (0.1 mg Fe/mL) for PTT or PBS for Laser Only control treatment. (B) SUM159 cell viability determined by alamarBlue 72 h after PTT (10 min) at P1, P2, and P3 laser powers, compared to IONP Only, Laser Only (P1-P3), and Non-Treated controls. Addition of alamarBlue Reagent results in a colorimetric change that is proportional to the number of metabolically active cells. * $p< 0.05$, ** $p < 0.01$, *** $p < 0.001$ via Dunnett's post-hoc comparison to Non-Treated control.

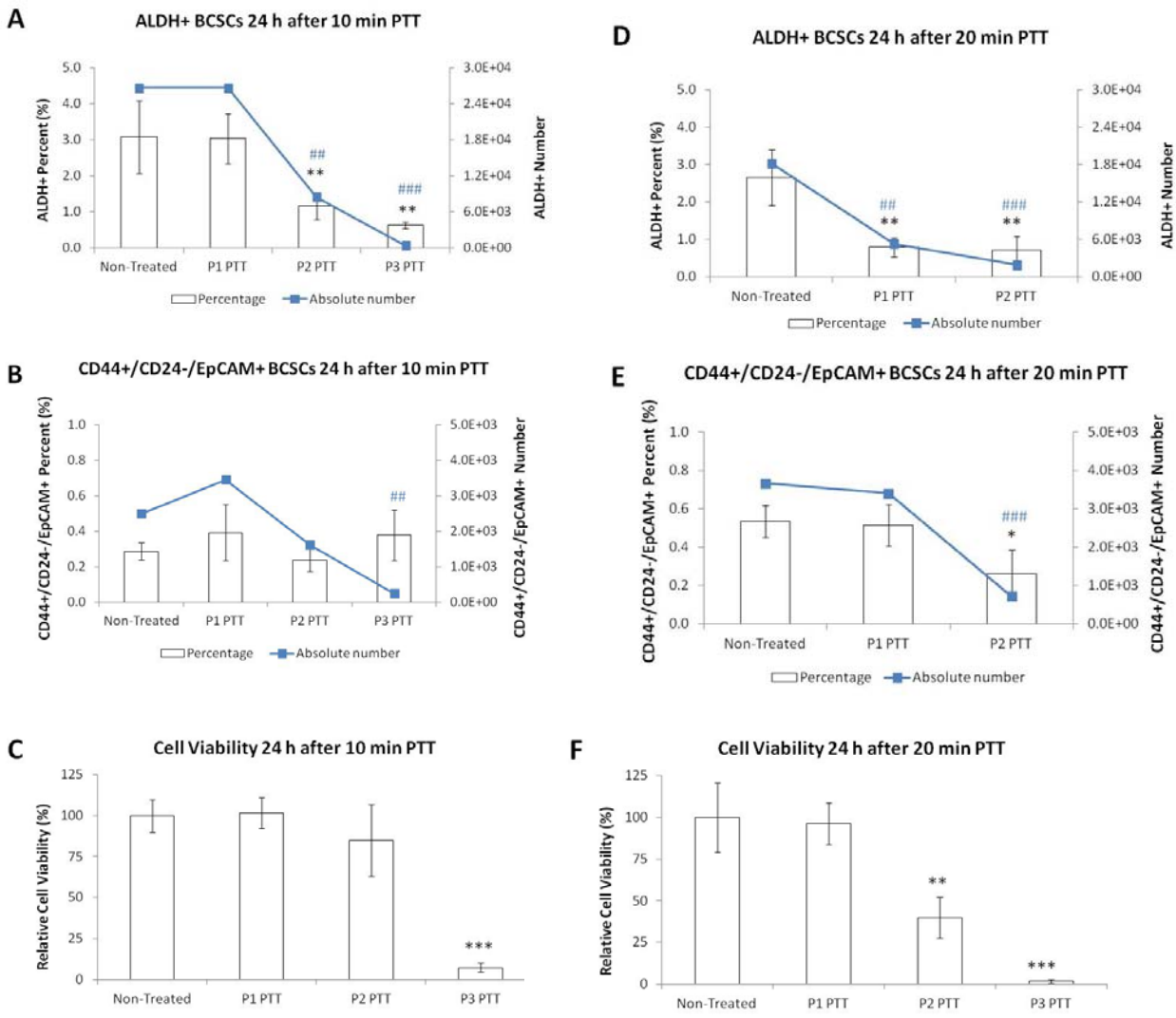

Figure 2.2. SUM159 cell viability 24 h after 10 min (A) and 20 min (D) PTT. MET-like ALDH+ BCSC percentage and absolute number 24 h after 10 min (B) and 20 min (E) PTT. EMT-like CD44+/CD24-/EpCAM+ BCSC percentage and absolute number 24 h after 10 min (C) and 20 min (F) PTT. It should be noted that after 20 min PTT at P3, the number of viable cells was insufficient for analysis by flow cytometry. For cell viabilities and percentages of BCSCs, * $p < 0.05$, ** $p < 0.01$, *** $p < 0.001$ via Dunnett's post-hoc comparison to Non-Treated control. For absolute numbers of BCSCs, # $p < 0.05$, ## $p < 0.01$, ### $p < 0.001$ via Dunnett's post-hoc comparison to Non-Treated control.

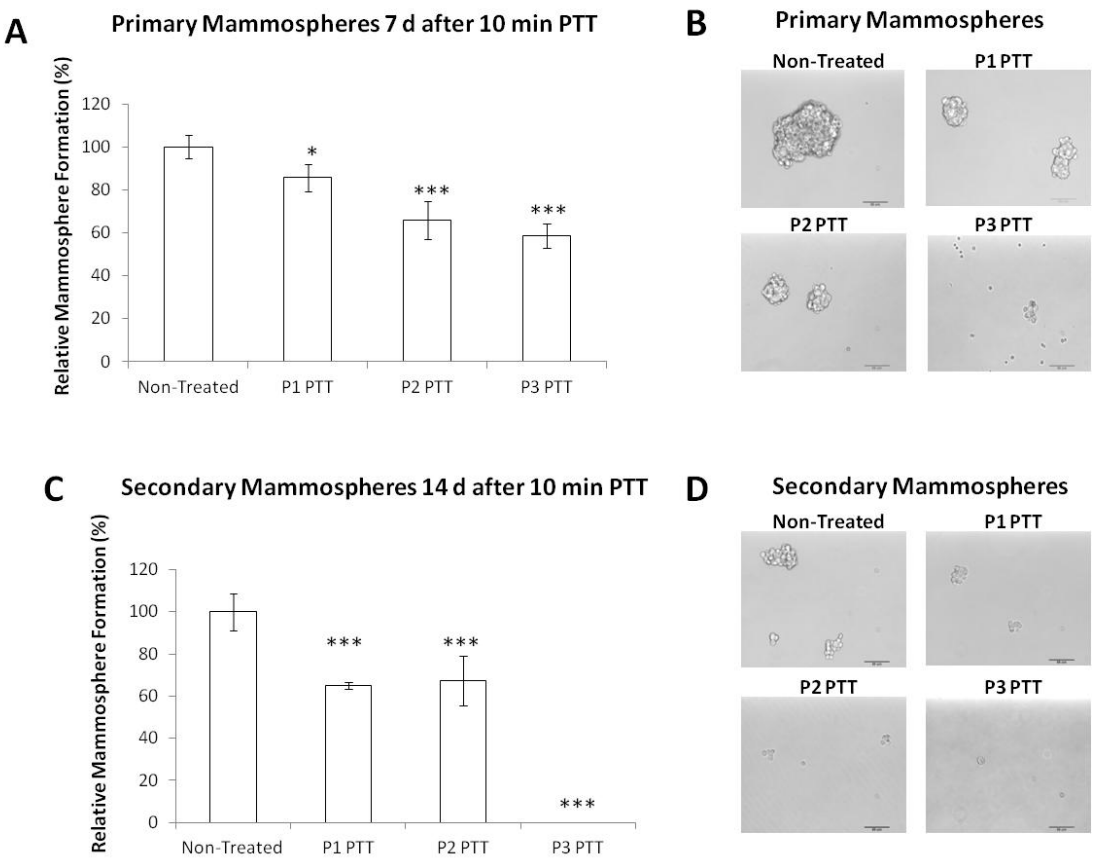

Figure 2.3. (A) MCF7 primary mammosphere formation seven days after PTT (10 min) at P1, P2, P3 laser powers, grown at a density of 6,000 cells/well. (B) Representative images of primary mammosphere size seven days after PTT. (C) Secondary mammosphere formation 14 days after primary PTT, normalized by number of cells plated per well. (D) Representative images of secondary mammosphere size 14 days after primary PTT. Primary spheres were collected on Day 7, digested to single cells and plated for secondary mammosphere formation. * $p< 0.05$, ** $p < 0.01$, *** $p < 0.001$ via Dunnett's post-hoc comparison to Non-Treated control.

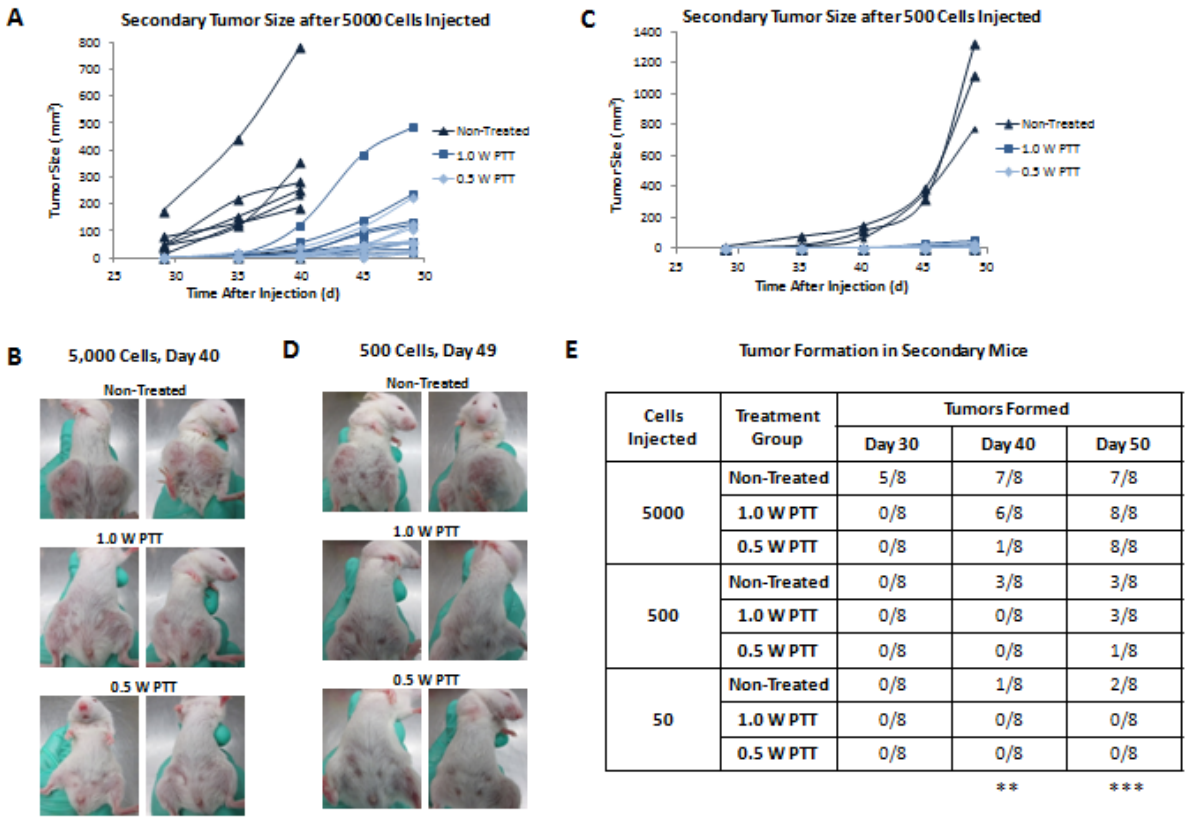

Cells Injected	Treatment Group	Tumors Formed		
		Day 30	Day 40	Day 50
5000	Non-Treated	5/8	7/8	7/8
	1.0 W PTT	0/8	6/8	8/8
	0.5 W PTT	0/8	1/8	8/8
500	Non-Treated	0/8	3/8	3/8
	1.0 W PTT	0/8	0/8	3/8
	0.5 W PTT	0/8	0/8	1/8
50	Non-Treated	0/8	1/8	2/8
	1.0 W PTT	0/8	0/8	0/8
	0.5 W PTT	0/8	0/8	0/8
			**	***

Figure 2.4. Tumor growth curves for secondary mice receiving dual injections of 5,000 (A) and 500 (C) treated SUM159 tumor cells from primary mice. Representative images of secondary mice at Day 40 after receiving 5,000 treated cells (B) and at Day 49 after receiving 500 treated cells (D). (E) Tumor formation in secondary mice after receiving injections of 5,000, 500, or 50 treated SUM159 tumor cells from primary mice. Primary mice were administered HCIONPs (20 mg Fe/kg body weight) intravenously 48 h prior to laser application. * $p < 0.05$, ** $p < 0.01$, *** $p < 0.001$ via Extreme Limiting Dilution Analysis software as described by Hu and Smith [18, 51].

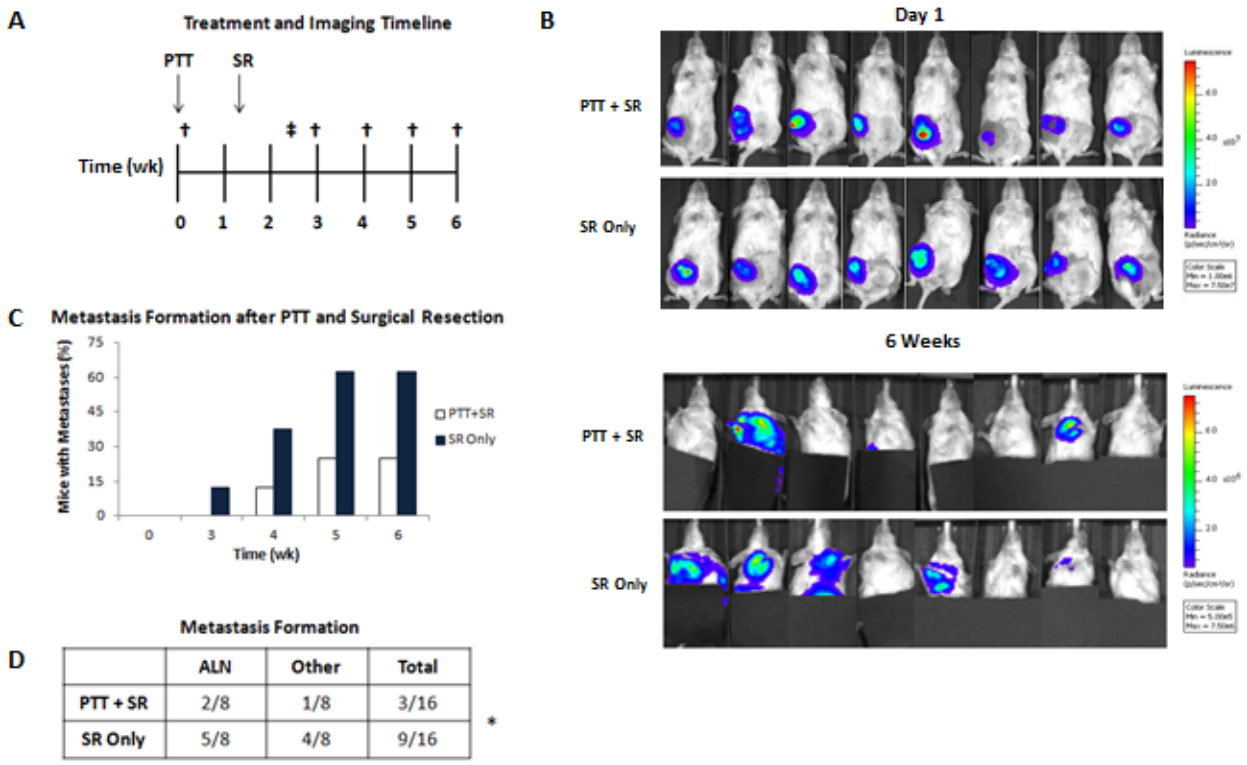

Figure 2.5. (A) Schematic of bioluminescence imaging of SUM159 tumor-bearing mice, relative to treatment. † denotes bioluminescence imaging. ‡ denotes removal of surgical wound clips. (B) IVIS bioluminescence images of mice one day and six weeks following PTT on Day 0. To image metastases with higher sensitivity, the lower portions of all mice were covered to mask the tumor signal. (C) Percentage of mice with metastasis detectable via bioluminescence imaging over time after treatment. (D) Summary of axillary lymph node (ALN) and other metastases detected in treated mice during necropsy. * $p < 0.05$ by Chi-square test of proportions.

2.8 Supplemental Figures

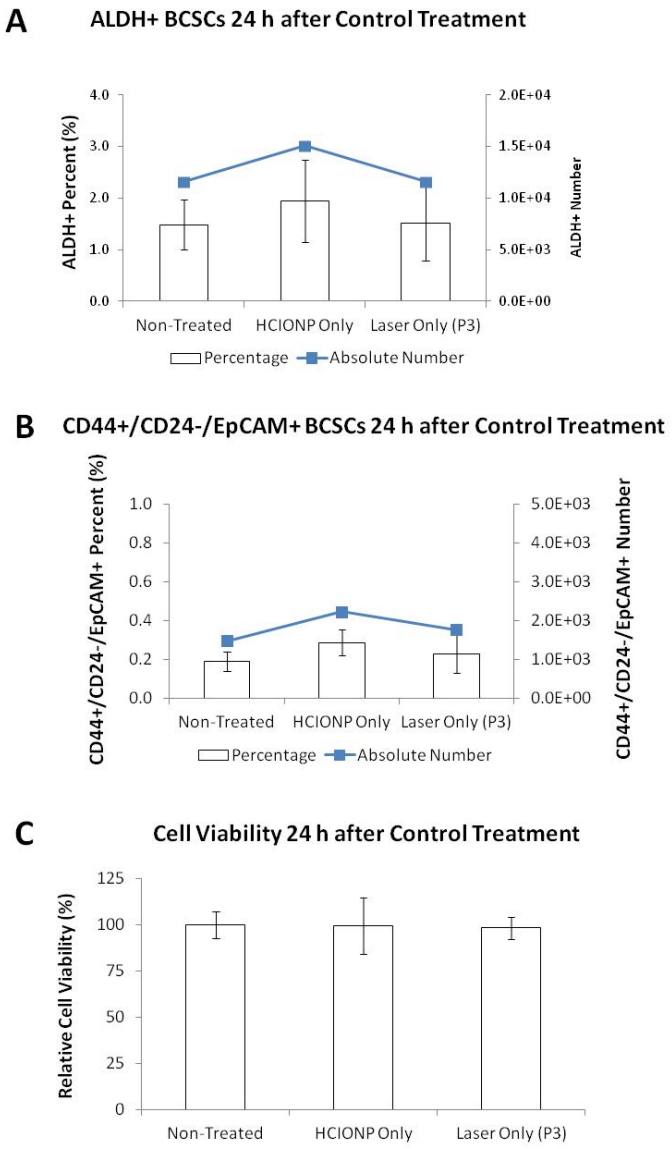

Figure 2.S1. (A) SUM159 cell viability after overnight recovery from IONP Only and Laser Only (P3 power, 10 min) control treatments. (B) MET-like ALDH+ BCSC percentage and absolute number after control treatments. (C) EMT-like CD44+/CD24-/EpCAM+ BCSC percentage and absolute number after control treatments.

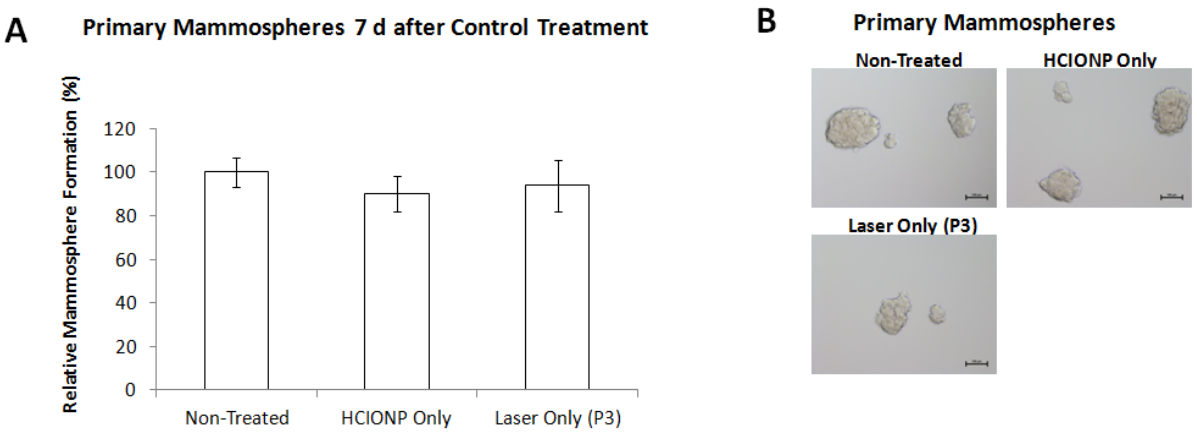

Figure 2.S2. (A) MCF7 primary mammosphere formation seven days after IONP Only and Laser Only (P3 power, 10 min) control treatment. (B) Representative images of primary mammosphere size seven days after control treatment.

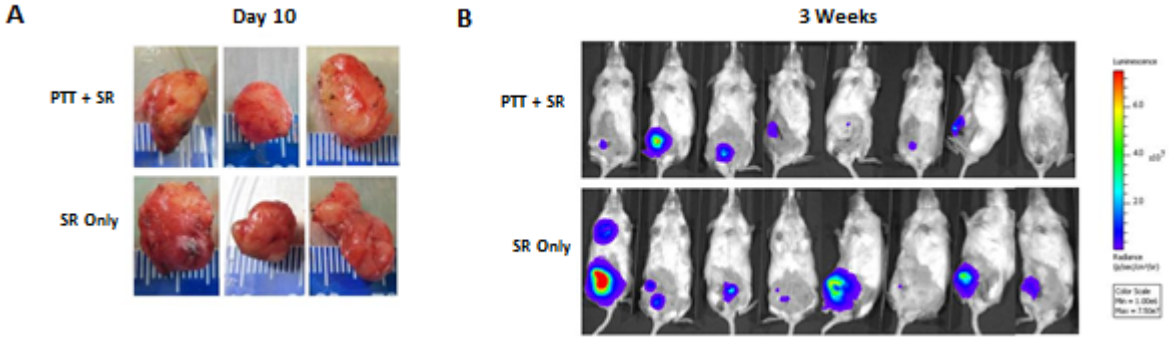

Figure 2.S3. (A) Representative images of tumors excised by surgery from treated mice on Day 10. (B) Bioluminescence images of treated SUM159 tumor-bearing mice taken at Week 3, eleven days after surgery.

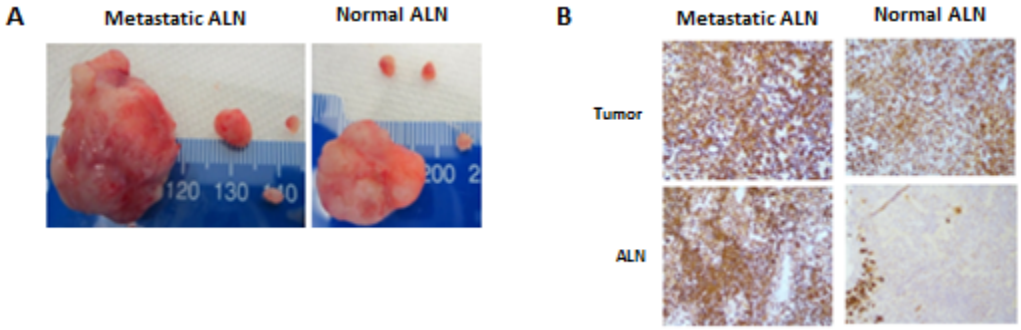

Figure 2.S4. (A) Representative images of treated tumors with normal or metastatic lymph nodes from Week 6 necropsy. (B) Representative images of pan-cytokeratin (AE-1/AE-3) staining of human metastatic cancer cells (in brown) located within tumors and lymph nodes from Week 6 necropsy of treated mice (corresponding to Figure 2.S4A) bearing SUM159 tumors.

2.9 Acknowledgements

Others who contributed to this work include Nicholas O. Stevers[1] , Joseph P. Burnett[1], Hongwei Chen[1], Miao He[1], Hasan Korkaya[2], Sean P. McDermott[3], Yadwinder Deol[3], Shawn G. Clouthier[3], Tahra Luther[3], Max S. Wicha[3], and Duxin Sun[1]. We would like to thank the operators at the University of Michigan Flow Cytometry Core, particularly Aaron Robida and Mike Pihalja, and Alan Burgess at the University of Michigan Comprehensive Cancer Center Tissue Core. This work was supported in part by the NIH Pharmacological Sciences Training Program (H.P.), the American Foundation for Pharmaceutical Education Pre-Doctoral Fellowship (H.P.), and the University of Michigan Rackham Pre-Doctoral Fellowship (H.P.).

[1]Department of Pharmaceutical Sciences, College of Pharmacy, University of Michigan, Ann Arbor, Michigan.

[2] Comprehensive Cancer Center, Department of Internal Medicine, University of Michigan, Ann Arbor, Michigan. Georgia Regents University Cancer Center, Augusta, Georgia.

[3]Department of Internal Medicine, Comprehensive Cancer Center, University of Michigan, Ann Arbor, Michigan.

2.10 References

1. Bonnet, D. and J.E. Dick, *Human acute myeloid leukemia is organized as a hierarchy that originates from a primitive hematopoietic cell.* Nat Med, 1997. **3**(7): p. 730-7.

2. Al-Hajj, M., et al., *Prospective identification of tumorigenic breast cancer cells.* Proc Natl Acad Sci U S A, 2003. **100**(7): p. 3983-8.

3. Singh, S.K., et al., *Identification of a cancer stem cell in human brain tumors.* Cancer Res, 2003. **63**(18): p. 5821-8.

4. Collins, A.T., et al., *Prospective identification of tumorigenic prostate cancer stem cells.* Cancer Res, 2005. **65**(23): p. 10946-51.

5. Li, C., et al., *Identification of pancreatic cancer stem cells.* Cancer Res, 2007. **67**(3): p. 1030-7.

6. Prince, M.E., et al., *Identification of a subpopulation of cells with cancer stem cell properties in head and neck squamous cell carcinoma.* Proc Natl Acad Sci U S A, 2007. **104**(3): p. 973-8.

7. Ginestier, C., et al., *ALDH1 is a marker of normal and malignant human mammary stem cells and a predictor of poor clinical outcome.* Cell Stem Cell, 2007. **1**(5): p. 555-67.

8. Wright, M.H., et al., *Brca1 breast tumors contain distinct CD44+/CD24- and CD133+ cells with cancer stem cell characteristics.* Breast Cancer Res, 2008. **10**(1): p. R10.

9. Korkaya, H., et al., *Activation of an IL6 inflammatory loop mediates trastuzumab resistance in HER2+ breast cancer by expanding the cancer stem cell population.* Mol Cell, 2012. **47**(4): p. 570-84.

10. Mani, S.A., et al., *The epithelial-mesenchymal transition generates cells with properties of stem cells.* Cell, 2008. **133**(4): p. 704-15.

11. Charafe-Jauffret, E., et al., *Breast cancer cell lines contain functional cancer stem cells with metastatic capacity and a distinct molecular signature.* Cancer Res, 2009. **69**(4): p. 1302-13.

12. Liu, S., et al., *Breast cancer stem cells transition between epithelial and mesenchymal states reflective of their normal counterparts.* Stem Cell Reports, 2014. **2**(1): p. 78-91.

13. Korkaya, H. and M.S. Wicha, *Selective targeting of cancer stem cells: a new concept in cancer therapeutics.* BioDrugs, 2007. **21**(5): p. 299-310.

14. Korde, L.A. and J.R. Gralow, *Can We Predict Who's at Risk for Developing Bone Metastases in Breast Cancer?* Journal of Clinical Oncology, 2011. **29**(27): p. 3600-3604.

15. Lu, J., et al., *Breast cancer metastasis: challenges and opportunities.* Cancer Res, 2009. **69**(12): p. 4951-3.

16. Weigelt, B., J.L. Peterse, and L.J. van't Veer, *Breast cancer metastasis: Markers and models.* Nature Reviews Cancer, 2005. **5**(8): p. 591-602.

17. Conley, S.J., et al., *Antiangiogenic agents increase breast cancer stem cells via the generation of tumor hypoxia.* Proc Natl Acad Sci U S A, 2012. **109**(8): p. 2784-9.

18. Atkinson, R.L., et al., *Thermal enhancement with optically activated gold nanoshells sensitizes breast cancer stem cells to radiation therapy.* Sci Transl Med, 2010. **2**(55): p. 55ra79.

19. Phillips, T.M., W.H. McBride, and F. Pajonk, *The response of CD24(-/low)/CD44+ breast cancer-initiating cells to radiation.* J Natl Cancer Inst, 2006. **98**(24): p. 1777-85.

20. Wang, R.B., P.S. Billone, and W.M. Mullett, *Nanomedicine in Action: An Overview of Cancer Nanomedicine on the Market and in Clinical Trials.* Journal of Nanomaterials, 2013.

21. Day, E.S., J.G. Morton, and J.L. West, *Nanoparticles for Thermal Cancer Therapy.* Journal of Biomechanical Engineering-Transactions of the Asme, 2009. **131**(7).

22. Hirsch, L.R., et al., *Nanoshell-mediated near-infrared thermal therapy of tumors under magnetic resonance guidance.* Proceedings of the National Academy of Sciences of the United States of America, 2003. **100**(23): p. 13549-13554.

23. Huang, X.H., et al., *Cancer cell imaging and photothermal therapy in the near-infrared region by using gold nanorods.* Journal of the American Chemical Society, 2006. **128**(6): p. 2115-2120.

24. Loo, C., et al., *Immunotargeted nanoshells for integrated cancer imaging and therapy.* Nano Letters, 2005. **5**(4): p. 709-711.

25. Li, J.L. and M. Gu, *Gold-Nanoparticle-Enhanced Cancer Photothermal Therapy.* Ieee Journal of Selected Topics in Quantum Electronics, 2010. **16**(4): p. 989-996.

26. Wang, C.H., et al., *Photothermolysis of glioblastoma stem-like cells targeted by carbon nanotubes conjugated with CD133 monoclonal antibody.* Nanomedicine, 2011. **7**(1): p. 69-79.

27. Hauck, T.S., et al., *Enhancing the Toxicity of Cancer Chemotherapeutics with Gold Nanorod Hyperthermia.* Advanced Materials, 2008. **20**(20): p. 3832-+.

28. Robinson, J.T., et al., *High Performance In Vivo Near-IR (> 1 mu m) Imaging and Photothermal Cancer Therapy with Carbon Nanotubes.* Nano Research, 2010. **3**(11): p. 779-793.

29. Zhou, F.F., et al., *Cancer photothermal therapy in the near-infrared region by using single-walled carbon nanotubes.* Journal of Biomedical Optics, 2009. **14**(2).

30. Huang, X.H., et al., *Determination of the minimum temperature required for selective photothermal destruction of cancer cells with the use of immunotargeted gold nanoparticles.* Photochemistry and Photobiology, 2006. **82**(2): p. 412-417.

31. Iancu, C. and L. Mocan, *Advances in cancer therapy through the use of carbon nanotube-mediated targeted hyperthermia.* International Journal of Nanomedicine, 2011. **6**: p. 1675-1684.

32. Wang, C., et al., *Immunological Responses Triggered by Photothermal Therapy with Carbon Nanotubes in Combination with Anti-CTLA-4 Therapy to Inhibit Cancer Metastasis.* Advanced Materials, 2014. **26**(48): p. 8154-8162.

33. Zhou, F.F., et al., *Mitochondria-Targeting Single-Walled Carbon Nanotubes for Cancer Photothermal Therapy.* Small, 2011. **7**(19): p. 2727-2735.

34. Guo, L., et al., *Combinatorial photothermal and immuno cancer therapy using chitosan-coated hollow copper sulfide nanoparticles.* ACS Nano, 2014. **8**(6): p. 5670-81.

35. Yallapu, M.M., et al., *Multi-functional magnetic nanoparticles for magnetic resonance imaging and cancer therapy.* Biomaterials, 2011. **32**(7): p. 1890-1905.

36. Toraya-Brown, S., et al., *Local hyperthermia treatment of tumors induces CD8(+) T cell-mediated resistance against distal and secondary tumors.* Nanomedicine, 2014. **10**(6): p. 1273-85.

37. Zhao, Q., et al., *Magnetic nanoparticle-based hyperthermia for head & neck cancer in mouse models.* Theranostics, 2012. **2**: p. 113-21.

38. Narayan, M., et al., *Trastuzumab-induced HER reprogramming in "resistant" breast carcinoma cells.* Cancer Res, 2009. **69**(6): p. 2191-4.

39. Bear, A.S., et al., *Elimination of metastatic melanoma using gold nanoshell-enabled photothermal therapy and adoptive T cell transfer.* PLoS One, 2013. **8**(7): p. e69073.

40. *Aurolase Therapy.* Nanospectra.

41. *Pilot Study of AuroLase(tm) Therapy in Refractory and/or Recurrent Tumors of the Head and Neck.* ClinicalTrials.gov.

42. *Efficacy Study of AuroLase Therapy in Subjects With Primary and/or Metastatic Lung Tumors.* ClinicalTrials.gov.

43. Burke, A.R., et al., *The resistance of breast cancer stem cells to conventional hyperthermia and their sensitivity to nanoparticle-mediated photothermal therapy.* Biomaterials, 2012. **33**(10): p. 2961-70.

44. Sadhukha, T., et al., *Effective elimination of cancer stem cells by magnetic hyperthermia.* Mol Pharm, 2013. **10**(4): p. 1432-41.

45. Chen, H.W., et al., *Highly crystallized iron oxide nanoparticles as effective and biodegradable mediators for photothermal cancer therapy.* Journal of Materials Chemistry B, 2014. **2**(7): p. 757-765.

46. Moghimi, S.M., A.C. Hunter, and J.C. Murray, *Long-circulating and target-specific nanoparticles: Theory to practice.* Pharmacological Reviews, 2001. **53**(2): p. 283-318.

47. Maeda, H., et al., *Tumor vascular permeability and the EPR effect in macromolecular therapeutics: a review.* J Control Release, 2000. **65**(1-2): p. 271-84.

48. Fillmore, C.M. and C. Kuperwasser, *Human breast cancer cell lines contain stem-like cells that self-renew, give rise to phenotypically diverse progeny and survive chemotherapy.* Breast Cancer Res, 2008. **10**(2): p. R25.

49. Li, Y., et al., *Sulforaphane, a dietary component of broccoli/broccoli sprouts, inhibits breast cancer stem cells.* Clin Cancer Res, 2010. **16**(9): p. 2580-90.

50. Kakarala, M., et al., *Targeting breast stem cells with the cancer preventive compounds curcumin and piperine.* Breast Cancer Res Treat, 2010. **122**(3): p. 777-85.

51. Hu, Y. and G.K. Smyth, *ELDA: extreme limiting dilution analysis for comparing depleted and enriched populations in stem cell and other assays.* J Immunol Methods, 2009. **347**(1-2): p. 70-8.

52. Liu, S., et al., *MicroRNA93 regulates proliferation and differentiation of normal and malignant breast stem cells.* PLoS Genet, 2012. **8**(6): p. e1002751.

53. Brigger, I., C. Dubernet, and P. Couvreur, *Nanoparticles in cancer therapy and diagnosis.* Advanced Drug Delivery Reviews, 2002. **54**(5): p. 631-651.

54. Storm, G., et al., *Surface Modification of Nanoparticles to Oppose Uptake by the Mononuclear Phagocyte System.* Advanced Drug Delivery Reviews, 1995. **17**(1): p. 31-48.

55. Dreaden, E.C., et al., *Size matters: gold nanoparticles in targeted cancer drug delivery.* Ther Deliv, 2012. **3**(4): p. 457-78.

56. Guo, S.T. and L. Huang, *Nanoparticles Escaping RES and Endosome: Challenges for siRNA Delivery for Cancer Therapy.* Journal of Nanomaterials, 2011.

57. Goel, R., et al., *Biodistribution of TNF-alpha-coated gold nanoparticles in an in vivo model system.* Nanomedicine, 2009. **4**(4): p. 401-410.

58. Liu, X.S., et al., *Minimizing nonspecific phagocytic uptake of biocompatible gold nanoparticles with mixed charged zwitterionic surface modification.* Journal of Materials Chemistry, 2012. **22**(5): p. 1916-1927.

59. Huang, H.C., K. Rege, and J.J. Heys, *Spatiotemporal temperature distribution and cancer cell death in response to extracellular hyperthermia induced by gold nanorods.* ACS Nano, 2010. **4**(5): p. 2892-900.

60. Lee, S.E., et al., *Remote optical switch for localized and selective control of gene interference.* Nano Lett, 2009. **9**(2): p. 562-70.

61. Hildebrandt, B., et al., *The cellular and molecular basis of hyperthermia.* Crit Rev Oncol Hematol, 2002. **43**(1): p. 33-56.

62. Dontu, G., et al., *In vitro propagation and transcriptional profiling of human mammary stem/progenitor cells.* Genes Dev, 2003. **17**(10): p. 1253-70.

63. Dontu, G., et al., *Role of Notch signaling in cell-fate determination of human mammary stem/progenitor cells.* Breast Cancer Res, 2004. **6**(6): p. R605-15.

64. Visvader, J.E. and G.J. Lindeman, *Cancer stem cells in solid tumours: accumulating evidence and unresolved questions.* Nature Reviews Cancer, 2008. **8**(10): p. 755-768.

65. Wong, N.K.Y., et al., *Heterogeneity of breast cancer stem cells as evidenced with Notch-dependent and Notch-independent populations.* Cancer Medicine, 2012. **1**(2): p. 105-113.

66. Nefedova, Y., et al., *Inhibition of Notch signaling induces apoptosis of myeloma cells and enhances sensitivity to chemotherapy.* Blood, 2008. **111**(4): p. 2220-9.

67. McArthur, H.L. and P.G. Morris, *Aromatase inhibitor strategies in metastatic breast cancer.* Int J Womens Health, 2010. **1**: p. 67-72.

68. Telli, M.L. and R.W. Carlson, *First-line chemotherapy for metastatic breast cancer.* Clin Breast Cancer, 2009. **9 Suppl 2**: p. S66-72.

69. Tanei, T., et al., *Association of breast cancer stem cells identified by aldehyde dehydrogenase 1 expression with resistance to sequential Paclitaxel and epirubicin-based chemotherapy for breast cancers.* Clin Cancer Res, 2009. **15**(12): p. 4234-41.

70. Chen, H.W., et al., *Reducing non-specific binding and uptake of nanoparticles and improving cell targeting with an antifouling PEO-b-P gamma MPS copolymer coating.* Biomaterials, 2010. **31**(20): p. 5397-5407.

71. Sevenich, L., et al., *Transgenic expression of human cathepsin B promotes progression and metastasis of polyoma-middle-T-induced breast cancer in mice.* Oncogene, 2011. **30**(1): p. 54-64.

CHAPTER 3: INVESTIGATIONS OF PHOTOTHERMAL AND IMMUNE CHECKPOINT BLOCKADE TO INHIBIT METASTATIC BREAST CANCER BY ELIMINATION OF CANCER STEM CELLS AND INDUCTION OF A SYSTEMIC T-CELL RESPONSE

3.1 Abstract

As increasing evidence implicates breast cancer stem cells (BCSCs) as drivers of metastasis that evade traditional therapies, it has become imperative to explore the untapped potential of nanomedicine to develop translational therapies that can be incorporated into current clinical practices to achieve significant improvements in patient survival. One of only few nanoparticle-based treatments to enter human clinical trials is photothermal therapy (PTT) to induce localized tumor hyperthermia. Here we employ highly crystallized iron oxide nanoparticle (HCIONP)-mediated PTT in a model of metastatic breast cancer to investigate the ability to inhibit BCSCs and induce an enhanced, and potentially synergistic, effect with cancer immunotherapy to trigger a systemic, cancer (stem) cell-specific immune response. In 4T1 metastatic breast cancer cells, twenty minute HCIONP-mediated PTT significantly reduces ALDH+ BCSCs *in vitro*. In BALB/c mice bearing 4T1 tumors ALDH+ BCSCs are significantly inhibited by PTT when given as monotherapy and in combination with PD-L1 antibody. Combination treatment with PTT and PD-L1 antibody reveals promising reductions in tumor

growth and formation of lung macrometastases. Increases of key inflammatory cytokines (IL-6) and immune cell-attracting chemokines (CXCL-1, CXCL-9, CXCL-10) in serum of dual-treated mice suggest the potential to enhance the population of tumor-infiltrating effector T-cells, which will be confirmed with quantitative immunophenotyping of saved tumor tissues. With additional studies we expect to conclusively demonstrate PTT conditions which, when combined with immune checkpoint blockade, effectively prevent metastasis through inhibition of BCSCs and eliminate existing metastases by triggering a systemic, cancer (stem) cell-specific immune response. Successful development of such nanomedicine to enhance efficacy of both BCSC elimination and a T-cell-driven immune response could potentially extend immunotherapy as a viable treatment option for metastatic breast cancer and drastically improve patient survival.

3.2 Introduction

Advancement to a metastatic disease is the primary cause of death in breast cancer patients, at which point treatment becomes palliative [1-3]. Up to 10% of patients have Stage IV or metastatic breast cancer at the time of diagnosis, and it is estimated that metastatic recurrence accounts for 20-30% of breast cancer cases [4]. The ability to detect, prevent, and successfully treat metastasis remains one of the greatest challenges in breast cancer therapy. Accumulating evidence points to breast cancer stem cells (BCSCs), identified as aldehyde dehydrogenase positive (ALDH+) or by the surface receptor phenotype CD44+/CD24-, as the culprit driving the spread of cancer cells from the breast [5-8]. Also shown to be responsible for tumor growth and recurrence, this subset of cells exhibits resistance to and may even be enriched by conventional breast cancer therapies such as radiation and chemotherapy [9-14]. This underscores a critical

need to develop innovative therapies that at the cellular level kill BCSCs and are effective against metastatic disease.

Therapeutic regimens exploiting advances in nanoparticle development offer a tremendous potential to enhance treatment efficacy against cancer stem cells (CSCs) and consequently inhibit metastasis-initiating cells. However, the most effective future therapies must not only act locally against all populations of cancer cells (differentiated and stem) to prevent future metastasis but also systemically against all populations of cancer cells in existing metastases. Recent findings by ourselves and reported in the literature together suggest that nanoparticle-mediated photothermal therapy (PTT) may be a prime candidate for development of cancer therapy that is effective against BCSCs and differentiated cancer cells, both locally and systemically.

In photothermal cancer therapy, near infrared (NIR) laser light is absorbed by nanoparticles that in response produce heat that is effective at killing cells. It is one of few nanoparticle-based treatments to enter clinical trials in human cancer patients [15, 16]. Hyperthermic cell death is localized to cancer tissue based on application of the laser light. In some pre-clinical models the PTT-mediating nanoparticles are injected into the tumor directly [17, 18]. The gold nanoshell formulation, AuroLase, currently in clinical trials is injected into the blood stream and accumulates in the tumor tissue through passive targeting by the enhanced permeability and retention (EPR) effect [19-21]. Although treatment is localized by requiring external activation by laser light, use of biocompatible nanoparticles composed of gold and carbon minimizes potential off-target side effects of PTT. Iron oxide-based nanoparticles have been used to induce hyperthermia triggered by an alternating magnetic field (AMF), and our lab

has recently shown that those with a highly crystallized structure produced by thermal decomposition are also capable of PTT [22].

Atkinson et al. were the first to study a translational approach to include nanoshell-based PTT with radiation therapy to enhance the efficacy against ALDH+ BCSCs [9]. In our recent studies described in Chapter 2, we examined iron oxide nanoparticle (IONP)-mediated PTT in human SUM159 triple negative (estrogen, progesterone, and Her2 receptor negative) breast cancer models. We showed PTT inhibits both epithelial-like ALDH+ and mesenchymal-like CD44+/CD24- BCSCs, and that in immune-compromised mice PTT prevents the spread of SUM159 cells to axillary lymph nodes. Other works examining the mechanism by which PTT effects tumor growth and metastasis have not focused on the role of CSCs but the immune system. In the last year multiple groups have reported initial findings that nanoparticle-mediated hyperthermia induces a systemic cancer-specific immune response in which cytotoxic T-cells are trained to recognize and inhibit distal cancer cells [17], a response that may be strengthened by coupling with immunotherapy [23, 24]. Various cancer immunotherapy approaches have already advanced to the clinic. The simplest for pre-clinical research is checkpoint inhibition using monoclonal antibodies, to suppress inhibitory signaling of cytotoxic T-cells by cancer cells [25-27]. Other clinically investigated cancer immunotherapy approaches, which may be considered for combination with PTT, are genetic engineering of T-cells to enhance specificity for tumor-associated antigens and adoptive T-cell transfer. In the latter, a patient's T-cells are first removed to culture and expand *ex vivo* and then reintroduced into the patient (with the T-cell growth factor IL-2 potentially included in either step) [28-30].

Recent findings from photothermal therapy in immune-competent mice [17, 23, 24] collectively suggest a mechanism in which PTT at the primary tumor site triggers a release of

inflammatory cytokines and chemokines, such as those seen in burn patients, that attract antigen presenting cells (APCs) such as dendritic cells (DCs) to the tumor site. This results in activated DCs in tumor draining lymph nodes that present to CD8+ cytotoxic T-cells, which are drawn to the tumor site by the released chemokines such as CXCL1. The effector T-cell response is evident by an increase of IFN-γ at the tumor site released by dying cancer cells. Furthermore, it was shown that the systemic immune effect of PTT is enhanced by combination with immunotherapy intended to boost T-cell populations. Decreased lung metastasis and increased CD8+ populations and decreased growth in contralateral tumors that did not receive PTT were improved when PTT was supplemented with either adoptive T-cell therapy or immune checkpoint inhibition via a CTLA-4 antibody [23, 24]. Wang et al also reported the unique ability of carbon nanotubes photothermal mediators to act as an adjuvant to boost maturation of DCs and production of antitumor cytokines [24].

Here we sought to expand upon our previous study to inhibit breast cancer stem cells and prevent metastasis by iron oxide nanoparticle-mediated PTT, discussed in Chapter 2, by investigating treatment conditions which in immune-competent mice would induce local hyperthermia and a systemic immune response, both effective against BCSCs. Our first objective was to examine PTT efficacy against BCSCs in immune-competent mice with 4T1 metastatic breast cancer. Furthermore, we sought to determine whether in this setting PTT combination with immunotherapy will be additive or even synergistic. Our next objectives were to investigate the ability of such treatment to trigger cytokine and chemokine release by dying cancer cells and consequently increase cytotoxic T-cells in the tumor tissue. HCIONP-mediated PTT was first studied *in vitro* in 4T1 cells, revealing successful inhibition of ALDH+ BCSCs after 20 minutes heating to 46 °C. Furthermore, ALDH+ BCSCs in BALB/c mice bearing 4T1

tumors were significantly inhibited 48 h after PTT when given as monotherapy and in combination with PD-L1 antibody. Our initial results reveal that dual treatment combining PTT and PD-L1 blockade reduces tumor growth and formation of lung macrometastases, which may be further improved with adjustments to the treatment regimen. Analysis of serum in tumor-bearing mice post-treatment reveals induction of key inflammatory cytokines (IL-6) and immune cell-attracting chemokines (CXCL-1, CXCL-9, CXCL-10). To overcome challenges with quantification of T-cells by flow cytometry of homogenized tumor tissue, sections of saved tumor tissue will be analyzed by quantitative immunophenotyping.

The preliminary data presented here lays the groundwork to establish conditions in which localized PTT mediated by biodegradable iron oxide nanoparticles can prevent metastasis through inhibition of BCSCs in the primary tumor and, in combination with cancer immunotherapy, induce an immune response effective at eliminating existing metastatic cancer cells including BCSCs. Successful development of such translational nanomedicine to extend immunotherapy to metastatic breast cancer patients, enhancing recruitment of cytotoxic T-cells which become trained to recognize and kill distal cancer (stem) cells, would have potential to significantly improve survival of a widespread and currently incurable disease.

3.3 Results and Discussion

Our lab has developed highly crystallized iron oxide nanoparticles (HCIONPs) that are efficient mediators of photothermal therapy *in vivo* [22]. In contrast to more commonly used gold-based nanoparticles for PTT, the HCIONPs are biodegradable, capable of magnetic resonance imaging (MRI) of tumors, and their small size (~15 nm) is ideal for passive tumor

accumulation by the enhanced permeation and retention (EPR) effect [22, 31-33]. As discussed in Chapter 2, we have shown that HCIONP-mediated PTT eliminates BCSCs in SUM159 triple negative breast cancer cells *in vitro* and in immune-compromised NOD/SCID mice bearing SUM159 tumors. In order to study the ability of HCIONP-mediated PTT to induce a systemic antitumor effect in our follow up work, mouse breast cancer cells would be needed to establish tumors in immune-competent mice. For this work we selected the 4T1 cell line for *in vitro* and *in vivo* studies, as it has been used as a model for stage IV metastatic triple negative breast cancer and has a quantifiable ALDH+ BCSC population [34-36].

Like with our previous study, we first sought to demonstrate the ability of PTT to eliminate ALDH+ BCSCs *in vitro* by flow cytometry. 4T1 cells were subjected to 20 min PTT (HCIONPs + Laser) in a 96-well plate. Control treatments included Laser Only and HCIONP Only. As shown in Figure 3.1A, medium containing cells exposed to HCIONPs (0.1 mg Fe/mL) prior to laser treatment (0.24 W) reached a temperature ~46.5 °C within 10 minutes, at which point the temperature had essentially plateaued (~47 °C at 20 min). In contrast, a minimal temperature increase from ~31 to ~35 °C was observed in the medium containing cells in the Laser Only treatment group. Cells were counted and bulk viability determined 24 hours following PTT, prior to quantification of each BCSC population by flow cytometry. While Laser Only and HCIONP Only control treatments did not significantly affect 4T1 cell viability, the relative viability of PTT-treated cells dropped to 26% ($p < 0.001$) of the Non-Treated control (Figure 3.1B). Live BCSCs with elevated expression of the aldehyde dehydrogenase enzyme (ALDH+) were quantified after PTT by staining with DAPI and the Aldefluor kit followed by flow cytometry. As shown in Figure 3.1C only in the PTT-treated group does the ALDH+ cell population significantly decrease ($p < 0.001$), 3-fold from ~2% in the Non-Treated control. The

treatment effect is more apparent considering the absolute BCSC number (Figure 3.1C), accounting for the dramatic decrease in overall cell survival.

Next we intended to confirm our *in vitro* results with analysis of HCIONP-mediated PTT inhibition of ALDH+ BCSCs in immune-competent BALB/c mice with orthotopic 4T1 tumors grown in the inguinal mammary fat pad. For each of our *in vivo* experiments, we sought to investigate the potential to enhance response to treatment by combining PTT with cancer immunotherapy intended to boost the efficacy of effector cytotoxic T-cells in the tumor tissue. Our rational for this was three-fold. First, as described above, recent studies have revealed that PTT-mediated cell death triggers cytokine release and a signaling cascade that attracts cytotoxic CD8+ T-cells to tumor site [17, 23, 24]. Second, PTT via HCIONPs that have greatest tumor accumulation at the periphery [37] may induce damage to vasculature at the tumor boundary to enhance T-cell tumor infiltration. Third, immunotherapy aimed to boost efficacy of cytotoxic T-cells drawn to the primary tumor by PTT may promote development of an adaptive immune response against metastatic cancer cells [23, 24]. For our studies of PTT combined with cancer immunotherapy in mice, we chose an antibody to block the interaction between the programmed death 1 (PD-1) receptor on T-cells and the programmed death ligand 1 (PD-L1) receptor on cancer cells. Ligand activation of the PD-1 immune checkpoint pathway is normally used in regulating autoimmunity. However, many cancers have adapted to express the PD-L1 ligand to inhibit T-cell function and escape attack by these cells [38]. As the 4T1 cell line has been shown to have induced expression of PD-L1 *in vivo* [39, 40], we chose an anti-PD-L1 antibody for our studies. The PTT/PD-L1 antibody treatment regimen in immune-competent BALB/c mice with orthotopic 4T1 tumors grown in the inguinal mammary fat pad is shown in Scheme 3.1. Following tumor measurement on Day 0, mice were administered PD-L1 antibody every other

day beginning on Day 1. HCIONPs were injected by tail vein on Day 1 and PTT conducted on Day 2.

For our first *in vivo* study, we sought to confirm our *in vitro* results with analysis of HCIONP-mediated PTT inhibition of ALDH+ BCSCs. Mice with 4T1 tumors (~55 mm^3) were divided into Non-Treated, PD-L1 Antibody, PTT, and PTT + PD-L1 Antibody treatment groups (n=5-6). Mice in both groups given PD-L1 antibody received intraperitoneal (IP) injections (200 μg) 24 h before and 24 h after PTT. Mice receiving PTT were administered HCIONPs by tail vein (20 mg Fe/kg body weight) 24 h before 20 min laser application at a power of 0.52 W. As shown in Figure 3.2A, this resulted in a rapid increase in tumor surface temperature to ~55 °C within five minutes. Mice were sacrificed 48 h after PTT and tumors were digested for Aldefluor staining of single cells. Analysis by flow cytometry in Figure 3.2B reveals an average population of ALDH+ cells in the Non-Treated group of ~1.6%, consistent with our *in vitro* results. As expected, PTT significantly decreased the ALDH+ cells 3-fold to ~0.5% ($p < 0.001$). Similar results were obtained with the dual PTT + PD-L1 Antibody group ($p < 0.001$), while the ALDH+ population in the PD-L1 Antibody group was comparable to the Non-Treated control. While this suggests that PTT is the main inhibitor of ALDH+ BCSCs, recent efforts to develop CSC vaccines specifically targeting ALDH+ BCSCs [41-43] indicate that the death of these cells at the tumor site may result in BCSC inhibition by T-cells at distal sites; we expect this effect would be bolstered by PD-L1 antibody immunotherapy to boost the activity of cytotoxic T-cells at the primary tumor site following PTT.

The primary factors to determine efficacy of HCIONP-mediated PTT and anti-PD-L1 antibody treatments alone and in combination were tumor growth and development of lung macrometastases. 4T1 cells are syngeneic in BALB/c mice and spontaneously metastasize to the

lungs, which is the major cause of death, and other organs [44, 45]. Mice with tumors ≤ 80 mm^3 were randomized into treatment groups (n=5-6) on Day 0 and treated as shown in Scheme 3.1. Tumors were measured every five days following PTT on Day 2, and twenty days later mice were sacrificed. As shown in Figure 3.3A, PTT and PTT + PD-L1 Ab groups have modest but not significant reductions in tumor size compared to the Non-Treated control mice; tumor sizes in mice treated only with the anti-PD-L1 antibody were similar to control. While not quite significant compared to the Non-Treated control, mice in the dual-treatment group had the least development of lung metastases as shown in Figure 3.3B. Mice receiving the anti-PD-L1 antibody alone had the next greatest reduction in observable lung metastases. Photos of the excised lungs (Figure 3.3C) and representative hematoxylin and eosin (H&E) slides of lung sections confirm these observable differences (Figure 3.3D). On average the mice in PTT + PD-L1 Ab treatment group also had slightly smaller lung masses (data not shown), potentially an effect of having fewer metastatic growths. While the combination of HCIONP-mediated hyperthermia and anti-PD-L1 antibody immunotherapy appear to have the greatest ability to reduce 4T1 tumor growth and lung metastases, it is clear the therapeutic regimen must be altered to achieve statistically significant results. For example, like the anti-PD-L1 antibody administered multiple times over several days, multiple laser applications following HCIONP administration could help eliminate residual cancer cells after one PTT session.

To study whether PTT and PD-L1 inhibition can induce a substantial immune response driven by activation of CD8+ cytotoxic T-cells as described above [17, 23, 24], mice were treated according to Scheme 3.1 and were sacrificed on Days 4 and 10 to analyze serum cytokine and chemokine concentrations as well as tumor T-cell populations. While the majority of the 22 cytokines and chemokines tested were not significantly affected by the conditions of treatment,

our data revealed significant increases in four promising molecules: IL-6, CXCL-1, CXCL-9 and CXCL-10. A proinflammatory cytokine and typical marker of cellular immunity mediated through CD8+ T-cells, IL-6 was reported to be elevated in mouse serum following PTT induced by carbon nanotubes (subcutaneously injected) and hollow gold nanoshells (intratumorally injected) [23, 24]. The chemoattractant CXCL-1, known to draw neutrophils to burned tissues, was also higher in serum following PTT, as previously reported [23]. The chemoattractants CXCL-9 and CXCL-10 are recruiters of CD8+ T-cells and are directly correlated with the number of effector CD8+ T-cells that infiltrate tumors [46, 47]. As shown in Figure 3.4 (A-D), on Day 10 IL-6 and the three CXCL chemokines are elevated in serum following PTT + PD-L1 Antibody treatment compared to serum in Non-Treated mice. Surprisingly, the initial results in the mice receiving monotherapy suggest that PD-L1 Antibody treatment may have had a greater effect than PTT. These results may too have been influenced by the much longer duration of PD-L1 Antibody treatment compared to PTT, but follow up studies will need to be conducted to confirm these initial findings and make definitive conclusions.

In addition to serum collection for cytokine/chemokine analysis on Days 4 and 10, tumors were harvested and digested for flow cytometry analysis of CD8+ cytotoxic T-cells, CD4+ helper T-cells, and CD4+/FoxP3+ regulatory T-cells. CD4+ T-helper cells release IL-2 to promote CD8+ T-cell function and viability [48]. Regulatory T-cells, which are also characterized by high CD25 expression, normally function to help to maintain self-tolerance by inhibition of effector T-cell responses; one way this is accomplished is competition with CD8+ T-cells for IL-2 [30, 49, 50]. Immunotherapy efficacy is correlated with the ratio of CD8+ effector T-cells to regulatory T-cells [23, 30, 51]. Unfortunately, it was difficult to make conclusions from our flow data due to issues likely caused by high non-specific antibody

staining. It is possible that our observations may have been affected by staining the samples for concurrent ALDH analysis. Incubating the samples with Aldefluor reagent and the T-cell-binding antibodies at 37 °C in Aldefluor buffer, which contains efflux pump inhibitors, may have altered T-cell receptor expression and increased non-specific antibody binding [52]. While this approach has been previously used by our lab and others for concurrent ALDH and CD44/CD24 receptor expression analysis, for T-cell analysis in future studies it would be better incubate samples on ice in standard buffer (e.g., Hanks' balanced salt solution (HBSS) + 2% FBS) [53]. For our current analysis, we saved sections of each tumor sample before digestion and preserved them by formalin fixation and embedding in paraffin (FFPE). Thus as an alternate to T-cell analysis of homogenized samples by flow cytometry, we can perform quantitative immunophenotyping with multispectral imaging of the FFPE samples following multicolor immunofluorescence staining [54-56]. Besides eliminating the time-sensitivity and viability challenges presented by flow cytometry, this quantitative immunophenotyping approach allows for spatial analysis of cell type within preserved tissues that is not possible with flow cytometry analysis of homogenized samples. Repeating the analysis of our tumor tissue with this approach will give us a better picture of the cellular immune response triggered by our current conditions for PTT and PD-L1 immunotherapy, and will serve as a reference point to enhance future treatment regimens (e.g., further increase the population of CD8+ tumor-infiltrating effector T-cells).

There are many observations from our current data to consider to enhance the efficacy of PTT and immune checkpoint inhibition in metastatic cancer. Our most conclusive results were significant inhibition of the ALDH+ BCSCs in orthotopic 4T1 mammary tumors. Our initial data revealing inhibition of tumor growth and formation of lung metastasis in dual-treated mice

receiving PTT and immunotherapy are promising, but demonstrate that the therapeutic regimen and possibly other factors will need to be adjusted to achieve significant results. Two observations highlight the significant potential to improve treatment efficacy by performing multiple applications of PTT (e.g., 24 h and 48 h after the HCIONP injection, and possibly following additional injections). Our initial findings suggest that metastasis development may be better correlated with PD-L1 Ab treatment than PTT, which may be a consequence of multiple antibody treatments given through Day 9 whereas PTT was performed only once on Day 2. Furthermore, ALDH BCSC analysis on Day 10 revealed that the initial drop in the ALDH+ population observed at Day 4 begins to recover (data not shown), which may explain why tumor growth was reduced following PTT compared to Non-Treated mice but not significantly. Alternately, hyperthermic cell death by PTT of the primary tumor may be improved by intratumoral injection of HCIONPs, as reported in the literature [17, 18], to increase the nanoparticle concentration and distribution throughout the tumor tissue. This may also prevent any added burden to the immune system following intravenous HCIONP injection, as the immune system begins to recognize the foreign material and attempt to eliminate it through organs of the reticuloendothelial system (RES) or mononuclear phagocyte system (MPS) [57-59].

Several factors play a role in the efficacy of T-cell focused immunotherapies. Inherent tumor immunogenicity, particularly the population of cytotoxic T-cells present in the tumor, is correlated with patient outcome following therapy [60, 61]. Mouse 4T1 breast cancer cells have been shown to have low PD-L1 expression *in vitro*, but it is induced when grown *in vivo* due to IFN-γ signaling [39, 40]. While several papers have used a 4T1 mouse model to study immune checkpoint inhibition, others have reported it to be a poorly immunogenic model and have

encountered issues dealing with myeloid-derived suppressor cells (MDSCs) [62, 63]. Stemming from a variety of cells of myloid origin, MDSCs exist predominantly in bone marrow in a non-inflammatory state; in cancer or other inflammatory states, secretion of cytokines and other soluble factors trigger immune-suppressive activity of MDSCs at the tumor. The role of these "natural suppressor cells" in immune suppression is multi-faceted. Literature investigating how MDSCs suppress T-cells has primarily focused on their effects on T-cell priming [64]. It has also been shown that they may indirectly inhibit activity of effector CD8+ and CD4+ T-cells by inducing regulatory T-cells [64, 65]. In BALB/c mice bearing 4T1 tumors, Kim et al. showed that treatment with both anti-CTLA-4 and anti-PD-1 antibodies was insufficient to eradicate tumor growth and sustain survival. However, addition of MDSC inhibitors resulted in complete regression of primary tumors and increased overall survival from 30% to 80% at 100 days post-tumor implantation [62]. When Bear et al. first investigated nanoparticle-mediated PTT in mice bearing poorly immunogenic B16-F10 tumors they found that PTT needed to be coupled with ACT to overcome MDSC activity. Especially considering that CXCL-1 production has been reported to attract MDSCs to breast cancer tumors [66], our therapeutic efficacy may benefit from studies conducted to better understand how MDSCs respond to PTT and immunotherapy and whether they play a significant role in the immune response to treatment. Aside from potential changes in the therapeutic regimen, such as multiple applications of PTT, we may consider use of an alternative antibody to the anti-PD-L1 for continued work with 4T1 cells. For instance, an anti-CTLA-4 antibody to boost T-cells in the priming phase may be more efficacious.

The 4T1 breast cancer model has several advantages for our studies: it spontaneously metastasizes and is a great model for human stage IV breast cancer, it is syngeneic with BALB/c

mice and thus enables the study of the immune response to treatment, and has a quantifiable ALDH+ BCSC population [34-36]. However, little research has been performed to evaluate CD44+/CD24- as a marker for 4T1 (mesenchymal-like) BCSCs [67-70]. One group reported isolating CD24+/CD44+/ALDH+ tumor-initiating 4T1 cells [67], and another group found enhanced tumorigenic capabilities of CD24-/CD44+ 4T1 cells versus CD24+/CD44+ cells or a mixture of these two populations when injected into BALB/c mammary fat pads [68]. The ability to build off of our previous work by analyzing the effect of PTT on both ALDH+ epithelial-like BCSCs and CD44+/CD24- mesenchymal-like BCSCs would be ideal for future studies. While the two BCSC populations may plastically transition from one to the other, recent findings suggest that ALDH+ BCSCs may be the dominate driver of tumor growth and CD44+/CD24- BCSCs may more directly mediate metastasis [5].

The preliminary data presented here will serve to guide future studies of combination PTT and immunotherapy aimed to enhance inhibition of tumor growth and metastasis formation, and to initiate a CD8+ T-cell driven immune response that involves development of memory T-cells that will recognize breast cancer cell and BCSC antigens for sustained protection against recurrence and metastasis. Our immediate objectives will be to repeat studies of tumor growth, development of lung macrometastases, serum cytokine and chemokine induction, and changes in tumor T-cell populations. We also plan to conduct *in vitro* and *in vivo* experiments to investigate the ability of PTT to trigger activation of CD8+ T-cells that, upon exposure to dying cells in the primary tumor, become trained to recognize and kill BCSCs. Ideally we expect to unveil conditions for which PTT, as shown recently with ionizing irradiation [71], has an additive or synergistic effect when coupled with cancer immunotherapy, and to demonstrate the potential for

clinical translation of such combination therapy to significantly improve responses in patients with metastatic disease.

3.4 Conclusions

Here we sought to inhibit breast cancer stem cells and prevent metastasis in immune-competent mice by photothermal therapy using highly crystallized iron oxide nanoparticles, and conduct initial studies of the ability to induce a (BCSC-specific) systemic immune response when used in conjunction with immunotherapy. HCIONP-mediated PTT of BCSCs was first studied *in vitro* in 4T1 metastatic breast cancer cells, revealing successful inhibition of ALDH+ BCSCs after 20 minutes heating to 46 °C. Furthermore, ALDH+ BCSCs in BALB/c mice bearing 4T1 tumors were significantly inhibited 48 h after PTT when given as monotherapy and in combination with PD-L1 antibody. Combination treatment with PTT and PD-L1 antibody reduces tumor growth and formation of lung macrometastases but may be improved through adjustments to the treatment regimen. Analysis of serum in tumor-bearing mice post-treatment reveals induction of key inflammatory cytokines (IL-6) and immune cell-attracting chemokines (CXCL-1, CXCL-9, CXCL-10). Challenges encountered with quantification of T-cells by flow cytometry of homogenized tumor tissue necessitate follow up analysis of sections of tumor tissue saved for quantitative immunophenotyping. The preliminary data summarized here lays a foundation for continued experiments to demonstrate conditions in which localized PTT mediated by biodegradable iron oxide nanoparticles can: prevent metastasis through inhibition of BCSCs in the primary tumor, and induce a T-cell driven immune response effective at eliminating existing metastatic cancer cells, including BCSCs, when stimulated by immune

checkpoint blockade. Clinical translation of this nanomedicine approach to enhance cancer immunotherapy could lead to a viable treatment option for cancers in which patients don't currently respond to immunotherapy alone, potentially improving survival of patients with currently incurable metastatic breast cancer.

3.5 Materials and Methods

Preparation of HCIONPs: Polymer-coated HCIONPs were prepared as discussed in Chapter 2. Briefly, HCIONPs (15 nm diameter) were synthesized in organic solvent by thermal decomposition [22] and coated with diblock copolymer poly(ethylene oxide)-b-poly(γ-methacryloxypropyl trimethoxysilane) (PEO-b- PγMPS) synthesized by reversible addition fragmentation chain transfer (RAFT) polymerization [72]. Following purification by a magnetic separator (Frantz laboratory), the iron concentration was determined using o-phenanthroline as previously described [22]. HCIONPs were diluted in phosphate buffered saline (PBS) for *in vitro* and *in vivo* studies.

HCIONP-mediated PTT in vitro: 4T1 murine breast cancer cells were grown at 37 °C with 5% CO_2 as adherent monolayers in RPMI-1640 medium supplemented with 10% fetal bovine serum and 1% antibiotic-antimycotic. For PTT, a 96-well plate containing 4T1 cells (500,000/well) suspended in cell culture medium was rested on a hot plate set to 37 °C. HCIONPs were added at a final concentration of 0.1 mg Fe/mL in 200 μL per well. The solution was heated by a NIR laser (885 nm, spot size 5x8 mm^2, MDL-III-885, OPTO Engine LLC, Midvale, UT) at a power of 0.24 W for 20 minutes. The temperature was recorded each minute

using an infrared camera (FLIR Systems, i7, Boston, MA). After PTT the cells were collected, added to 25 cm^2 flasks, and allowed to recover overnight.

Mouse Models for PTT: All mouse studies were conducted in accordance with a standard animal protocol approved by the University of Michigan University Committee on the Use and Care of Animals. Five week old BALB/c immune-competent mice were obtained from Harlan laboratories. Primary xenograft tumors were formed in the no 4 inguinal mammary pad by orthotopic injection of $0.5x10^4$ 4T1 cells suspended in matrigel. Upon the detection of palpable tumors, tumor volumes were calculated according to the following equation: volume = 0.5 x length x $(width)^2$. For all *in vivo* studies mice were intravenously injected with HCIONPs by tail vein (20 mg Fe per kg mouse body weight) and, following anesthesia, 24 h later the NIR laser (0.52 W) was applied for 20 min. Tumor surface temperatures were continuously monitored using an infrared camera (FLIR Systems, i7, Boston, MA).

Flow Cytometry: For analysis 24 h after *in vitro* PTT, 4T1 cells were collected and counted using Trypan Blue before staining. The Aldefluor Assay (StemCell Technologies, Durham, NC) was conducted according to the manufacturer's instructions. DAPI was used for cell viability. Samples were run on a FACSCanto II (BD) to collect 10,000 live cells. For analysis of *in vivo* PTT, mice were humanely euthanized two or eight days after PTT (Day 4, Day 10). 4T1 tumors were harvested and digested using a gentleMACS Octo Dissociator (MACS Miltenyi Biotec, San Diego, CA) according to the manufacturer's protocol. Cells were stained with Aldefluor reagent, CD3-BV711, CD8-PE-Cy7, CD4-APC, FoxP3-PE antibodies (BioLegend) and DAPI for 30 min at 37 °C in Aldefluor reagent. Samples were run on a FACSAria III (BD) to collect 10,000 live cells. Analysis was conducted using Flowing Software

2.5.1 (Perttu Terho, Turko Centre for Biotechnology, University of Turko, Finland) and FACSDiva Software (BD).

Metastasis Studies: Following PTT, tumors were measured every five days. Twenty days post-PTT, mice in each treatment group were sacrificed based on tumor burden. Lungs were removed and their mass recorded, and macrometastases were counted. Lungs and tumors were formalin fixed and paraffin embedded (FFPE). Sections of lung tissue were imaged using an inverted microscope (Nikon Eclipse Ti-E) following hematoxylin and eosin (H&E) staining to detect micro- and macrometastases.

Cytokine Analysis: Two or eight days following PTT, mice were sacrificed and blood collected via cardiac puncture. Serum was obtained through centrifugation using Microtainer tubes (BD) at 1500 g for 10 minutes. Cytokine and chemokine concentrations were measured in duplicate using a Milliplex Mouse Premixed 22-plex assay (Millipore) and a Luminex^{200} System.

Statistical Analysis: All data are represented as mean ± standard deviation. The significance values of data sets with more than two groups were calculated using Minitab software via one-way analysis of variance (ANOVA) followed by either Dunnett's post-hoc comparisons to the non-treated control or Tukey's post-hoc testing as indicated.. A $p < 0.05$ was considered statistically significant.

3.6 Figures

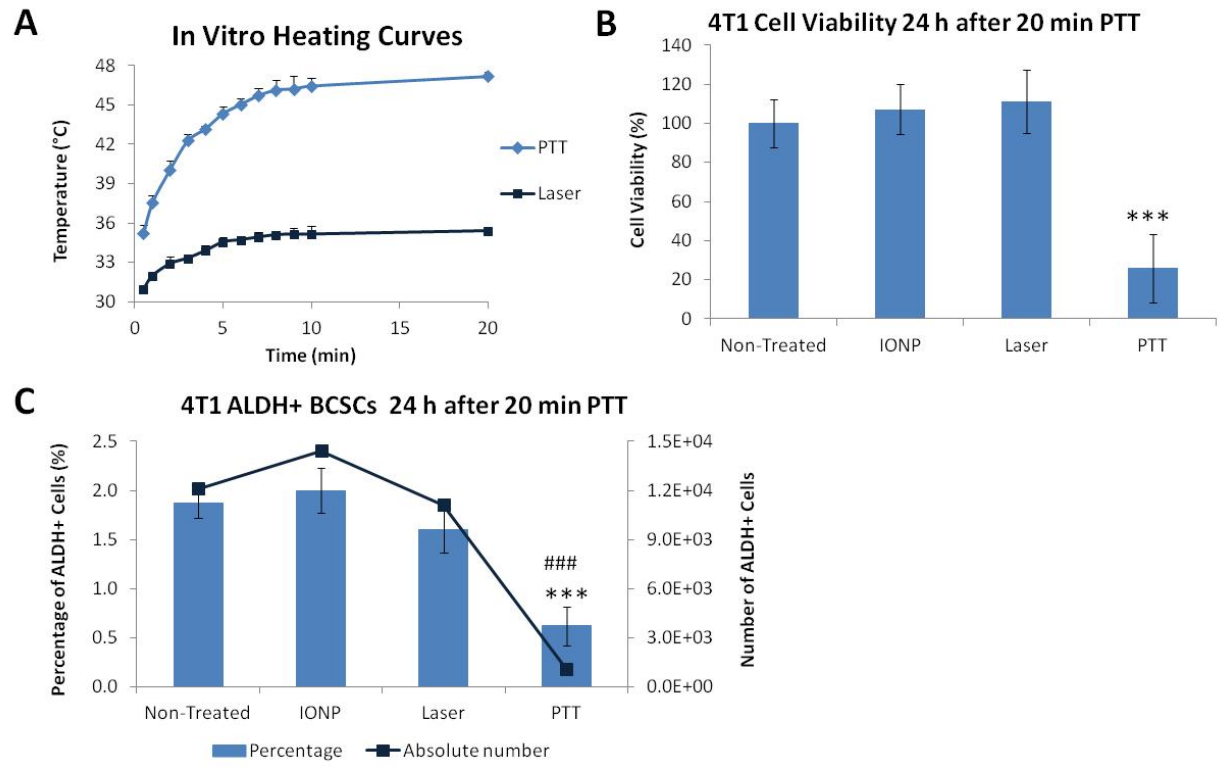

Figure 3.1. (A) Heating curves of 4T1 cells receiving Laser Only or PTT (HCIONPs 0.1 mg Fe/mL) treatments on a 96-well plate. (B) 4T1 cell viability 24 h after 20 min PTT. (C) ALDH+ BCSC percentage and absolute number 24 h after 20 min PTT. For cell viabilities and percentages of BCSCs, * $p < 0.05$, ** $p < 0.01$, *** $p < 0.001$ via Dunnett's post-hoc comparison to Non-Treated control. For absolute numbers of BCSCs, # $p < 0.05$, ## $p < 0.01$, ### $p < 0.001$ via Dunnett's post-hoc comparison to Non-Treated control.

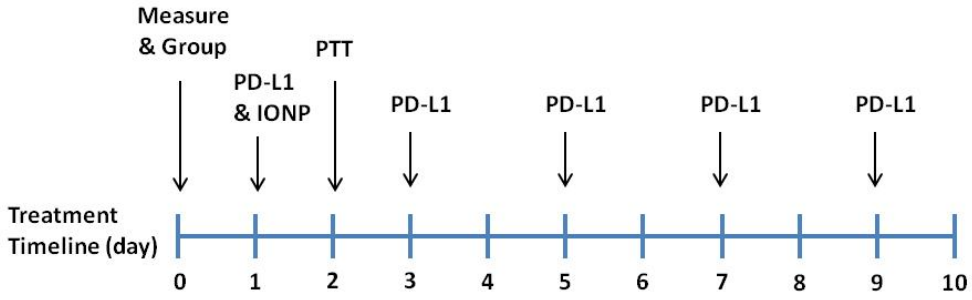

Scheme 3.1. For *in vivo* studies, BALB/c mice bearing orthotopic 4T1 mammary tumors were divided into treatment groups based on tumor size on Day 0. Mice were injected with HCIONPs (intravenously) and PD-L1 antibody (intraperitoneally) on Day 1. PTT occurred on Day 2, allowing 24 hours for HCIONP intratumoral accumulation. PD-L1 antibody was administered every other day a total of five times, ceasing on Day 9.

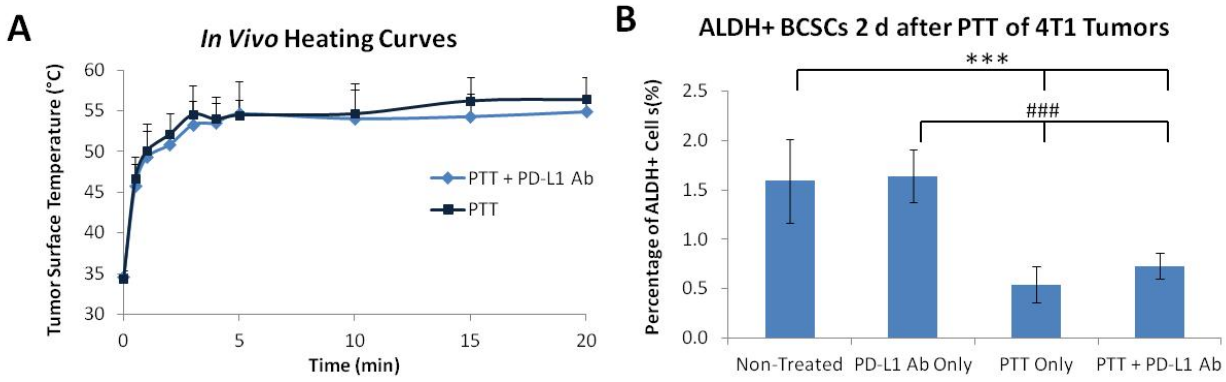

Figure 3.2. (A) Heating curves of 4T1 mammary fat pad tumors in BALB/c mice receiving PTT or PTT + PD-L1 Antibody treatments. (B) ALDH+ BCSC percentage 2 d after 20 min PTT. * $p < 0.05$, ** $p < 0.01$, *** $p < 0.001$ via Tukey's post-hoc comparison to Non-Treated control. # $p < 0.05$, ## $p < 0.01$, ### $p < 0.001$ via Tukey's post-hoc comparison to PD-L1 Ab treatment.

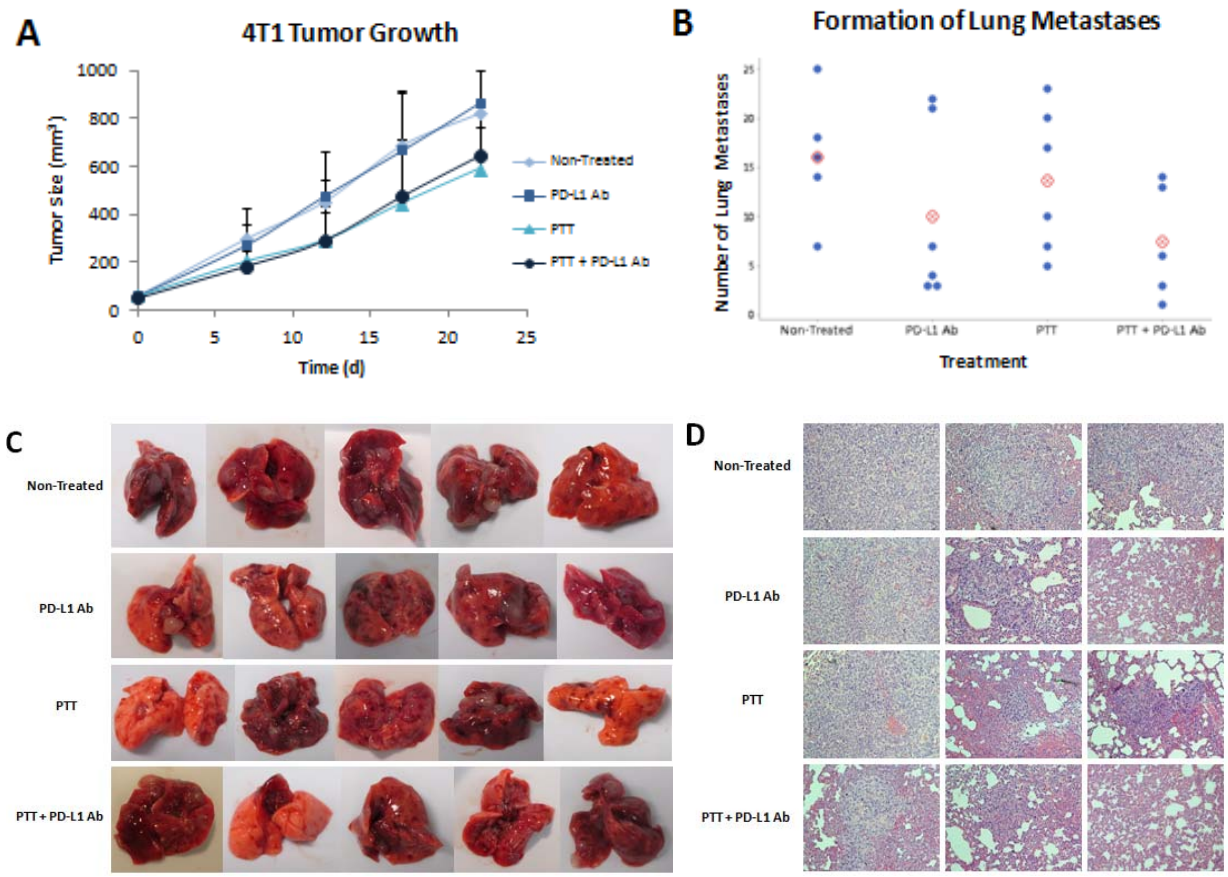

Figure 3.3. (A) 4T1 tumor growth in BALB/c mice following photothermal and immunotherapy treatments. (B) Number of lung metastases in individual mice, counted in tissue harvested on Day 22. Averages per treatment group are shown in red. (C) Photos of excised lungs after sacrificing mice on Day 22. (D) Representative H&E staining of sectioned lung tissue.

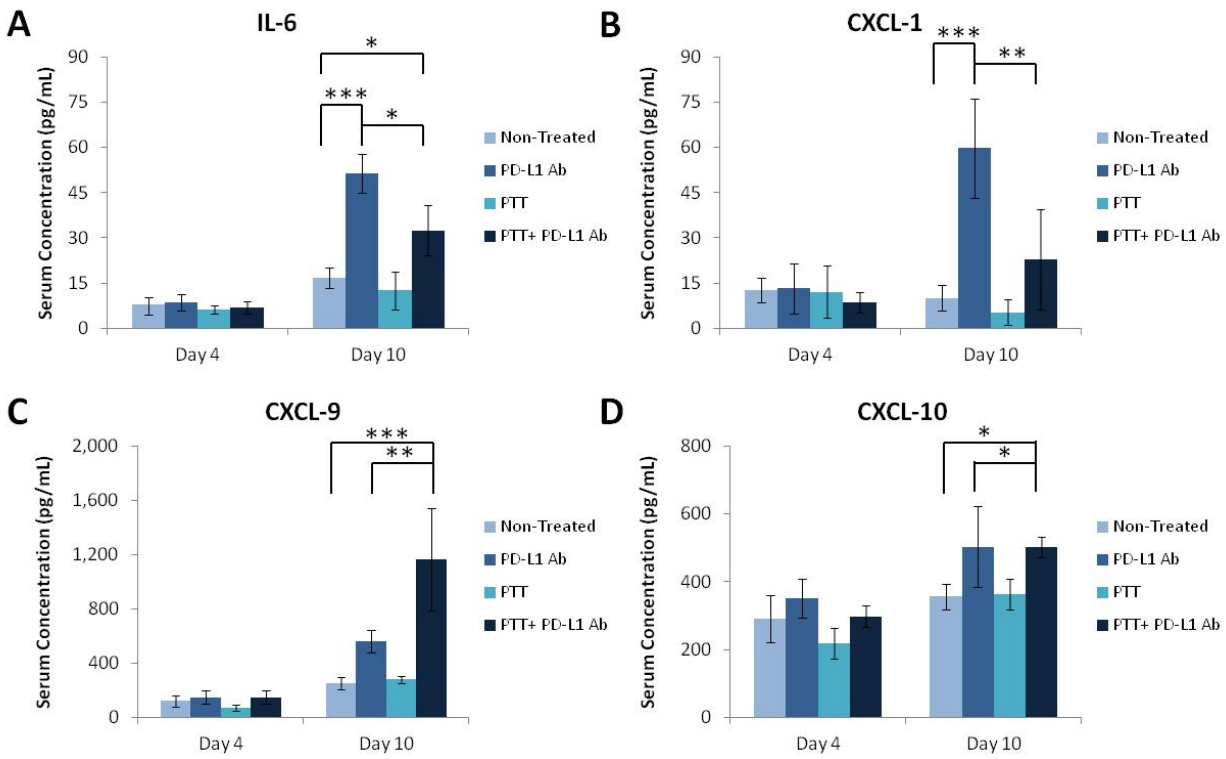

Figure 3.4. Serum concentrations of IL-6 (A), CXCL-1 (B), CXCL-9 (C), and CXCL-10 (D) on Day 4 and Day 10.

3.7 Acknowledgements

Others who contributed to this work include Nicholas O. Stevers[1], Hongwei Chen[1], Joseph P. Burnett[1], Aaron Robida[2], Max S. Wicha[3], Qiao Li and Duxin Sun[1]. I would like to thank Sean McDermott[3] and Feng Ni[1] for their thoughtful input, as well as Mike Pihalja at the University of Michigan Flow Cytometry Core, Alan Burgess at the University of Michigan Comprehensive Cancer Center Tissue Core, and Joel Whitfield at Immunology Core. This work was supported in part by the University of Michigan Rackham Pre-Doctoral Fellowship (H. Paholak).

[1]Pharmaceutical Sciences Department, University of Michigan
[2]Flow Cytometry Core, University of Michigan

[3]Department of Internal Medicine, University of Michigan
[4]Department of Surgery, University of Michigan

3.8 References

1. Lu, J., et al., *Breast cancer metastasis: challenges and opportunities.* Cancer Res, 2009. **69**(12): p. 4951-3.

2. McArthur, H.L. and P.G. Morris, *Aromatase inhibitor strategies in metastatic breast cancer.* Int J Womens Health, 2010. **1**: p. 67-72.

3. Telli, M.L. and R.W. Carlson, *First-line chemotherapy for metastatic breast cancer.* Clin Breast Cancer, 2009. **9 Suppl 2**: p. S66-72.

4. *Incidence and Incidence Rates.* Metastatic Breast Cancer Network, 2015.

5. Liu, S., et al., *Breast cancer stem cells transition between epithelial and mesenchymal states reflective of their normal counterparts.* Stem Cell Reports, 2014. **2**(1): p. 78-91.

6. Wicha, M.S., S. Liu, and G. Dontu, *Cancer stem cells: an old idea--a paradigm shift.* Cancer Res, 2006. **66**(4): p. 1883-90; discussion 1895-6.

7. Ginestier, C., et al., *ALDH1 is a marker of normal and malignant human mammary stem cells and a predictor of poor clinical outcome.* Cell Stem Cell, 2007. **1**(5): p. 555-67.

8. Al-Hajj, M., et al., *Prospective identification of tumorigenic breast cancer cells.* Proc Natl Acad Sci U S A, 2003. **100**(7): p. 3983-8.

9. Atkinson, R.L., et al., *Thermal enhancement with optically activated gold nanoshells sensitizes breast cancer stem cells to radiation therapy.* Sci Transl Med, 2010. **2**(55): p. 55ra79.

10. Conley, S.J., et al., *Antiangiogenic agents increase breast cancer stem cells via the generation of tumor hypoxia.* Proc Natl Acad Sci U S A, 2012. **109**(8): p. 2784-9.

11. Creighton, C.J., et al., *Residual breast cancers after conventional therapy display mesenchymal as well as tumor-initiating features.* Proc Natl Acad Sci U S A, 2009. **106**(33): p. 13820-5.

12. Korkaya, H., et al., *Activation of an IL6 inflammatory loop mediates trastuzumab resistance in HER2+ breast cancer by expanding the cancer stem cell population.* Mol Cell, 2012. **47**(4): p. 570-84.

13. Li, X., et al., *Intrinsic resistance of tumorigenic breast cancer cells to chemotherapy.* J Natl Cancer Inst, 2008. **100**(9): p. 672-9.

14. Phillips, T.M., W.H. McBride, and F. Pajonk, *The response of CD24(-/low)/CD44+ breast cancer-initiating cells to radiation.* J Natl Cancer Inst, 2006. **98**(24): p. 1777-85.

15. Wang, R., P.S. Billone, and W.M. Mullett, *Nanomedicine in Action: An Overview of Cancer Nanomedicine on the Market and in Clinical Trials.* Journal of Nanomaterials, 2013. **2013**: p. 12.

16. Day, E.S., J.G. Morton, and J.L. West, *Nanoparticles for Thermal Cancer Therapy.* Journal of Biomechanical Engineering-Transactions of the Asme, 2009. **131**(7).

17. Toraya-Brown, S., et al., *Local hyperthermia treatment of tumors induces CD8(+) T cell-mediated resistance against distal and secondary tumors.* Nanomedicine, 2014. **10**(6): p. 1273-85.

18. Zhao, Q., et al., *Magnetic nanoparticle-based hyperthermia for head & neck cancer in mouse models.* Theranostics, 2012. **2**: p. 113-21.

19. *Aurolase Therapy.* Nanospectra.

20. *Pilot Study of AuroLase(tm) Therapy in Refractory and/or Recurrent Tumors of the Head and Neck.* ClinicalTrials.gov.

21. *Efficacy Study of AuroLase Therapy in Subjects With Primary and/or Metastatic Lung Tumors.* ClinicalTrials.gov.

22. Chen, H.W., et al., *Highly crystallized iron oxide nanoparticles as effective and biodegradable mediators for photothermal cancer therapy.* Journal of Materials Chemistry B, 2014. **2**(7): p. 757-765.

23. Bear, A.S., et al., *Elimination of metastatic melanoma using gold nanoshell-enabled photothermal therapy and adoptive T cell transfer.* PLoS One, 2013. **8**(7): p. e69073.

24. Wang, C., et al., *Immunological Responses Triggered by Photothermal Therapy with Carbon Nanotubes in Combination with Anti-CTLA-4 Therapy to Inhibit Cancer Metastasis.* Advanced Materials, 2014. **26**(48): p. 8154-8162.

25. *The Role of Anti-PD-L1 Immunotherapy in Cancer.* OncLive, 2014.

26. Chen, D.S. and I. Mellman, *Oncology meets immunology: the cancer-immunity cycle.* Immunity, 2013. **39**(1): p. 1-10.

27. Postow, M.A., M.K. Callahan, and J.D. Wolchok, *Immune Checkpoint Blockade in Cancer Therapy.* J Clin Oncol, 2015. **33**(17): p. 1974-82.

28. Restifo, N.P., M.E. Dudley, and S.A. Rosenberg, *Adoptive immunotherapy for cancer: harnessing the T cell response.* Nat Rev Immunol, 2012. **12**(4): p. 269-81.

29. Kalos, M. and C.H. June, *Adoptive T cell transfer for cancer immunotherapy in the era of synthetic biology.* Immunity, 2013. **39**(1): p. 49-60.

30. Lee, S. and K. Margolin, *Cytokines in cancer immunotherapy.* Cancers (Basel), 2011. **3**(4): p. 3856-93.

31. Moghimi, S.M., A.C. Hunter, and J.C. Murray, *Long-circulating and target-specific nanoparticles: Theory to practice.* Pharmacological Reviews, 2001. **53**(2): p. 283-318.

32. Maeda, H., et al., *Tumor vascular permeability and the EPR effect in macromolecular therapeutics: a review.* J Control Release, 2000. **65**(1-2): p. 271-84.

33. Brigger, I., C. Dubernet, and P. Couvreur, *Nanoparticles in cancer therapy and diagnosis.* Advanced Drug Delivery Reviews, 2002. **54**(5): p. 631-651.

34. Kim, R.J. and J.S. Nam, *OCT4 Expression Enhances Features of Cancer Stem Cells in a Mouse Model of Breast Cancer.* Lab Anim Res, 2011. **27**(2): p. 147-52.

35. Park, S.J., R.J. Kim, and J.S. Nam, *Inhibitor of DNA-binding 4 contributes to the maintenance and expansion of cancer stem cells in 4T1 mouse mammary cancer cell line.* Lab Anim Res, 2011. **27**(4): p. 333-8.

36. Kim, R.J., et al., *High aldehyde dehydrogenase activity enhances stem cell features in breast cancer cells by activating hypoxia-inducible factor-2alpha.* Cancer Lett, 2013. **333**(1): p. 18-31.

37. Chen, H., et al., *Anti-HER2 antibody and ScFvEGFR-conjugated antifouling magnetic iron oxide nanoparticles for targeting and magnetic resonance imaging of breast cancer.* Int J Nanomedicine, 2013. **8**: p. 3781-94.

38. Shi, L., et al., *The role of PD-1 and PD-L1 in T-cell immune suppression in patients with hematological malignancies.* J Hematol Oncol, 2013. **6**(1): p. 74.

39. Korman, A.J., K.S. Peggs, and J.P. Allison, *Checkpoint blockade in cancer immunotherapy.* Adv Immunol, 2006. **90**: p. 297-339.

40. Hirano, F., et al., *Blockade of B7-H1 and PD-1 by monoclonal antibodies potentiates cancer therapeutic immunity.* Cancer Res, 2005. **65**(3): p. 1089-96.

41. Teitz-Tennenbaum, S., et al., *Targeting cancer stem cells via dendritic-cell vaccination.* Oncoimmunology, 2012. **1**(8): p. 1401-1403.

42. Ning, N., et al., *Cancer stem cell vaccination confers significant antitumor immunity.* Cancer Res, 2012. **72**(7): p. 1853-64.

43. Lu, L., et al., *Cancer stem cell vaccine inhibits metastases of primary tumors and induces humoral immune responses against cancer stem cells.* Oncoimmunology, 2015. **4**(3): p. e990767.

44. Tao, K., et al., *Imagable 4T1 model for the study of late stage breast cancer.* BMC Cancer, 2008. **8**: p. 228.

45. Chen, L., et al., *Rejection of metastatic 4T1 breast cancer by attenuation of Treg cells in combination with immune stimulation.* Mol Ther, 2007. **15**(12): p. 2194-202.

46. Chen, J.G., et al., *Intratumoral expression of IL-17 and its prognostic role in gastric adenocarcinoma patients.* Int J Biol Sci, 2011. **7**(1): p. 53-60.

47. Gorbachev, A.P., Marianne, *Expression of CXCL9/Mig in the tumor microenvironment is critical for recruitment of CD8 T cells and suppression of cutaneous tumor growth.* The Journal of Immunology, 2011. **186**.

48. Dunn, G.P., L.J. Old, and R.D. Schreiber, *The three Es of cancer immunoediting.* Annu Rev Immunol, 2004. **22**: p. 329-60.

49. Schreiber, R.D., L.J. Old, and M.J. Smyth, *Cancer immunoediting: integrating immunity's roles in cancer suppression and promotion.* Science, 2011. **331**(6024): p. 1565-70.

50. McNally, A., et al., *CD4+CD25+ regulatory T cells control CD8+ T-cell effector differentiation by modulating IL-2 homeostasis.* Proc Natl Acad Sci U S A, 2011. **108**(18): p. 7529-34.

51. Waitz, R., et al., *Potent induction of tumor immunity by combining tumor cryoablation with anti-CTLA-4 therapy.* Cancer Res, 2012. **72**(2): p. 430-9.

52. Rasheed, Z., Q. Wang, and W. Matsui, *Isolation of stem cells from human pancreatic cancer xenografts.* J Vis Exp, 2010(43).

53. Holmes, K., et al., *Preparation of cells and reagents for flow cytometry.* Curr Protoc Immunol, 2001. **Chapter 5**: p. Unit 5 3.

54. Mansfield, J.R., C. Hoyt, and R.M. Levenson, *Visualization of microscopy-based spectral imaging data from multi-label tissue sections.* Curr Protoc Mol Biol, 2008. **Chapter 14**: p. Unit 14 19.

55. Mansfield, J.R., *Immune Cell Phenotyping in Solid Tumors using Quantitative Pathology.*

56. *Phenotyping Immune Cell Subsets in situ in FFPE Tissue Sections.* Perkin Elmer, 2015.

57. Storm, G., et al., *Surface Modification of Nanoparticles to Oppose Uptake by the Mononuclear Phagocyte System.* Advanced Drug Delivery Reviews, 1995. **17**(1): p. 31-48.

58. Dreaden, E.C., et al., *Size matters: gold nanoparticles in targeted cancer drug delivery.* Ther Deliv, 2012. **3**(4): p. 457-78.

59. Guo, S.T. and L. Huang, *Nanoparticles Escaping RES and Endosome: Challenges for siRNA Delivery for Cancer Therapy.* Journal of Nanomaterials, 2011.

60. Characiejus, D., et al., *Prediction of response in cancer immunotherapy.* Anticancer Res, 2011. **31**(2): p. 639-47.

61. Blankenstein, T., et al., *The determinants of tumour immunogenicity.* Nat Rev Cancer, 2012. **12**(4): p. 307-13.

62. Kim, K., et al., *Eradication of metastatic mouse cancers resistant to immune checkpoint blockade by suppression of myeloid-derived cells.* Proc Natl Acad Sci U S A, 2014. **111**(32): p. 11774-9.

63. Le, H.K., et al., *Gemcitabine directly inhibits myeloid derived suppressor cells in BALB/c mice bearing 4T1 mammary carcinoma and augments expansion of T cells from tumor-bearing mice.* Int Immunopharmacol, 2009. **9**(7-8): p. 900-9.

64. Monu, N.R. and A.B. Frey, *Myeloid-derived suppressor cells and anti-tumor T cells: a complex relationship.* Immunol Invest, 2012. **41**(6-7): p. 595-613.

65. Huang, B., et al., *Gr-1+CD115+ immature myeloid suppressor cells mediate the development of tumor-induced T regulatory cells and T-cell anergy in tumor-bearing host.* Cancer Res, 2006. **66**(2): p. 1123-31.

66. Acharyya, S., et al., *A CXCL1 paracrine network links cancer chemoresistance and metastasis.* Cell, 2012. **150**(1): p. 165-78.

67. Kaur, P., et al., *A mouse model for triple-negative breast cancer tumor-initiating cells (TNBC-TICs) exhibits similar aggressive phenotype to the human disease.* BMC Cancer, 2012. **12**: p. 120.

68. Lee, C.M., *Characterization of murine and human breast cancer stem cells in vitro and in vivo.* 2014.

69. Kruger, J.A., et al., *Characterization of stem cell-like cancer cells in immune-competent mice.* Blood, 2006. **108**(12): p. 3906-12.

70. Wang, X.-r.S., Bao-en; Ai, Jun; Liu, Li-hua, Liu, Yue-cai, Zhang, Chao; Zhang, Hai-pu; Liu, Deng-xiang, *Enrichment and identification of cancer stem cell-like cells in mouse breast cancer cell line 4T1.* Chinese Journal of Cancer Biotherapy, 2010. **17**(4): p. 381-385.

71. Deng, L., et al., *Irradiation and anti-PD-L1 treatment synergistically promote antitumor immunity in mice.* J Clin Invest, 2014. **124**(2): p. 687-95.

72. Chen, H.W., et al., *Reducing non-specific binding and uptake of nanoparticles and improving cell targeting with an antifouling PEO-b-P gamma MPS copolymer coating.* Biomaterials, 2010. **31**(20): p. 5397-5407.

CHAPTER 4. OPTIMIZING CANCER CELL UPTAKE OF GOLD NANOPARTICLES BY 'LIVING' PEGYLATION TO CONTROL TARGETING LIGAND AND CHARGE DENSITIES

4.1 Abstract

After decades of cancer treatment dominated by non-specific therapies with detrimental side effects and often resulting in development of resistance and recurrence, nanotechnology offers tremendous untapped potential in the movement toward more specific, personalized cancer therapies. One of few nanoparticle-based treatments to enter clinical trials in human cancer patients is localized photothermal therapy (PTT) activated by near infrared (NIR) light-absorbing gold nanoshells, which currently accumulate in tumor tissue through passive targeting. Patient tolerance and response to such therapy may benefit from formulation to develop stealthy, actively targeted nanoparticles. Here we report and demonstrate biomedical applications of a new technique – 'living' PEGylation – that allows control of the density and composition of heterobifunctional PEG (HS-PEG-R) on gold nanoparticles (AuNPs). We first establish 'living' PEGylation by incubating HS-PEG_{5000}-COOH with AuNPs (~20 nm) at increasing molar ratios from zero to 2000. This causes the hydrodynamic layer thickness to differentially increase up to 26 nm. The controlled, gradual increase in PEG-COOH density is revealed after centrifugation, based on the ability to re-suspend the pellet and increase the AuNP absorption. Using a

fluorescamine-based assay we quantify differential HS-PEG_{5000}-NH_2 binding to AuNPs, revealing it is highly efficient until AuNP saturation. Furthermore, the zeta potential incrementally changes from −44.9 to +52.2 mV and becomes constant upon saturation. Using 'living' PEGylation we prepare AuNPs with different ratios of HS-PEG-RGD and incubate them with U-87 MG and non-target cells, demonstrating that targeting ligand density is critical to maximizing the targeting efficiency of AuNPs to cancer cells. The ability to minimize non-specific binding/uptake by healthy cells could further improve targeted nanoparticle efficacy. Consequently, we sequentially control the HS-PEG-R density to develop multifunctional nanoparticles, conjugating positively-charged HS-PEG-NH_2 at increasing ratios to AuNPs containing negatively-charged HS-PEG-COOH to reduce uptake by macrophage cells. Application of this facile PEGylation technique to PTT-mediating nanoparticles to enhance the ratio of uptake by target versus non-target cells could significantly improve patient response and decrease both the dose and cost of treatment. Furthermore, future work to enhance formulation of such stealthy, targeted nanoparticles to confer imaging capabilities could potentially enable PTT to be applied to metastatic cancers.

4.2 Introduction

The ability to target delivery of nanoparticles to solid tumors and minimize their distribution to non-target sites are critical tasks in the development of cancer nanomedicine for *in vivo* molecular imaging and targeted therapy [1]. It is generally accepted that the presentation of multiple targeting ligands on nanoparticle surfaces can improve cell targeting. A variety of tumor-targeting ligands, such as the RGD peptide [2], epidermal growth factor (EGF) [3], folate

[4], transferrin (Tf) [5], or antibodies and antibody fragments, such as a single-chain variable fragment (scFv) [6], have been used to facilitate the binding/uptake of carriers to target cells. However, little work has been done to determine whether an optimal ligand density exists [7].In order to achieve an effective level of nanoparticles in the targeted tissue or tumor site, targeted nanoparticles should transition from circulating blood to the tissue of interest and bind to their molecular target as a first step in nanoparticle retention or cellular internalization. The reality is that even with targeting ligands, many types of systemically delivered nanoparticles are rapidly cleared from the blood stream through non-specific uptake by the reticuloendothelial system (RES) and the mononuclear phagocytic system (MPS) in the liver, spleen, and bone marrow [8]. This results in reduced bioavailability of the targeting agents, a low therapeutic index, and potential toxicity to normal organs. Therefore, enhancing target-ligand interactions and reducing both non-specific binding by biomolecules and uptake of nanoparticles by the RES are major challenges for improving the sensitivity and specificity of biomarker targeted nanoparticles.

Gold nanoparticles (AuNPs) have been attracting increasingly widespread interest as a multifunctional platform for various applications in biology and medicine [9-12]. AuNPs are particularly useful for these applications, as they can function as contrast agents in optical imaging [13-15], sensitizers for Raman scattering-based diagnostic probes [16-18], and as vectors for photothermal therapy [19-21]. A key feature of nanoparticle agents is their multifunctionality; the ability to append ligands, antibodies, imaging labels, drugs, or other molecules to nanoparticles enables targeted molecular imaging and therapy [22-24]. AuNPs serve as an excellent platform to attach functional moieties facilely due to a strong Au-S linkage formed using thiol-terminated poly(ethylene glycol) (HS-PEG-R) molecules [25].

For biomedical applications of AuNPs using PEG molecules with functional R-groups, the ability to control the PEG-R chain density can have profound implications. An optimal targeting ligand density on nanoparticles might enhance their targeting efficiency to tumors with minimized non-specific uptake by healthy tissues and organs. While advances have been made in the development of functionalized AuNPs, current AuNP synthesis approaches lack the ability to subsequently control PEG chain density and therefore the density and stability of the functional groups coating the AuNPs [26-30]. Traditional PEGylation on chemically made AuNPs is typically achieved through a ligand exchange process by using thiol-terminated PEG molecules to replace the original capping ligands (e.g., citrate). Therefore, stabilization of AuNPs during PEGylation requires excessive PEG molecules [16, 26, 27], making it impossible to control the PEG-R chain density on AuNPs.

Here we report a 'living' PEGylation technique with the ability to control the density of functional PEG chains, and thus the targeting ligand or charge density, on AuNPs. The principle behind this technique is similar to that of living polymerization, which is widely used by polymer chemists to control chain length by changing the ratio of monomer/initiator to build di-block or tri-block copolymers [31]. For our studies we used AuNPs made by femtosecond laser ablation [32, 33]. Different from traditional AuNPs made by chemical synthesis, AuNPs made by femtosecond laser ablation have 'naked' surfaces without any capping ligands. Consequently, it is possible to develop stable AuNP formulations while controlling the molar ratio of HS-PEG-R/AuNP, when it is below the saturation ratio. PEGylation is so efficient that essentially all of the added HS-PEG-R molecules become bound to the AuNPs. Using 'living' PEGylation, we investigate the potential to improve key requirements for targeted nanomedicine. First we control the targeting ligand density on AuNPs to optimize the specific targeting ability to cancer cells.

Furthermore, via 'living' PEGylation we can add PEG-R chains in sequential steps to AuNPs, controlling the density of different functional PEG-R chains on the nanoparticles. Using this controlled, sequential PEGylation we develop double-charged AuNPs, conjugating positively-charged HS-PEG-NH_2 at increasing ratios to AuNPs containing negatively-charged HS-PEG-COOH, to reduce uptake by macrophage cells. Therefore, this unique PEGylation process using laser-produced AuNPs facilitates unprecedented control over the development of multifunctional nanoparticles, with implications for both therapeutic and diagnostic nanoparticle applications. Of particular interest is its potential application in clinical trials for nanoparticles capable of photothermal therapy.

4.3 Results and Discussion

In our first step to establish 'living' PEGylation, we mixed gold nanoparticles (~20 nm in diameter based on TEM imaging) with HS-PEG-COOH at different HS-PEG-COOH/AuNP molar ratios from zero to 2000. This molar ratio range was chosen based on the surface area of 20 nm AuNP and the footprint of PEG molecules. For PEGylation we selected thiolated PEG_{5000}, which is most widely used to modify gold nanoparticles [30, 34]. The thiol concentration (>95%) was confirmed by an Ellman's test. During PEGylation the AuNP concentration was fixed at 1.0 nM, determined by correlating our measured extinction spectra to the experimentally determined extinction cross-section data (8.8×10^8 $M^{-1}cm^{-1}$ for AuNPs with a diameter of 20 nm) [35].

Control over the AuNP PEGylation process was monitored by the change in particle size. As shown in Figure 4.1, the change in hydrodynamic layer thickness differentially increased with increasing molar ratios of HS-PEG-COOH/AuNP and reached a constant at 26 nm after the

AuNP surface was saturated at molar ratio of 500. This revealed an increase in PEG chain density on AuNP surfaces upon increasing the HS-PEG-COOH/AuNP molar ratio. For free PEG molecules in a good solvent, the radius of gyration R_g can be empirically calculated as shown in equation (1):

$$R_g[nm] = 0.181 \times N^{0.58} \quad (1)$$

where N is the number of ethylene glycol (EG) monomer units per PEG chain [36]. For the PEG_{5000} used here, R_g is 2.8 nm and the size increase should be around 11.2 nm (2.8 × 4) if the PEG chains form isolated hemispheres (mushroom) on the surface with a critical PEG density σ^* ($1/\pi R_g^2$) around 0.04 PEG/nm^2. At a molar ratio of 500 the PEG density σ is around 0.4 PEG/nm^2, which is 10 times higher than the critical grafting density [29]. The grafting PEG chains are most likely reconfigured, stretching out in a brush conformation as shown in the insert of Figure 4.1. This explains why the hydrodynamic layer thickness (ΔD) is more than four times the radius of gyration.

Figure 4.S1(a) shows the optical spectra of AuNPs at all HS-PEG-COOH/AuNP ratios. The overlapping curves and the constant OD reveal that there is no loss of AuNPs after PEGylation for each of the HS-PEG-COOH/AuNP molar ratios. This is in contrast to traditional PEGylation to citrate-capped AuNPs made by chemical synthesis, which requires a large excess of thiolated PEG molecules [27]. Otherwise, the citrate-capped gold colloids will not be stable [26]. The high colloidal stability of laser-made AuNPs after PEGylation with different molar ratios is attributed to the highly negatively-charged 'naked' surface in Figure 4.S1(b), which shows that the zeta potential is independent of the HS-PEG-COOH/AuNP molar ratio. Although there are not any capping ligands on the AuNP surfaces before PEGylation, the AuNPs made by

femtosecond pulse laser ablation have a natural negative surface with a zeta potential of about −33.3 mV. The negatively-charged surface is caused by partial oxidation from the oxygen present in solution, followed by proton transfer to adjacent hydroxide ions [37]. This natural negative surface free of capping ligands makes these laser-generated gold colloids unique from traditional ones in that PEGylation can be controlled.

The differential PEG-COOH chain densities on AuNPs after PEGylation at varying molar ratios of HS-PEG-COOH/AuNP were confirmed by centrifuging the solutions and re-suspending the pellet of AuNPs. Figure 4.2 compares the optical densities (OD) of the absorption peaks after centrifugation for each HS-PEG-COOH/AuNP molar ratio, and Figure 4.S2 shows typical absorption spectra. The data in Figure 4.2 clearly demonstrate the controlled increase in HS-PEG-COOH density with each AuNP formulation, as the HS-PEG-COOH/AuNP molar ratio dictates the stability of the formulations after centrifugation. For ratios less than 100 the AuNP pellet could not be re-dispersed after centrifugation, revealing the PEG-COOH chain density is too low to maintain a stable formulation. As the molar ratio increased from 100 to 300 the OD number increased by 25 times, with a relative change from 4% to 100% when compared to the OD before centrifugation, respectively. The data also indicate that even though the AuNP surface is not fully covered with PEG at a molar ratio of 300, the AuNPs are stable against centrifugation. This differential stability based on the changing HS-PEG-COOH density on AuNPs is also apparent in Figure 4.S2. As the molar ratio increased from 100 to 200 more AuNPs were recovered after centrifugation, determined by the increase of the absorption peak at 524 nm. However, detection of a second, smaller peak (or ‘bump’) at ~650 nm suggests these partially PEGylated AuNPs tend to form aggregates after centrifugation, indicating a higher PEG-COOH chain density is required to maintain stability.

To further analyze the PEGylation efficiency of our laser-made AuNPs we incubated HS-PEG-NH_2 with AuNPs at increasing molar ratios, which allowed us to use a fluorescamine-based assay to quantify HS-PEG-NH_2 binding to AuNPs [27]. We varied the HS-PEG-NH_2 concentration during incubation from 50 to 2000 nM while keeping the AuNP concentration constant at 1.0 nM. First we monitored the zeta potential values of the PEGylated AuNPs as shown in Figure 4.3(a). They gradually transformed from highly negative (−44.9 mV) at low molar ratios to highly positive (reaching +52.2 mV) and remained constant for molar ratios higher than 500, revealing the increasing PEG-NH_2 chain density on the AuNPs until the surfaces become saturated. Successful differential PEGylation was further demonstrated by monitoring the size increase after PEGylation with increasing HS-PEG-NH_2/AuNP molar ratios, as shown in Figure 4.S3. The data show that the hydrodynamic layer thickness incrementally increased up to 26 nm at the saturated HS-PEG-NH_2/AuNP molar ratio of 500, which is consistent with the PEGylation using HS-PEG-COOH. The data combined clearly reveal a controlled increase in the PEG-NH_2 chain density as we increased the HS-PEG-NH_2/AuNP molar ratio.

Using the fluorescamine-based assay we established a linear calibration curve for free HS-PEG-NH_2 (Figure 4.S4(b)) based on the peak intensity at 480 nm observed in the fluorescence spectra at PEG concentrations from 50 to 2000 nM (Figure 4.S4(a)). In this assay a non-fluorescent fluorescamine reacts with a primary amine to generate a compound that emits fluorescence at 480 nm when excited at 390 nm, as shown in Scheme 4.S1. Originally developed for quantification of primary amines in biomolecules, this assay has sensitivity on the pM scale [38]. After incubation with AuNPs followed by centrifugation, we quantified the concentration of free HS-PEG-NH_2 in the supernatants as shown in Figure 4.3(b) (corresponding fluorescence

spectra shown in Figure 4.S4(c)). Although the HS-PEG-NH_2 concentration increased 10 times up to 500 nM there was no obvious fluorescence increase after measuring the supernatants, whereas for ratios higher than 500 the supernatant fluorescence began to increase. This revealed that the gradual increase in HS-PEG-NH_2 binding to AuNPs is highly efficient below saturation at 500 nM, and this point of saturation is consistent with our zeta potential and size change measurements. Measuring the PEG concentration in supernatants to estimate the PEG chain density on AuNPs is a widely used method [27, 30]. However, in previous reports using chemically prepared AuNPs, more than 90% of the added HS-PEG-R molecules remained in the supernatants because of the excessive HS-PEG-R required to stabilize AuNPs during PEGylation [26]. In our case as most of the added HS-PEG-NH_2 molecules were bound to AuNPs, our assay measurements are more sensitive than those in the previous reports. The combined experiments using HS-PEG-COOH and HS-PEG-NH_2 demonstrate a highly efficient PEGylation process that allows control of the PEG density on AuNPs by manipulating the molar ratio of HS-PEG-R/AuNP, while the ratio is less than the saturated one. This technique is similar to living polymerization, through which a polymer chain length can be controlled by the ratio of monomer/initiator. Thus we termed this technique 'living' PEGylation.

One important application of 'living' PEGylation is to control the targeting ligand density on AuNPs to improve specific targeting efficiency. Consequently, we synthesized HS-PEG-RGD to investigate specific targeting efficacy of AuNPs to $\alpha_v\beta_3$ integrin receptors. The targeting peptide conjugation to PEG was performed based on traditional coupling reactions between NHS ester and amine groups using thiol-protected OPSS-PEG-NHS and cyclo(RGDfk)-NH_2 followed by deprotection of the thiol groups using DTT (Scheme 4.S2) [39, 40]. The expected HS-PEG-RGD was purified by a size exclusion column and confirmed by HPLC, with the retention time

shifting from 16.87 to 19.64 min compared to unconjugated RGD (Figure 4.S5) [41]. The characteristic peak of the optical spectrum of purified HS-PEG-RGD is identical to RGD alone, revealing the successful peptide conjugation (Figure 4.S6). An Ellman's test also confirmed effective deprotection to reveal a terminal free thiol. PEGylation using HS-PEG-RGD on AuNPs with serial HS-PEG-RGD/AuNP molar ratios was done as described for HS-PEG-COOH. Hydrodynamic size and zeta potential measurements were used to monitor the PEGylation process (Figure 4.S7). As expected, the hydrodynamic size of PEGylated AuNPs incrementally increased as we increased the molar ratio of HS-PEG-RGD/AuNP below the saturation ratio (Figure 4.S7(a)). The zeta potential data revealed that all PEG-RGD-modified AuNPs have highly negatively charged surfaces (~ −40 mV) (Figure 4.S7(b)). Taken together, the data clearly show that AuNPs with different PEG-RGD densities on the surface were successfully obtained in a controlled way.

Specific cellular targeting efficiency to cancer cells was tested using two cancer cell lines: U-87 MG, positive for $\alpha_v\beta_3$ integrin receptors, and MCF-7, classified negative for the receptor and serving as an example of non-target cells. The gold content inside the cells after digestion with aqua regia was measured by ICP-OES. Using the same conditions as for live cell incubations the stability of these PEGylated AuNPs in media was first confirmed by the optical spectra in Figure 4.S8, as there is no change of peak OD over four hours in DMEM plus 10% FBS.

The effect of the PEG-RGD/AuNP ratio on cellular uptake after incubation with AuNPs is shown in Figure 4.4(a) for U-87 MG cells and in Figure 4.4(b) for MCF-7 cells. These data clearly show that U-87 MG cells uptake more AuNPs modified with RGD than MCF-7 cells, which demonstrates the specific targeting ability of the RGD peptide [2, 41]. Furthermore, for

incubations with AuNPs with PEG-RGD/AuNP molar ratios of 50 or lower U-87 MG cells demonstrate consistently increased uptake as the PEG-RGD/AuNP molar ratio is increased, with uptake reaching up to 3.7 pg/cell as the ratio increased to 50. On the contrary, MCF-7 cells uptake is independent of PEG-RGD density change in this range, which is around 0.2 pg/cell and 18-fold lower than in U-87 MG cells. For AuNPs with PEG-RGD/AuNP molar ratios higher than 50, uptake in both U-87 MG cells and MCF-7 cells began to increase with increasing RGD density. Comparing Figures 4.4(a) and 4.4(b), the relative uptake of U-87 MG (compared to MCF-7) versus PEG-RGD chain density revealed a clear optimal targeting ligand density around 50 PEG-RGD on each AuNP that maximizes specific uptake by target cells while minimizing uptake in non-target cells.

We next incubated MCF-7 cells with AuNPs containing a control RAD peptide that does not specifically target $\alpha_v\beta_3$ integrin receptors in order to determine whether the increased gold content in MCF-7 cells for PEG-RGD/AuNP molar ratios higher than 50 was caused by non-specific uptake [42]. We found that the gold content in MCF-7 cells does not increase for even the highest PEG-RAD/AuNP molar ratios (Figure 4.S9). This suggests that the rise in uptake observed for higher molar ratios of PEG-RGD/AuNP in Figure 4.4(b) is from specific uptake due to very low expression of $\alpha_v\beta_3$ integrin receptors on MCF-7 cells, triggered by a threshold RGD density. Consequently, we decided to next investigate the potential for targeting ligand density to affect non-specific uptake by macrophage cells.

Figure 4.5 shows the uptake of AuNPs with different PEG-RGD surface densities after incubation with macrophage cells. Similar to the trend observed in MCF-7 cells in Figure 4.4(b), for molar ratios below 50 the uptake is independent of the targeting ligand density while above 50 the uptake consistently increases with increasing ligand density. This suggests $\alpha_v\beta_3$ integrin

receptors are present on macrophage cells [43], and this can trigger increased nanoparticle uptake at higher PEG-RGD densities on AuNPs. Taken with the results of Figure 4.4, this confirms it is possible to control the targeting ligand density on AuNPs and that it plays a critical role in optimizing specific targeting efficacy.

Another application of 'living' PEGylation is to control PEG-R chain densities on AuNPs in a sequential way for multifunctional purposes, like building di-block or tri-block copolymers using living polymerization. Here we investigated a two-step PEGylation process, first partially PEGylating with HS-PEG-R_1 and then PEGylating with HS-PEG-R_2 as shown in Scheme 4.1. As long as the AuNPs are not saturated (i.e. the molar ratio of HS-PEG-R/AuNP is lower than 500), one can control the density of functional moieties (R groups) covalently attached to AuNPs. In this sequential way, double-charged AuNPs with varying PEG-NH_2/PEG-COOH molar ratios were prepared by partially PEGylating with HS-PEG-COOH first, then adding different amounts of HS-PEG-NH_2, and finally adding more HS-PEG-COOH to saturate the surface.

The different double-charged AuNP formulations containing both HS-PEG-NH_2 and HS-PEG-COOH were incubated with RAW 264.7 macrophage cells and the uptake results are shown in Figure 4.6. The data show that by increasing the ratio of PEG-NH_2 on AuNPs from 50 to 300 through living PEGylation, the non-specific uptake of Au/cell (pg) gradually halved from 0.63 ± 0.01 to 0.33 ± 0.01. The reduced cell uptake can be explained by the overall surface charge becoming more neutral with controlled addition of more PEG-NH_2, as shown in Figure 4.S10. These results are consistent with those obtained by Liu et al for AuNPs modified via zwitterionic self-assembled monolayers (SAMs) composed of both negatively- and positively-charged, thiol-containing carbon chains [44].Compared to AuNPs modified with only negatively-charged carbon chains, as they increased the ratio of positive to negative carbon chains on the AuNP

surfaces the negative zeta potential gradually increased and reduced the AuNP uptake by macrophage cells.

In Figure 4.6 we also observe that our double-charged AuNP formulations have less non-specific uptake than all of the control AuNPs decorated with a single type of PEG-R (i.e. -OCH_3, -COOH, -NH_2). For instance, the double-charged AuNP formulations show a relative uptake ranging from 40% to 76% when compared to AuNP-PEG-OCH_3, the control with the least uptake. As expected, the AuNP control containing only HS-PEG-NH_2 exhibits the greatest non-specific uptake due to the electrostatic attraction between the positively-charged AuNPs and the negatively-charged cell membrane [45-48]. The uptake of the negatively-charged AuNP-PEG-COOH control is greater than those for each double-charged AuNPs for two reasons. First, phagocytic cells preferentially uptake anionic particles versus those that are more neutral in charge [44, 46, 49]. Second, the zwitterionic property of double-charged AuNPs confers stealth due to a layer of tightly bound water molecules on the AuNP surface. This has been shown to reduce binding of plasma proteins, and recognition and non-specific uptake by cells [44, 45, 50-53]. This also explains why the uptake of the double-charged AuNPs is reduced even when compared to the neutral AuNP-PEG-OCH_3 control. Our uptake results for the double-charged AuNPs relative to the positively-charged and negatively-charged controls are consistent with those of Liu et al in RAW 264.7 macrophage cells [44]. Furthermore, they observed the same uptake trend based on AuNP charge/zeta potential in normal human umbilical vein endothelial cells (HUVEC) and human hepatocellular liver carcinoma cells (HepG2), with one slight difference. They found that in the macrophage cells the reduction in uptake of double-charged AuNPs relative to the negatively-charged AuNPs is greater than those observed in the two non-phagocytic cell lines, and they attribute this to the preferential uptake of anionic particles by

phagocytic cells. Overall, our cellular uptake data with sequentially modified double-charged AuNPs exemplifies a second approach to reduce nanoparticle clearance by the immune system. Even greater potential to maximize specific uptake in target cells while minimizing non-specific uptake lies in an AuNP formulation containing both an optimal targeting ligand density and double-charged surface obtained by 'living' PEGylation, and merits further exploration. Our data suggests a facile and feasible approach would be to sequentially PEGylate using negatively-charged HS-PEG-COOH and an optimal density of HS-PEG-R_1, where R_1 represents a positively-charged targeting ligand.

Enhanced stability to partial PEGylation in a sequential way makes laser-made, 'naked' AuNPs unique from chemically-made ones capped with citrate, as demonstrated in the photograph in Figure 4.S11. While all commercial and laser-made AuNP formulations are stable if excessively PEGylated with HS-PEG-R (irrespective of charge), only laser-made AuNPs are stable after sequential PEGylation involving HS-PEG-NH_2. In AuNPs capped with citrate, this causes aggregation of the AuNPs and the solutions become black. Our work collectively demonstrates that this new PEGylation process with laser-made AuNPs facilitates creation of multifunctional AuNPs with a range of biomedical applications, including photothermal therapy if expanded to laser-produced, near infrared light-absorbing gold nanoparticles.

4.4 Conclusions

Using gold nanoparticles generated by femtosecond pulse laser ablation we revealed the unique ability to control the density of HS-PEG-R (-COOH, -NH_2, and -RGD) conjugated to AuNP surfaces for one or sequential rounds of conjugation, terming this process 'living'

PEGylation. After PEGylation with HS-PEG-COOH at different molar ratios of HS-PEG-COOH/AuNP up to 2000, the hydrodynamic layer thickness incrementally increased with increasing molar ratio and became constant upon AuNP saturation. We then centrifuged and re-suspended the PEGylated AuNP to demonstrate the differential PEG chain density on the AuNP surface. As the PEG-COOH/AuNP molar ratio increased to the point of saturation, the OD for the absorption spectrum peak gradually increased up to 25 times and the AuNP recovery consistently increased. Next, PEGylation using HS-PEG-NH_2 was quantified by a fluorescamine-based assay. For differential HS-PEG-NH_2 ratios below the saturation ratio, essentially all the added HS-PEG-NH_2 bound to the AuNPs. Furthermore, as the molar ratio of HS-PEG-NH_2/AuNP increased the zeta potential incrementally changed from −44.9 to +52.2 mV and became constant upon AuNP saturation. Taken together, our results confirm that the PEG-R chain density on AuNP surfaces can be precisely controlled by changing the molar ratio of HS-PEG-R/AuNP. Next we used 'living' PEGylation to investigate the dependence of specific targeting efficacy on targeting ligand density on nanoparticle surfaces, controlling the density of the model peptide RGD to AuNPs via HS-PEG-RGD. An optimal targeting ligand density around 50 PEG-RGD on each AuNP maximizes the specific targeting efficiency to U-87 MG cancer cells. Additionally, we sequentially conjugated HS-PEG-COOH and HS-PEG-NH_2 to AuNPs to create double-charged AuNPs with precise control over the PEG-NH_2/PEG-COOH ratio to reduce non-specific uptake by macrophage cells. This unique PEGylation process facilitates unprecedented control in the synthesis of multifunctional nanoparticles, with implications for both therapeutic and diagnostic nanoparticle development. Of particular interest is its potential application for photothermal therapy, given its advancement to clinical trials in human cancer patients.

4.5 Materials and Methods

Materials and Instrumentation: HS-PEG_{5000}-NH_2, HS-PEG_{5000}-COOH, and ortho-pyridyl-disulfide-PEG-succinimidyl ester (OPSS-PEG-NHS, 5 kD) were purchased from Creative PEGWorks (Winston-Salem, NC). HS-PEG_{5000}-OCH_3 was purchased from NanoCS. Cyclo (Arg-Gly-Asp-*D*-Phe-Lys) (RGD-NH_2, Peptides International, Inc) were used as received. Fluorescamine, Ellman's reagents, and all other solvents were obtained from Sigma-Aldrich. Milli-Q water (18.2 MΩ cm) was prepared using Milli-Q Academic water purification system (Billerica, MA). UV visible spectra were recorded in a BioTek micro plate reader (Synergy 2). A luminescence spectrometer LS-50B (Perkin Elmer, UK) was used to characterize the emission spectra of the fluorescamine assay. The nanoparticle hydrodynamic size and zeta potential were measured using a dynamic light scattering (DLS) instrument (Malvern Zeta Sizer Nano S-90) equipped with a 22 mW He-Ne laser operating at $\lambda = 632.8$ nm. The AuNPs were viewed by transmission electron microscopy (TEM) (Philips CM-100 60 kV).

Preparation of AuNPs: AuNPs were generated by laser ablation with the following laser parameters. Femtosecond pulses delivered from the above-stated laser system (repetition rate of 100 kHz, 10 μJ pulse energy, 700 fs pulse width centered at a wavelength of 1.045 μm) were focused onto a spot size of about 50 μm on a gold metal plate (99.99% purity) placed on the bottom of a glass vessel filled with 20 mL of deionized water. After a couple of days of aging, the top clear red solution was collected.

PEGylation of AuNPs with HS-PEG-R: In a typical process, 1.0 mL of AuNP solution (1.0 nM) was added with 10 μL of HS-PEG-R solution at different concentrations to obtain the following final molar ratios: 0, 50, 80,100, 150, 200, 300, 400, 500, 600, 800, 1000, 2000. The

reaction mixture was vortexed immediately and then incubated at room temperature for two days. After PEGylation, half of each solution was used for measuring absorption spectra, hydrodynamic size and zeta potential. The other half of each solution was centrifuged at 14000 rpm for 20 min and re-dispersed with Milli-Q water by gentle shaking. This process was repeated three times. For PEGylation using HS-PEG-NH_2, the supernatant after the first centrifugation was carefully collected and also centrifuged two more times to remove any remaining AuNPs. The resultant supernatant solution was analyzed via the fluorescamine assay. For the sequential PEGylation with a combination of both HS-PEG-COOH and HS-PEG-NH_2, AuNPs were first partially PEGylated with HS-PEG-COOH, then different amounts of HS-PEG-NH_2 was added.

Quantification of Unbound HS-PEG-NH_2 in Supernatant: For a typical fluorescamine assay, 400 μL of each supernatant solution or calibration solution (without mixing with AuNPs) was mixed with 20 μL of Na_2HPO_4 (0.2 M, pH 10.0) and then 4.0 μL of fluorescamine solution in DMSO (2 mM). After 15 min, fluorescence spectra (λ_{ex}: 390 nm, λ_{em}: 480 nm) were recorded. The fluorescence intensities at 480 nm for each solution were plotted as a function of the HS-PEG-NH_2/AuNP molar ratio.

Preparation of HS-PEG-RGD and PEGylation to AuNPs: To a 25-mL round bottom flask, 50.1 mg of OPSS-PEG-NHS were dissolved in 1.0 mL of benzene. The solution was frozen before evaporating the solvent under reduced pressure to remove trace amounts of water. Anhydrous DMF (10 mL) was added to dissolve the powder, then 6.1 mg of c(RGDfK) was added and mixed together, and finally *N, N*-Diisopropylethylamine was added. The solution was stirred at room temperature for 48 h. Dithiothreitol (DTT) was then added to the reaction mixture and stirred for additional 2 h to reduce the disulfide and obtain a free thiol at the end of the PEG-RGD polymer. The resultant powder was harvested through precipitation in dry diethyl ether.

Unconjugated RGD was removed by a size exclusion NAP-5 Column (GE Healthcare, UK) and the purified HS-PEG-RGD was confirmed by HPLC. PEGylation using HS-PEG-RGD to AuNPs at different molar ratios is carried out the same as for HS-PEG-COOH. After centrifugation twice, the final AuNP pellets were re-suspended in 0.5 mL Milli-Q H_2O to concentration the solution 20 times.

Cell Culture and Preparation: The U-87 MG brain cancer (glioblastoma), MCF-7 breast cancer, and RAW 264.7 macrophage cell lines were maintained as adherent cultures and grown as monolayers in a humidified incubator (95% air; 5% CO_2) at 37 °C in a Petri dish containing medium supplemented with antibiotic-antimycotic and 10% heat-inactivated fetal bovine serum (FBS). To test targeting efficiency of AuNPs with different PEG-RGD density, cells were seeded into 6-well plates and left overnight. Cell numbers (3.0×10^5 U-87 MG/well, 7.3×10^5 MCF-7/well, $2.7x10^5$ RAW 264.7/well) were counted using a Countess automated cell counter (Invitrogen, USA). After exposure to AuNPs (5 nM) formulated with different ratios of PEG-RGD in complete media supplied with 10% FBS at 37 °C for 4 h (U-87 MG, MCF-7) or 8 h (RAW 264.7), cells were washed with PBS twice and digested in aqua regia for 2 h. The aqua regia solutions were transferred to 15 mL centrifuge tubes and the final volumes were adjusted using Milli-Q water. The final gold content was measured using inductively coupled plasma optical emission spectrometry (ICP-OES). To test non-specific uptake of double-charged AuNPs with HS-PEG-COOH and HS-PEG-NH_2, macrophage cells (2.7×10^5/well) were seeded into 6-well plates overnight and then incubated with 1.0 nM double-charged AuNPs in complete media at 37 °C for 4 h. AuNPs coated with a single type of thiolated PEG (HS-PEG-OCH_3, HS-PEG-COOH, or HS-PEG-NH_2) were used as controls.

4.6. Figures

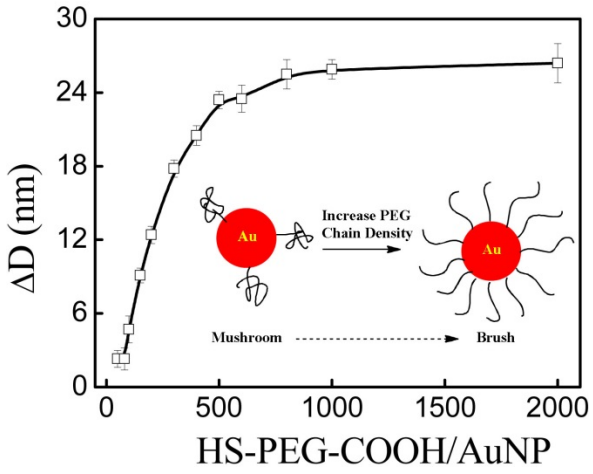

Figure 4.1. Hydrodynamic size change of AuNPs PEGylated with HS-PEG-COOH at all molar ratios before centrifugation, where the insert shows a schematic illustration of the conformation change of PEGylated chains on gold nanoparticles from mushroom at lower PEG chain densities to brush at higher PEG chain densities.

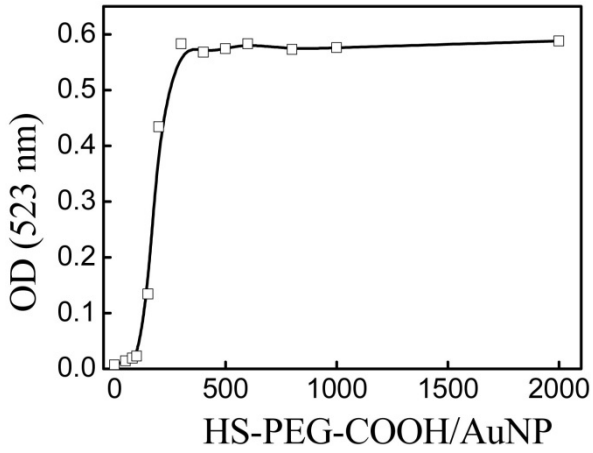

Figure 4.2. Optical density at absorption peak of AuNPs PEGylated with HS-PEG-COOH at all molar ratios after centrifugation.

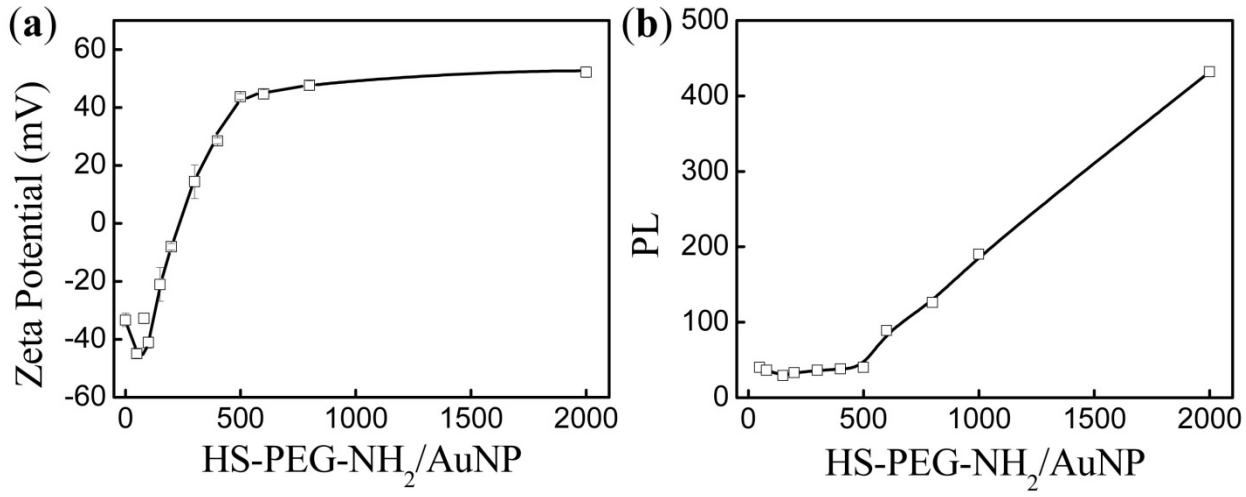

Figure 4.3. (a) Zeta potential before centrifugation of AuNPs PEGylated with HS-PEG-NH_2 at all molar ratios and (b) fluorescence intensity at 480 nm, via fluorescamine-based assay, of the corresponding supernatants after centrifugation.

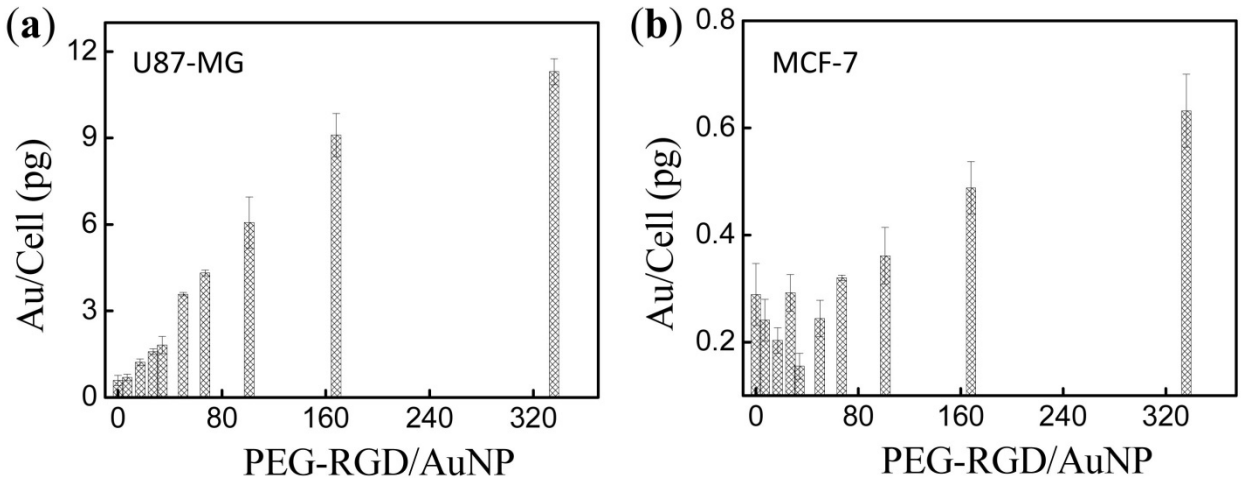

Figure 4.4. Cellular uptake of AuNPs PEGylated with different PEG-RGD densities on the AuNP surface in U-87 MG (a) and MCF-7 (b) cells.

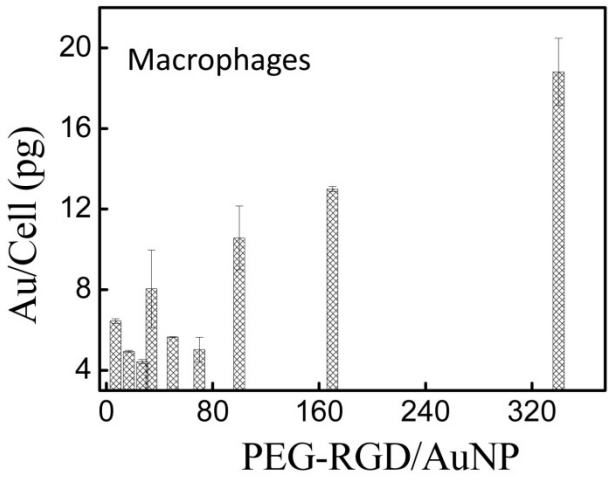

Figure 4.5. Macrophage cell uptake of AuNPs PEGylated with different PEG-RGD densities on the AuNP surfaces.

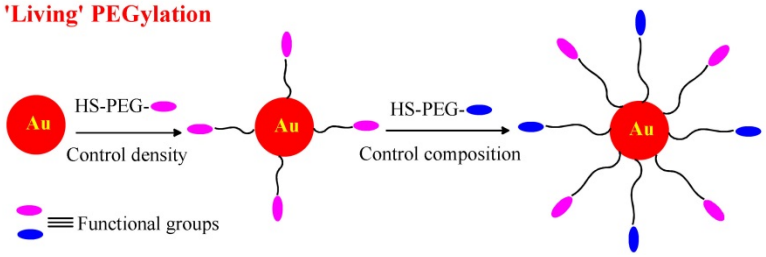

Scheme 4.1. Schematic illustration of 'living' PEGylation with different functional PEG chains and controllable PEG chain density.

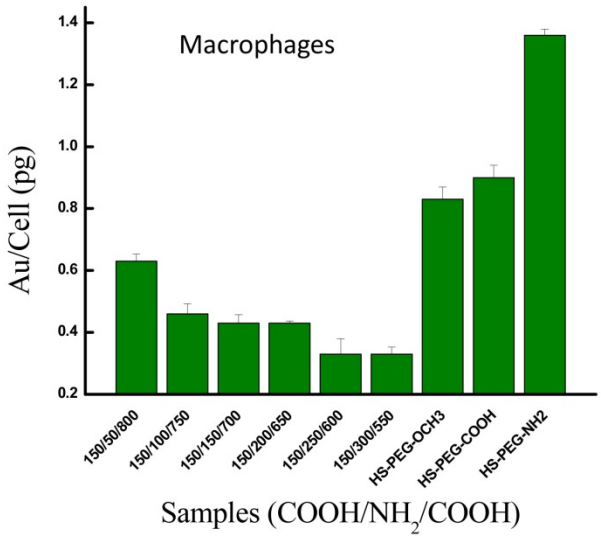

Figure 4.6. Macrophage cell non-specific uptake of AuNPs decorated with PEG-R in single (control) or successive (double-charged) conjugations.

4.7 Supplemental Figures

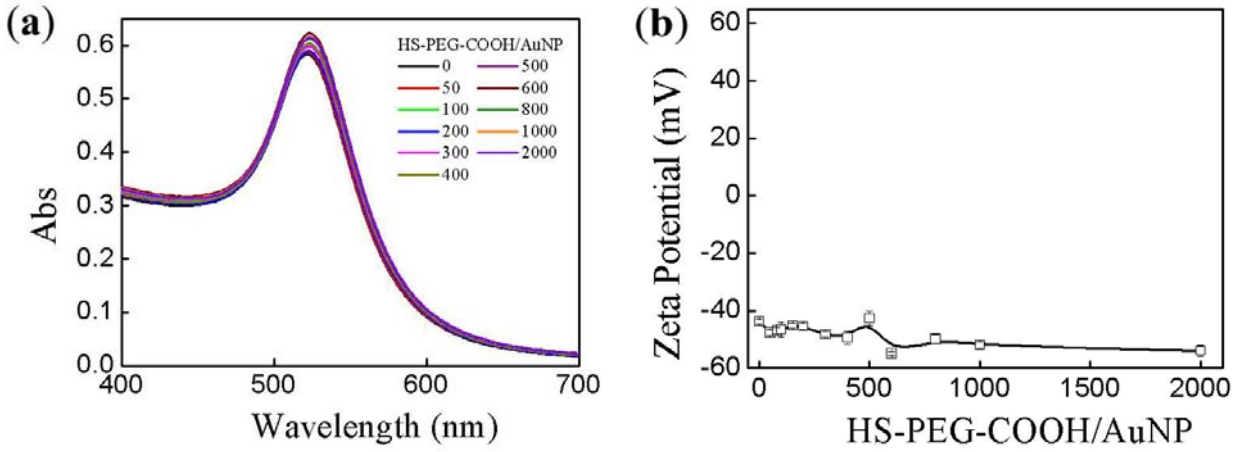

Figure 4.S1. Absorption spectra (a) and zeta potential (b) versus HS-PEG-COOH/AuNP molar ratios, before centrifugation.

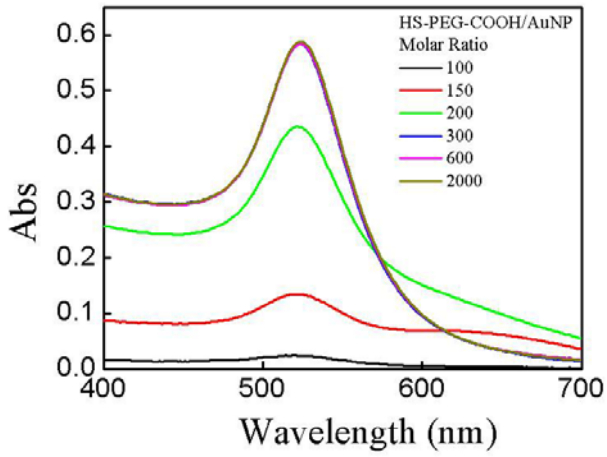

Figure 4.S2. Absorption spectra at typical molar ratios of AuNPs PEGylated with HS-PEG-COOH, after centrifugation.

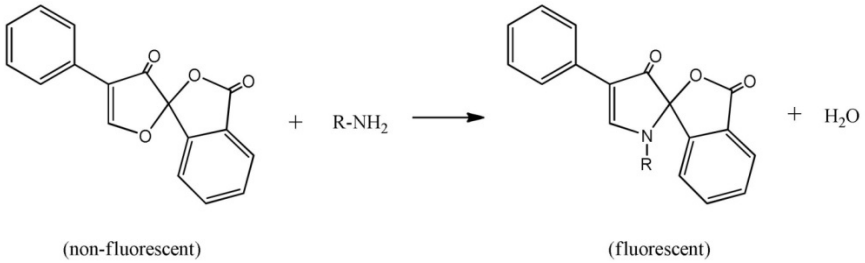

Scheme 4.S1. Scheme of the reaction between fluorescamine and a primary amine that generates a fluorescent product.

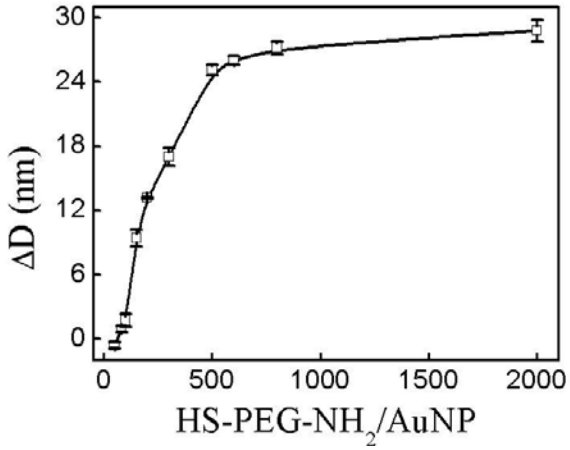

Figure 4.S3. Hydrodynamic size change of AuNPs PEGylated with HS-PEG-NH_2 at all molar ratios, before centrifugation.

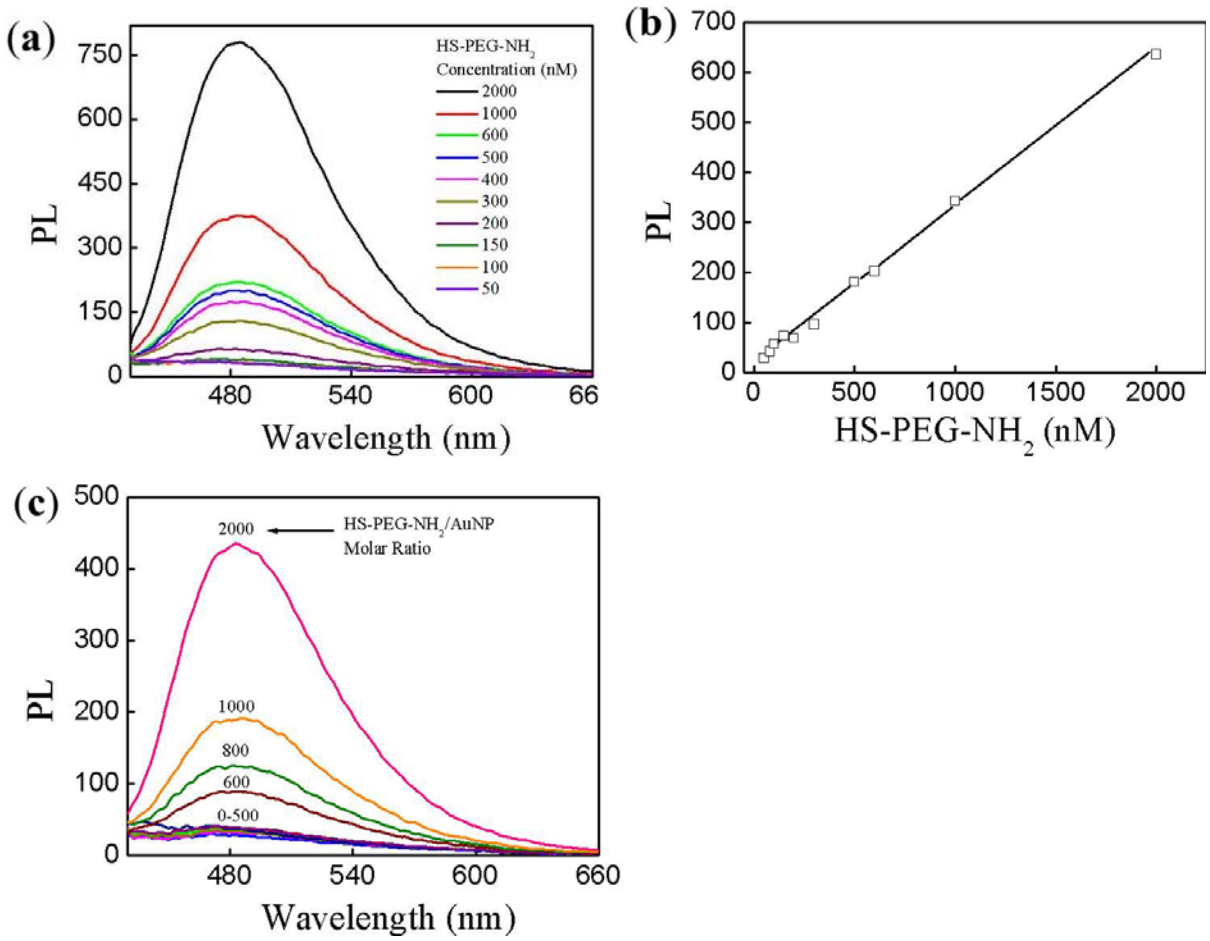

Figure 4.S4. Fluorescence spectra of the HS-PEG-NH_2 calibrating solutions (a) and the plot of corresponding fluorescence intensity at 480 nm (b). Fluorescence spectra of the supernatants containing free HS-PEG-NH_2 after mixing with AuNP at different molar ratios followed by centrifugation (c).

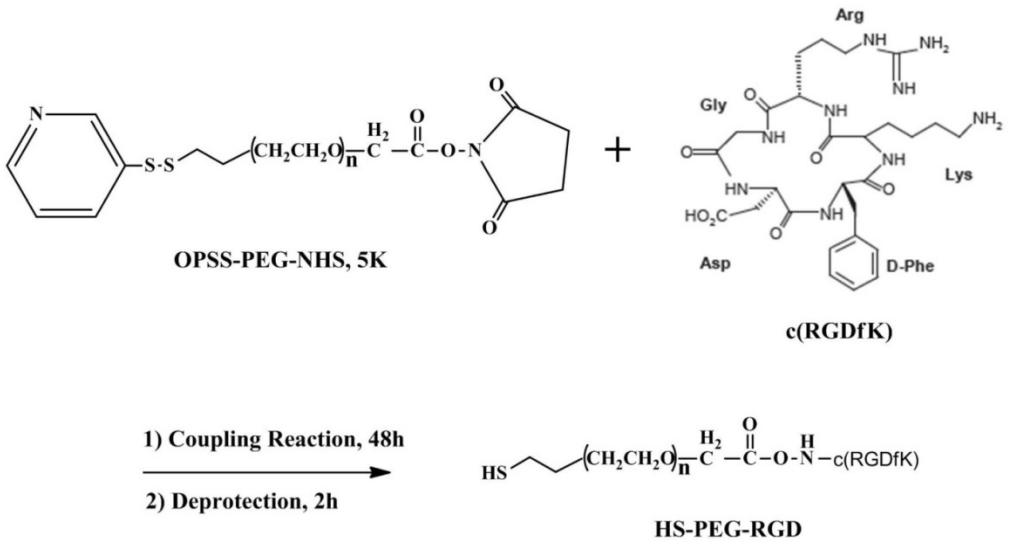

Scheme 4.S2. Synthesis of HS-PEG-RGD.

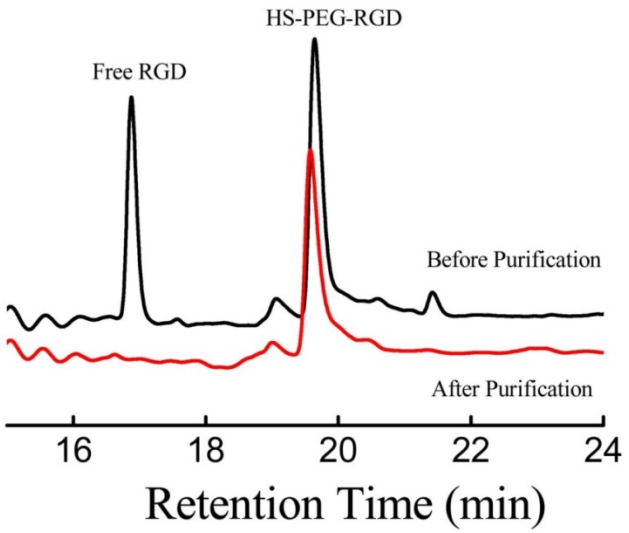

Figure 4.S5. HPLC profile of synthesized HS-PEG-RGD before and after purification.

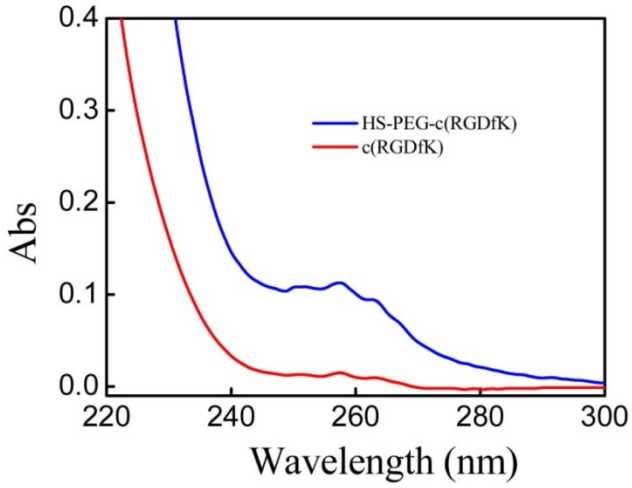

Figure 4.S6. Optical spectra of HS-PEG-RGD and RGD.

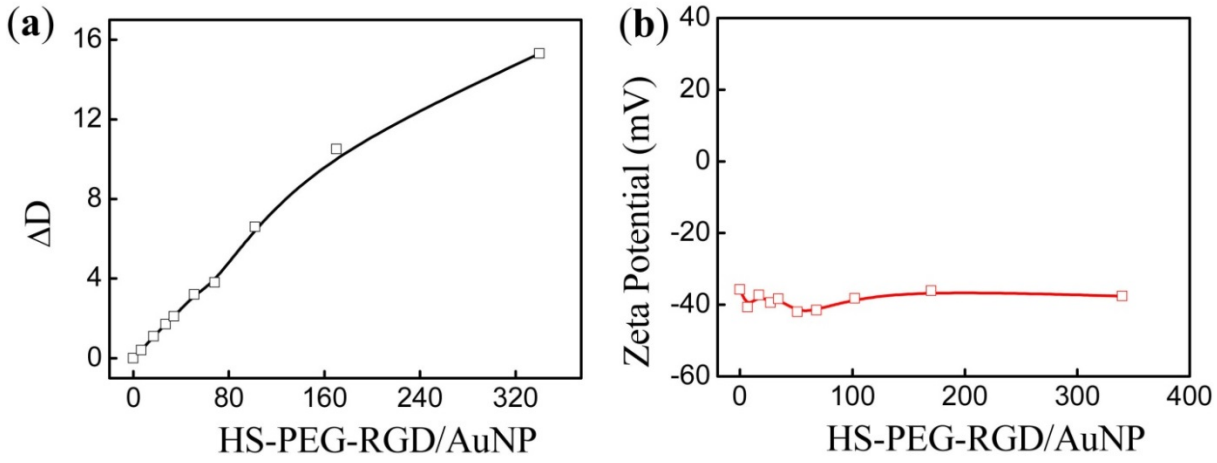

Figure 4.S7. (a) Hydrodynamic size change and (b) zeta potential of AuNPs PEGylated with HS-PEG-RGD at different molar ratios, before centrifugation.

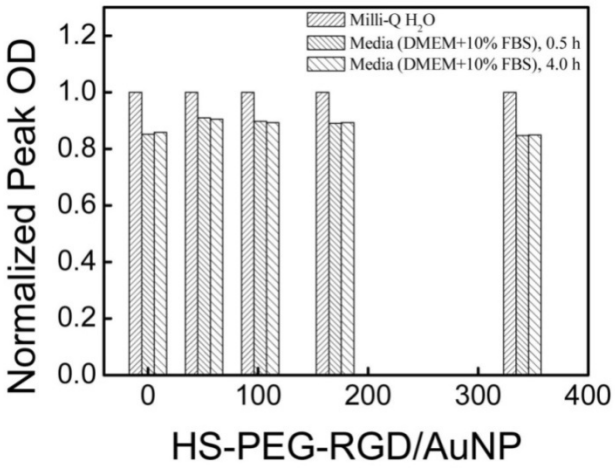

Figure 4.S8. Stability of AuNPs PEGylated with HS-PEG-RGD at typical molar ratios in DMEM media plus 10% FBS.

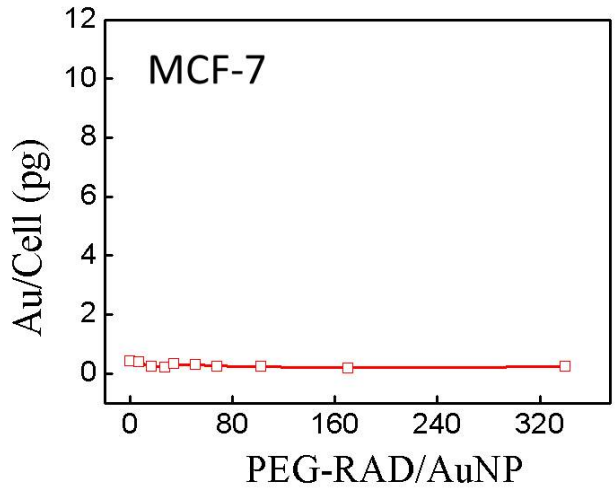

Figure 4.S9. MCF-7 cell non-specific uptake of AuNPs decorated with PEG-RAD (control) at different surface densities.

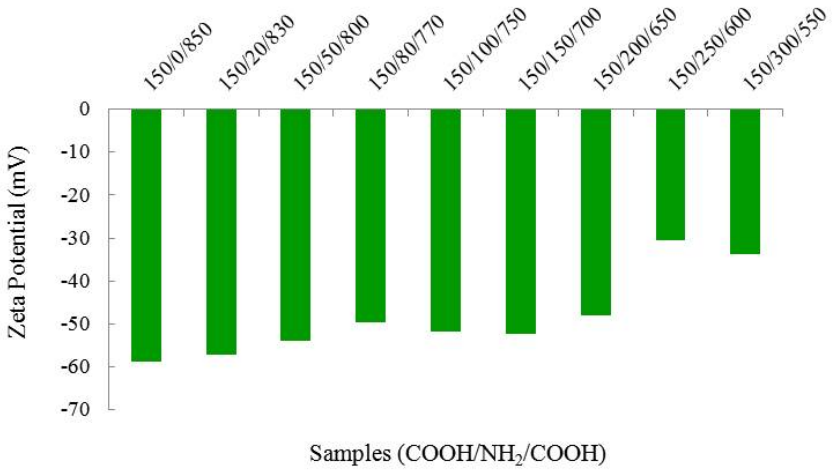

Figure 4.S10. Zeta potential of double-charged AuNPs sequentially PEGylated three times (COOH/NH_2/COOH), with increasing HS-PEG-NH_2/AuNP molar ratios.

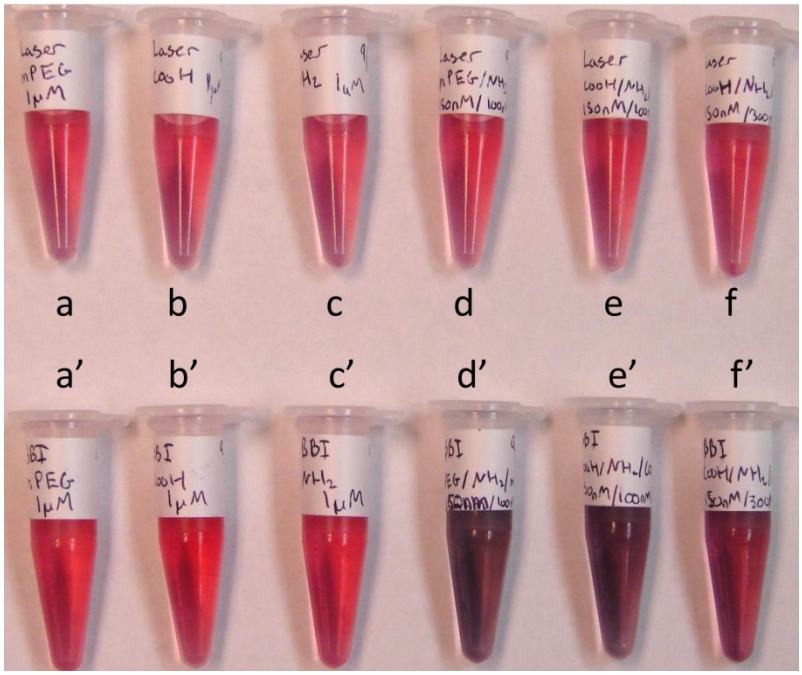

Figure 4.S11. Photograph of laser-generated (top panel) and chemically-made AuNPs (bottom panel) after PEGylation with 1 μM (large excess) of HS-PEG-OCH_3 (a, a'), HS-PEG-COOH (b, b'), and HS-PEG-NH_2 (c, c') (both laser- and chemically-made AuNPs are stable); 150 nM of HS-PEG-OCH_3 then 100 nM of HS-PEG-NH_2 (d, d'); 150 nM of HS-PEG-COOH then 100 nM of HS-PEG-NH_2 (e, e'); 150 nM of HS-PEG-COOH then 300 nM of HS-PEG-NH_2 (f, f') (laser-made AuNPs are stable but chemically-made AuNPs are not).

4.8 Acknowledgements

Hongwei Chen and Hayley Paholak contributed equally to this work, which in its original form was published in *Nanotechnology* (Vol 24, Issue 35) in 2013. Others authors who contributed to this work include Masayuki Ito[2], Kanokwan Sansanaphongpricha[1], Wei Qian[2], Yong Che[2], and Duxin Sun[1]. This work was supported by National Institutes of Health grants RO1CA120023 (D. S.) and a collaborative grant from IMRA America, Inc.

[1]Pharmaceutical Sciences Department, University of Michigan
[2]IMRA America, Inc., Ann Arbor, Michigan

4.9 References

1. Phillips, M.A., M.L. Gran, and N.A. Peppas, *Targeted Nanodelivery of Drugs and Diagnostics.* Nano Today, 2010. **5**(2): p. 143-159.

2. de la Zerda, A., et al., *Family of enhanced photoacoustic imaging agents for high-sensitivity and multiplexing studies in living mice.* Acs Nano, 2012. **6**(6): p. 4694-701.

3. Mickler, F.M., et al., *Tuning nanoparticle uptake: live-cell imaging reveals two distinct endocytosis mechanisms mediated by natural and artificial EGFR targeting ligand.* Nano Lett, 2012. **12**(7): p. 3417-23.

4. Porta, F., et al., *Folic acid-modified mesoporous silica nanoparticles for cellular and nuclear targeted drug delivery.* Adv Healthc Mater, 2013. **2**(2): p. 281-6.

5. Yue, J., et al., *Transferrin-conjugated micelles: enhanced accumulation and antitumor effect for transferrin-receptor-overexpressing cancer models.* Mol Pharm, 2012. **9**(7): p. 1919-31.

6. Yang, L., et al., *Single chain epidermal growth factor receptor antibody conjugated nanoparticles for in vivo tumor targeting and imaging.* Small, 2009. **5**(2): p. 235-43.

7. Elias, D.R., et al., *Effect of ligand density, receptor density, and nanoparticle size on cell targeting.* Nanomedicine, 2013. **9**(2): p. 194-201.

8. Nie, S., *Understanding and overcoming major barriers in cancer nanomedicine.* Nanomedicine (Lond), 2010. **5**(4): p. 523-8.

9. Giljohann, D.A., et al., *Gold Nanoparticles for Biology and Medicine.* Angewandte Chemie-International Edition, 2010. **49**(19): p. 3280-3294.

10. Doane, T.L. and C. Burda, *The unique role of nanoparticles in nanomedicine: imaging, drug delivery and therapy.* Chemical Society Reviews, 2012. **41**(7): p. 2885-2911.

11. Dykman, L. and N. Khlebtsov, *Gold nanoparticles in biomedical applications: recent advances and perspectives.* Chemical Society Reviews, 2012. **41**(6): p. 2256-2282.

12. Daniel, M.C. and D. Astruc, *Gold nanoparticles: Assembly, supramolecular chemistry, quantum-size-related properties, and applications toward biology, catalysis, and nanotechnology.* Chemical Reviews, 2004. **104**(1): p. 293-346.

13. Huang, X., et al., *Cancer cell imaging and photothermal therapy in the near-infrared region by using gold nanorods.* Journal of the American Chemical Society, 2006. **128**(6): p. 2115-20.

14. Klein, S., et al., *Quantitative visualization of colloidal and intracellular gold nanoparticles by confocal microscopy.* Journal of Biomedical Optics, 2010. **15**(3).

15. Leduc, C., et al., *Direct Investigation of Intracellular Presence of Gold Nanoparticles via Photothermal Heterodyne Imaging.* Acs Nano, 2011. **5**(4): p. 2587-2592.

16. Qian, X.M., et al., *In vivo tumor targeting and spectroscopic detection with surface-enhanced Raman nanoparticle tags.* Nature Biotechnology, 2008. **26**(1): p. 83-90.

17. Xie, W., P.H. Qiu, and C.B. Mao, *Bio-imaging, detection and analysis by using nanostructures as SERS substrates.* Journal of Materials Chemistry, 2011. **21**(14): p. 5190-5202.

18. Rand, D., et al., *Nanomaterials for X-ray Imaging: Gold Nanoparticle Enhancement of X-ray Scatter Imaging of Hepatocellular Carcinoma.* Nano Letters, 2011. **11**(7): p. 2678-2683.

19. Hirsch, L.R., et al., *Nanoshell-mediated near-infrared thermal therapy of tumors under magnetic resonance guidance.* Proceedings of the National Academy of Sciences of the United States of America, 2003. **100**(23): p. 13549-13554.

20. von Maltzahn, G., et al., *Nanoparticles that communicate in vivo to amplify tumour targeting.* Nature Materials, 2011. **10**(7): p. 545-552.

21. Dong, W.J., et al., *Facile Synthesis of Monodisperse Superparamagnetic Fe3O4 Core@hybrid@Au Shell Nanocomposite for Bimodal Imaging and Photothermal Therapy.* Advanced Materials, 2011. **23**(45): p. 5392-+.

22. Park, K., et al., *New Generation of Multifunctional Nanoparticles for Cancer Imaging and Therapy.* Advanced Functional Materials, 2009. **19**(10): p. 1553-1566.

23. Minelli, C., S.B. Lowe, and M.M. Stevens, *Engineering Nanocomposite Materials for Cancer Therapy.* Small, 2010. **6**(21): p. 2336-2357.

24. Wang, F., et al., *Doxorubicin-Tethered Responsive Gold Nanoparticles Facilitate Intracellular Drug Delivery for Overcoming Multidrug Resistance in Cancer Cells.* Acs Nano, 2011. **5**(5): p. 3679-3692.

25. Choi, C.H.J., et al., *Mechanism of active targeting in solid tumors with transferrin-containing gold nanoparticles.* Proceedings of the National Academy of Sciences of the United States of America, 2010. **107**(3): p. 1235-1240.

26. Qian, W., et al., *Highly Efficient and Controllable PEGylation of Gold Nanoparticles Prepared by Femtosecond Laser Ablation in Water.* Journal of Physical Chemistry C, 2011. **115**(47): p. 23293-23298.

27. Xia, X.H., et al., *Quantifying the Coverage Density of Poly(ethylene glycol) Chains on the Surface of Gold Nanostructures.* Acs Nano, 2012. **6**(1): p. 512-522.

28. Nagasaki, Y., *Construction of a densely poly(ethylene glycol)-chain-tethered surface and its performance.* Polymer Journal, 2011. **43**(12): p. 949-958.

29. Thierry, B. and H.J. Griesser, *Dense PEG layers for efficient immunotargeting of nanoparticles to cancer cells.* Journal of Materials Chemistry, 2012. **22**(18): p. 8810-8819.

30. Walkey, C.D., et al., *Nanoparticle Size and Surface Chemistry Determine Serum Protein Adsorption and Macrophage Uptake.* Journal of the American Chemical Society, 2012. **134**(4): p. 2139-2147.

31. Braunecker, W.A. and K. Matyjaszewski, *Controlled/living radical polymerization: Features, developments, and perspectives.* Progress in Polymer Science, 2007. **32**(1): p. 93-146.

32. Petersen, S., et al., *Penetratin-Conjugated Gold Nanoparticles - Design of Cell-Penetrating Nanomarkers by Femtosecond Laser Ablation.* Journal of Physical Chemistry C, 2011. **115**(12): p. 5152-5159.

33. Zeng, H.B., et al., *Nanomaterials via Laser Ablation/Irradiation in Liquid: A Review.* Advanced Functional Materials, 2012. **22**(7): p. 1333-1353.

34. Huang, X.H., et al., *A Reexamination of Active and Passive Tumor Targeting by Using Rod-Shaped Gold Nanocrystals and Covalently Conjugated Peptide Ligands.* Acs Nano, 2010. **4**(10): p. 5887-5896.

35. Liu, X.O., et al., *Extinction coefficient of gold nanoparticles with different sizes and different capping ligands.* Colloids and Surfaces B-Biointerfaces, 2007. **58**(1): p. 3-7.

36. Kawaguchi, S., et al., *Aqueous solution properties of oligo- and poly(ethylene oxide) by static light scattering and intrinsic viscosity.* Polymer, 1997. **38**(12): p. 2885-2891.

37. Sylvestre, J.P., et al., *Surface chemistry of gold nanoparticles produced by laser ablation in aqueous media.* Journal of Physical Chemistry B, 2004. **108**(43): p. 16864-16869.

38. Udenfrie.S, et al., *Fluorescamine - Reagent for Assay of Amino-Acids, Peptides, Proteins, and Primary Amines in Picomole Range.* Science, 1972. **178**(4063): p. 871-&.

39. Gormley, A.J., et al., *Biological evaluation of RGDfK-gold nanorod conjugates for prostate cancer treatment.* J Drug Target, 2011. **19**(10): p. 915-24.

40. Polyak, D., et al., *Development of PEGylated doxorubicin-E-[c(RGDfK)(2)] conjugate for integrin-targeted cancer therapy.* Polymers for Advanced Technologies, 2011. **22**(1): p. 103-113.

41. Chen, H.W., et al., *Reducing non-specific binding and uptake of nanoparticles and improving cell targeting with an antifouling PEO-b-P gamma MPS copolymer coating.* Biomaterials, 2010. **31**(20): p. 5397-5407.

42. Sancey, L., et al., *Clustering and internalization of integrin alphavbeta3 with a tetrameric RGD-synthetic peptide.* Mol Ther, 2009. **17**(5): p. 837-43.

43. Byzova, T.V., et al., *Role of integrin alpha(v)beta3 in vascular biology.* Thromb Haemost, 1998. **80**(5): p. 726-34.

44. Liu, X.S., et al., *Minimizing nonspecific phagocytic uptake of biocompatible gold nanoparticles with mixed charged zwitterionic surface modification.* Journal of Materials Chemistry, 2012. **22**(5): p. 1916-1927.

45. Arvizo, R.R., et al., *Effect of nanoparticle surface charge at the plasma membrane and beyond.* Nano Lett, 2010. **10**(7): p. 2543-8.

46. He, C., et al., *Effects of particle size and surface charge on cellular uptake and biodistribution of polymeric nanoparticles.* Biomaterials, 2010. **31**(13): p. 3657-66.

47. Pillai, P.P., et al., *Controlled pH stability and adjustable cellular uptake of mixed-charge nanoparticles.* J Am Chem Soc, 2013. **135**(17): p. 6392-5.

48. Cho, E.C., et al., *The effects of size, shape, and surface functional group of gold nanostructures on their adsorption and internalization by cells.* Small, 2010. **6**(4): p. 517-22.

49. Frohlich, E., *The role of surface charge in cellular uptake and cytotoxicity of medical nanoparticles.* Int J Nanomedicine, 2012. **7**: p. 5577-91.

50. Murthy, A.K., et al., *Charged gold nanoparticles with essentially zero serum protein adsorption in undiluted fetal bovine serum.* J Am Chem Soc, 2013. **135**(21): p. 7799-802.

51. Holmlin, R.E.C., X.X.; Champan, R.G.; Takayam, S.; Whitesides, G.M., *Zwitterionic SAMs that Resist Nonspecific Adsorption of Protein from Aqueous Buffer.* Langmuir, 2001. **17**.

52. Chen, S., et al., *Strong resistance of a thin crystalline layer of balanced charged groups to protein adsorption.* Langmuir, 2006. **22**(19): p. 8186-91.

53. Zhang, L., et al., *Imaging and cell targeting characteristics of magnetic nanoparticles modified by a functionalizable zwitterionic polymer with adhesive 3,4-dihydroxyphenyl-l-alanine linkages.* Biomaterials, 2010. **31**(25): p. 6582-8.

CHAPTER 5. CORE-SATELLITE NANOPARTICLES WITH CLICKABLE PEPTIDES FOR ACTIVELY TARGETED PHOTOTHERMAL CANCER THERAPY AND MAGNETIC RESONANCE IMAGING

5.1 Abstract

The advent of nanomedicine has brought tremendous potential to push the boundaries of traditional cancer therapies and design specific treatments with enhanced control over delivery and targeting. Photothermal therapy (PTT) to induce localized hyperthermia is one of few nanoparticle-based treatments to enter clinical trials in human cancer patients, but currently relies on passive tumor targeting clinically. Employing actively targeted, theranostic nanoparticles for PTT combines multiple approaches at controlled delivery of localized therapy and may be adapted in the future for metastatic cancer settings, particularly in light of recent reports in animal models that PTT can trigger a cancer-specific immune response. Here we describe a facile, optimal design for actively targeted, theranostic nanocomposites with a core-satellite structure for photothermal therapy and magnetic resonance imaging (MRI). A small, "clickable" targeting peptide facilely synthesized with an N-terminal alkyne separated by two 6-aminohexanoic acid spacers acids enables precise control over attachment to the nanoparticles to prevent steric hindrance and optimize binding with the target receptor. Poly(ethylene glycol)-azide (PEG-N_3)-coated PTT nanocomposites with a highly crystallized iron oxide nanoparticle

(HCIONP) core (17 nm) and ultra-small AuNP satellites (4 nm) results in enhanced stability with highly efficient conjugation of the targeting peptide by azide-alkyne click chemistry, as determined by changes in hydrodynamic size (33.1 to 39.7 nm) and peptide quantification via the Bradford assay. The high stability of the HCIONP-AuNP-PEG-N_3 nanocomposite makes it ideal for controlled conjugation of cysteine-containing peptides which would otherwise attach directly to the AuNP surface. Furthermore, compared to AuNPs often used for PTT, the HCIONP core of the nanocomposite enables purification by magnet if desired and *in vivo* MRI to visualize the tumor tissue before and after treatment. The HCIONP-AuNP nanocomposites with tumor-targeting, clickable peptides for PTT and MRI presented here exemplify controlled delivery of localized therapy to reduce off-target toxicity and consequently increase both patient tolerance and response to cancer treatment.

5.2 Introduction

The wealth of knowledge in the cancer field gained through bioinformatics and rapid technological advances since the advent of the computer sparked a movement toward personalized cancer therapy that will significantly improve patient response and tolerance. Critical to individualized cancer treatment are the ability to identify which mutations and aberrant signaling are driving each patient's cancer and consequently target and deliver specific therapies. For decades non-surgical cancer treatment has been dominated by radiation and chemotherapy, which are generally aimed at rapidly dividing cells and don't offer much specificity. Consequently, it can be difficult to strike a balance between minimizing off-target side effects and maintaining treatment efficacy. A decrease in the dose or frequency may be

achieved by development of targeted therapies either employing an active homing mechanism or passive carrier [1-3]. Resultant improvements in biodistribution and pharmacokinetic (PK) properties (e.g., half life) enhance the amount and proportion of the therapeutic at the target site. The majority of research on targeted therapies that has advanced to use in patients has focused on increasing delivery to cancer cells in general [3-10], yet there remains great potential to develop therapies that hit more specific targets such as organelles within the cells (e.g., nucleus) [11, 12] or a particular subset of cancer cells such as cancer stem cells [13, 14].

Both passively and actively targeted therapeutics have advanced beyond pre-clinical research. Passive targeting relies on physical properties, such as size or surface charge, of the therapeutic formulation that enhance physiological characteristics such as half-life in the bloodstream (i.e., rate of elimination), plasma protein binding, recognition by immune cells, and ability to exploit the enhanced permeability and retention (EPR) effect resulting from the relatively leaky vasculature and poor drainage of the tumor environment [15, 16]. Abraxane (albumin-bound Paclitaxel, Celgene) and Doxil (Doxorubicin encapsulated into polymer-coated liposomes, Johnson & Johnson's Janssen) are commercially available, passively targeted nanoparticle formulations that have improved the therapeutic index of standard chemotherapy drugs [16, 17]. Various approaches have been taken to develop actively targeted therapeutics, in which (part of) the molecule avidly binds to a specific receptor in a homing fashion [16]. Monoclonal antibodies (mAbs) developed through genetic engineering pioneered by Herb Boyer at the University of California, San Francisco led to a medical breakthrough to produce actively targeted biologics such as Herceptin [18, 19], which became part of frontline treatment for women with Her2+ breast cancer. More recently monoclonal antibodies targeting PD-L1 receptors on cancer cells have been developed for cancer immunotherapy to block cancer cell

suppression of the immune cells attempting to destroy them [20-22]. Examples include BMS936559 (Brystol-Myers Squibb) and MPDL3280A (Genentech) tested in clinical trials for multiple cancers including melanoma and non-small cell lung cancer [23].Antibody-drug conjugates (ADCs) are another approach to develop commercially producible, actively targeted cancer therapy [24]. Examples include Kadcyla (Genentech), in which Herceptin is conjugated to a taxane, approved for metastatic Her2+ breast cancer [25]and Adcetris (Seattle Genetics), composed of a CD30-targeting mAb linked to a microtubule-disrupting compound, approved for Hodgkin lymphoma and systemic anaplastic large cell lymphoma [26].Peptide-based therapies have also been investigated in clinical trials, such as Merck KGaA's Cilengitide [27, 28]. An integrin inhibitor containing the RGD-targeting peptide motif, it is believed to affect both tumor cell growth and formation of new blood vessels that supply the tumor (angiogenesis). Another example in clinical trials is AN-152, a peptide analog of luteinizing hormone-releasing hormone (LHRH) that is bound to Doxorubicin, for targeted prostate cancer therapy [29]. Similarly, the peptide Cetrorelix became the first clinically approved LHRH antagonist, and has been indicated for both prostate and breast cancer treatment [28].

While nanoparticles offer tremendous untapped potential for controlled delivery of targeted cancer therapies, few nanoparticle therapies beyond Abraxane and Doxil have advanced to clinical settings. One that has is Aurimune (CytImmune), which entered Phase I clinical trials in 2006 for advanced or metastatic solid organ cancers [30]. It relies on passive targeting from precisely sized, polymer-coated gold nanoparticles (AuNPs) to deliver tumor necrosis factor (TNF) to help normalize tumor blood flow for enhanced penetration of chemotherapy [31]. Another is AuroLase (Nanospectra Biosciences), polymer-coated gold nanoshells that kill cancer cells through thermal ablation [32]. The nanoshells accumulate in the tumor tissue through

passive targeting, which results in localized destruction as laser light is applied and efficiently converted into heat by the nanoshells (i.e., photothermal therapy). More sophisticated nanoparticle formulations have been designed and tested in the laboratory setting to enhance control over targeted delivery of therapeutic agents, such as those designed for pH-sensitive intracellular drug release in acidic lysosomes or enzyme-mediated release [33-39]. Nanoparticles may not only serve as a platform for targeted drug delivery but also diagnostic tumor imaging, for which a few iron oxide-based nanoparticles, such as Feridex (Berlex Laboratories), have already been approved for use in humans [17].

Nanoparticle-mediated photothermal therapy such as AuroLase provides additional control beyond tumor targeting of agents injected into the patient, since the inert gold nanoshells will only be activated under locally applied laser light. Active targeting of such heat-mediating nanoparticles may reduce the intravenous dose required to achieve a similar intratumoral nanoparticle concentration and potentially the cost of treatment. However, many factors must be taken into account when considering an optimized actively targeted nanoparticle formulation. In terms of the targeting ligand, antibodies are possible to commercially produce and have high binding affinities for their target receptor; however, production and purification is expensive and their relatively large size limits the potential loading capacity of a therapeutic drug onto the nanoparticle surface [40]. A design to maximize both targeting efficiency and potency of drug-loaded nanoparticles would be ideal. High affinity peptides derived from the binding region of an antibody are cheaper and simpler to produce and purify, would allow more room on the nanoparticle surface for attachment of a drug, and may be better suited to benefit from the multivalent effect [40, 41]. Regarding attachment to the nanoparticle surface, peptides and antibodies are generally conjugated using chemically-reactive groups (NH_2, COOH, SH) on the

side chains of their amino acid building blocks [42]; however, this approach may affect the binding of the ligand to target receptors. A simple modification of the ligand in a region outside of the primary binding site to allow a specific conjugation reaction would be ideal for maximizing binding affinity. Similarly, a balance must be struck in selecting chemistry approaches to control the addition of the targeting ligand while maintaining stability of a colloidal nanoparticle.

Here we propose an optimized design for actively targeted, theranostic nanoparticles for localized, externally controlled photothermal therapy (PTT) and tumor imaging capabilities. Nanocomposites composed of a highly crystallized iron oxide nanoparticle (HCIONP) core and gold nanoparticle (AuNP) satellites facilely synthesized in our lab have been shown to be efficient PTT mediators capable of magnetic resonance imaging (MRI) in an *in vivo* breast cancer model, and can be simply modified through thiol-gold linkage [43]. These core-satellite nanocomposites will be modified with heterobifunctional polyethylene glycol, thiol-PEG-azide (HS-PEG-N_3), to precisely control conjugation of a targeting peptide through click chemistry using a peptide bearing an N-terminal alkyne separated by two spacers. This design avoids using amino acid side chains for conjugation of the peptide, preventing possible interference of its interaction with the target receptor. The high stability of the HCIONP-AuNP nanocomposite makes it ideal for controlled conjugation of cysteine-containing peptides with thiol groups, which requires the PEG-azide to be attached to the nanoparticle prior to click chemistry with the peptide to prevent the peptide from attaching to the gold nanoparticle surface directly through its cysteine side chains. Furthermore, while purification by centrifugation after modification of the nanoparticle surface can affect nanoparticle stability, the HCIONP core of the nanocomposite

enables more gentle purification by magnet. Compared to AuNPs often used for PTT, the HCIONP core also allows *in vivo* MRI to visualize the tumor tissue before and after treatment.

5.3 Results and Discussion

Decades of cancer treatment dominated by surgery, radiation, and chemotherapy has resulted in many patients not only struggling to cope with the knowledge of carrying a potentially fatal disease but the detrimental side effects they face with non-specific treatments. The ability to develop and effectively deliver personalized, targeted medicine may increase patient tolerance and response to treatment as well as avoid future complications from stresses put on the body (e.g., heart) directly caused by treatment (e.g., Doxorubicin). Employing actively targeted nanoparticles for photothermal therapy combines multiple approaches at delivering localized cancer therapy with reduced off-target toxicity. The nanoparticle size facilitates passive targeting of therapy to the tumor site, where the ligand on the nanoparticle surface will direct it to the cells of interest. Using nanoparticles composed of inert materials, such as gold, that are externally activated to produce heat localizes damage to cancer cells despite not all of the nanoparticles reaching the tumor site.

Due to simple, cost effective production and small size relative to a monoclonal antibody, a peptide was considered the ideal targeting ligand to attach to the surface of the nanoparticle for photothermal therapy and selected for our study. The 9-mer model peptide selected has an amino acid sequence of Asp-Arg-Phe-Cys-Asp-Arg-Phe-Pro-Phe (DRFCDRFPF), giving it side chains with functional groups that are commonly used for chemical attachment to the surface of nanoparticles: the carboxylic acid (COOH) groups in the aspartic acid (D) residues, and the thiol

(SH) group in the cysteine (C) residue [42, 44]. This sequence was derived from the nine amino acids deemed critical for the interaction of the Jagged1 ligand with its Notch receptor over-expressed on several types of cancer cells including breast cancer [45, 46]. However, using functional groups within the side chains of any critical amino acid to conjugate a peptide to therapeutic nanoparticles may interfere with binding affinity for the target receptor.

Here we propose to use click chemistry for a specific chemical conjugation of the targeting peptide to the surface of the nanoparticle for photothermal therapy (Scheme 5.1). "Click" chemistry was first described by Sharpless and coworkers seeking simple, high yield, stereo-specific reactions that create only "inoffensive" by-products [47]. Being bio-orthogonal reactions, the functional groups of both the reactants and products will not interact with naturally occurring biomolecules [48, 49]. Azide-alkyne cycloaddition (Scheme 5.2) has become one of the most used click chemistry reactions. Like many click chemistry reactions, it can be performed at room temperature in water. A linear alkyne functional group will react highly efficiently with an azide group in the presence of a copper catalyst to form a triazole product. If desired, copper-less azide-alkyne cycloaddition may be performed using a ring-strained alkyne [48]. As a modification to previously described "clickable" peptides [50, 51], we propose the N-terminal addition of two 6-aminohexanoic acid (Ahx) spacers between the targeting peptide's amino acids to minimize steric hindrance when attached to the nanocomposite and optimize the ligand-target interaction. Furthermore, both the spacers and the 4-pentynoic acid contain the necessary functional groups to continue FMOC chemistry used during peptide synthesis to add each amino acid to the chain. Following manual synthesis of the 9-mer-alkyne shown in Scheme 5.3, the peptide was purified by reverse phase high performance liquid chromatography (RP-

HPLC). The analytical run of the purified product is shown in Figure 5.1A and confirmation of the correct mass by electrospray ionization mass spectroscopy in Figure 5.1B.

The gold standard for nanoparticle mediators of photothermal cancer therapy are gold-based nanoparticles, following the works of Mostafa El-Sayed and Jennifer West applying gold nanorods (AuNRs) and developing the silica-core gold nanoshells (AuNSs) that were commercialized to AuroLase therapy [11, 32, 52-55]. These particular gold structures have a peak absorbance of near infrared (NIR) light, which allows for maximal tissue penetration and selective heating of nanoparticles due to the low light absorbance by tissue chromophores at this wavelength [56]. Gold efficiently converts light irradiation into heat by causing oscillations of electrons at the nanoparticle surface, a phenomenon known as surface plasmon resonance [57]. In addition to being biocompatible, an advantage of gold nanoparticles is the ability to facilely modify their surface using thiol functional groups. However, this poses a challenge when the required targeting ligand contains one or more thiol-bearing cysteines if a unique reaction is desired for the chemical conjugation. Normally, AuNPs are coated with the hydrophilic polymer poly(ethylene glycol) (HS-PEG-R) to render them stable in physiological conditions [58, 59], and small targeting molecules like peptides would be attached to the PEG rather than directly to the nanoparticle surface to prevent it being masked by the polymer [58]. If the peptide contains a cysteine, it must be added to the AuNPs after they are coated with PEG rather than simply attaching the thiol-PEG-peptide conjugate. For our study the azide-PEG-coated nanoparticles must remain stable during the attachment of the cysteine-containing targeting peptide by click chemistry and subsequent purification, making the HCIONP-AuNP core-satellite nanocomposite previously reported by our lab ideal.

Commercial gold nanoparticles (15 nm) were originally selected for proof-of-concept studies for peptide attachment by click chemistry. The stability of colloidal gold can be tracked through absorbance measurements related to their concentration by the Beer-Lambert Law [60]. The concentration of AuNPs coated with HS-PEG-N_3 was determined before and after click chemistry using their peak absorption at 520 nm (Figure 5.2A). As shown in Figure 5.2B, the AuNP instability is apparent from the dramatic drop in concentration after allowing the copper-catalyzed click chemistry reaction to proceed overnight. Next we sought to test whether PTT-mediating AuNPs stabilized onto HCIONPs, as previously described in our lab [43], would remain stable during peptide addition via click chemistry. Furthermore, the HCIONP core grants the nanocomposites MRI capabilities not possible with commonly used AuNRs and AuNSs for photothermal therapy and enables purification of the nanoparticles by magnet, a gentler process than centrifugation.

For the initial stability study, HCIONP-AuNP nanocomposites with and without the PEG-N_3 coating were used. HCIONPs (17 nm) for the nanocomposite core were synthesized by thermal decomposition and rendered water soluble by coating with an antifouling polymer, as previously described by our lab [43, 61, 62]. AuNP satellites (~7 nm) were synthesized from chloroauric acid [43]. After overnight mixing of the polymer-coated HCIONPs and the AuNPs to form the nanocomposites, a portion was coated with thiol-PEG-azide before purification by magnet. The stability of the nanocomposites to the click chemistry reagents (copper sulfate, sodium ascorbate) was tested using alkyne-5-FAM as a model for the 9-mer-alkyne peptide. As shown in Figure 5.2C, the nanocomposites are most stable when the alkyne and azide groups are reacted in the presence of the click chemistry reagents. Both solutions tested using nanocomposites lacking the PEG-N_3 coating are unstable to click chemistry conditions.

For subsequent studies, the nanocomposites were formulated with ultra-small AuNP satellites (~4 nm) similarly synthesized from chloroauric acid. Previously tested by our lab, these ultra-small PTT-mediating AuNPs no longer express the absorbance peak at 520 nm. The structure and size of the HCIONP-AuNP-PEG-N_3 nanocomposites were viewed by transmission electron microscopy (TEM), as shown in Figure 5.3A. Initial measurements of the hydrodynamic size and zeta potential before addition of the 9-mer-alkyne were taken by dynamic light scattering (Figure 5.3B). The 33.1 nm hydrodynamic size following PEGylation meets our expectations based on the HCIONP and AuNP sizes determined by TEM. The nanocomposite iron and gold concentrations were determined by inductively coupled plasma optical emission spectrometry (ICP-OES) (Figure 5.3C); from this the molar ratio of AuNPs per HCIONP was determined to be 8.0:1, which is consistent with the number of AuNP satellites per HCIONP core according to TEM. The PEG-N_3 concentration for click chemistry was estimated according to the footprint of PEG_{5000} on gold nanoshells [63]. Calculating the surface area of AuNP satellites and assuming roughly half will be freely available for conjugation by HS-PEG-N_3, accounting for the surface area required for attachment to the HCIONP core, the molar ratio of PEG molecules per AuNP satellite was estimated to be 3:1.

Upon initiating the click chemistry reaction of the HCIONP-AuNP-PEG-N_3 nanocomposites and 9-mer-alkyne, initial and final absorption curves were obtained to demonstrate the nanocomposite stability as shown in Figure 5.4A. Successful attachment of the 9-mer-alkyne was confirmed in two ways. Following the click chemistry reaction, the solution was centrifuged to collect the unbound peptide in the supernatant and the nanocomposites were resuspended. First, the nanocomposite hydrodynamic size and zeta potential were determined, as shown in Figure 5.4B. The modest yet significant ($p = 0.05$) size increase from 33.1 to 39.7 nm

following click chemistry suggests the alkyne-peptide was conjugated to the end of the PEG-azide. Given the two positive arginine (R) and two negative aspartic acid (D) residues, a relatively consistent zeta potential before (-30.8 mV) and after (-30.5 mV) click chemistry is to be expected. Second, the Bradford Quick Start assay was chosen to quantify 9-mer-alkyne binding to the nanocomposites. The Coomassie Brilliant Blue dye converts from a cationic form to an anionic form upon binding to proteins through amino acids that are basic (e.g., arginine) and aromatic (e.g., phenylalanine), resulting in a shift from a red to a blue color that is detectable at 595 nm [64]. The unbound peptide collected was quantified using a standard curve of the 9-mer-alkyne generated at limiting peptide dilutions but maintaining a constant concentration of click chemistry reagents equal to that used in the reaction, as shown in Figure 5.4C. The absorbance value of the peptide supernatant after click chemistry was 0.005 above the background (click chemistry reagents without peptide), suggesting a highly efficient reaction in which virtually all of the peptide was conjugated to the nanocomposites.

For follow up studies, it would be optimal to purify the peptide-modified nanocomposites by magnet as a portion could not be resuspended following centrifugation. To test the targeting efficiency of the peptide-modified nanocomposites with cancer cells *in vitro*, ideally a well-characterized targeting peptide should be used in place of our model peptide. One example would be the RGD peptide that targets $\alpha_v\beta_3$ integrin receptors such as those found on U-87 MG glioblastoma cells [7, 58]. Furthermore, while our lab has previously shown the non-targeted HCIONP-AuNP nanocomposites are stable *in vivo*, demonstrating the proportions of Fe and Au are consistent in each tissue to which the nanocomposites distribute, the stability of the peptide-modified nanocomposites should be confirmed in blood.

Collectively our results presented here suggest that development of actively targeted, photothermal-mediating nanocomposites modified with clickable peptides offer many formulation benefits: stable nanoparticles that can be specifically and facilely appended with targeting peptides to promote optimal interactions with the target receptor. Employing nanocomposites that are stable to click chemistry allows controlled addition of cysteine (thiol)-containing peptides to gold-based photothermal mediators. The iron oxide core of the HCIONP-AuNP core-satellite nanocomposite enables purification by magnet if desired as well as MRI diagnostic therapy, for which a few iron oxide-based nanoparticles, such as Feridex and Combidex, have already been used in humans for tumor imaging [17]. Production of targeting peptides is much simpler and cheaper than monoclonal antibodies, which must be produced in bacteria and undergo multiple purification steps. Furthermore, the smaller size of peptides better facilitates drug loading if dual PTT and targeted drug delivery are desired. Nanoparticle-mediated photothermal therapy poses an attractive strategy for targeted cancer therapy in that it is inherently localized by requiring external activation. While its use in clinical trials is currently limited to head and neck cancer and primary and metastatic lung cancer [65, 66], PTT offers tremendous untapped potential for site-specific cancer therapy that has a relatively wide therapeutic index. As heat-mediated cell death isn't pathway specific, PTT could be applied to a variety of cancers including the difficult-to-treat triple negative breast cancer. Targeted nanoparticles capable of *in vivo* imaging, such as those described here, may even be adapted to apply PTT to metastatic sites in the future. Similarly, recent reports that PTT at primary tumor sites triggers an immune response to attack cancer cells at metastatic sites [67-69] has opened doors to developing potentially synergystic therapies combining PTT with the exploding field of cancer immunotherapy.

5.4 Conclusions

Here we demonstrate successful formulation of actively targeted, theranostic nanoparticles for localized, externally controlled photothermal therapy (PTT) and tumor imaging capabilities. First, we facilely synthesize a model clickable peptide with an N-terminal alkyne separated by two 6-aminohexanoic acid spacers acids, designed for precise control over attachment to the nanoparticles to prevent steric hindrance and optimize binding with the target receptor. Next we synthesize and characterize azide-coated PTT nanocomposites with a HCIONP core (17 nm) and ultra-small AuNP satellites (4 nm), and demonstrate their enhanced stability to azide-alkyne click chemistry through absorption measurements. Highly efficient peptide conjugation is confirmed by measuring changes in hydrodynamic size (33.1 to 39.7 nm) and quantifying unbound peptide via the Bradford assay. The high stability of the IONP-AuNP-PEG-N_3 nanocomposite makes it ideal for controlled conjugation of cysteine-containing peptides with thiol groups, which would otherwise attach directly to the AuNP surface if not previously PEGylated. Furthermore, compared to AuNPs often used for PTT, the HCIONP core of the nanocomposite enables purification by magnet if desired and *in vivo* MRI to visualize the tumor tissue before and after treatment. Employing actively targeted, facilely synthesized composite nanoparticles for photothermal therapy, as described here, combines multiple approaches for delivering localized therapy with reduced off-target toxicity to increase both patient tolerance and response to cancer treatment.

5.5 Materials and Methods

Synthesis of alkyne-peptide: The model targeting peptide was produced manually via FMOC solid phase synthesis using chlorotrityl resin. Following addition of the nine amino acids (DRFCDRFPF) to the resin, two 6-aminohexanoic acid spacers and 4-pentynoic acid were added at the N-terminus before cleavage from the resin. Purification of the peptide, designated 9-mer-alkyne, was performed via reverse phase high performance liquid chromatography (RP-HPLC) with a C-18 column (Sunfire, 19 mm × 150 mm, 5 μm), and electrospray ionization mass spectroscopy confirmed the correct mass.

Synthesis of iron oxide-gold core-satellite nanocomposite: Polymer-coated HCIONPs were prepared as previously described by our lab. Briefly, HCIONPs (17 nm diameter) were synthesized in organic solvent by thermal decomposition. They were rendered soluble in aqueous solution after coating with diblock copolymer poly(ethylene oxide)-b-poly(γ-methacryloxypropyl trimethoxysilane)(PEO-b- PγMPS), which is synthesized by reversible addition fragmentation chain transfer (RAFT) polymerization, and purifying by a magnetic separator (Frantz laboratory) at 4 °C. The iron concentration of the resultant solution was determined using o-phenanthroline as previously described.

Ultra-small AuNPs were synthesized from chloroauric acid ($HAuCl_4$, 2.0 mM stock) using sodium sulfide (Na_2S, 1.0 mM stock) as the reducing reagent, which was first prepared and aged in the dark for 48 h before use. Na_2S and $HAuCl_4$ were mixed in the dark at a volume ratio of 3.0/1.75 for 3 h. The HCIONP-AuNP core-satellite nanocomposites were formed in the dark by mixing polymer-coated HCIONPs (1.0 mL of 4.3 mg Fe/mL stock) with AuNPs (50 mL) overnight at 4 °C and subsequently coated with HS-PEG_{5000}-N_3 (NanoCS) overnight in the dark

at 4 °C. Azide-modified nanocomposites were purified by magnet at 4 °C and viewed by transmission electron microscopy (TEM) (JEOL JEM-1400Plus 120 kV). Hydrodynamic size and zeta potential were determined by dynamic light scattering (DLS) on a Zetasizer Nano S90 (Malvern). The iron and gold concentrations were measured by inductively coupled plasmaoptical emission spectrometry (ICP-OES) using yttrium as the internal standard, following dissolution of the nanocomposite in aqua regia (3:1 hydrochloric acid to nitric acid). The PEG-N_3 concentration on the HCIONP-AuNP nanocomposites was calculated using a footprint of 9.6 nm^2 for PEG-5000 [63] and the assumption that half of each AuNP surface could be coated with PEG after binding to a HCIONP core.

Peptide conjugation to nanocomposites by click chemistry: HCIONP-AuNP-PEG-N_3 (25 μM PEG-N_3) were mixed in the dark overnight with the 9-mer-alkyne (50 μM) in the presence of copper sulfate ($CuSO_4$) catalyst (200 μM) and sodium ascorbate (1 mM) reducing agent. Unbound peptide was removed by centrifugation with nanocomposites at 10,000 RPM for 10 min followed by additional centrifugation at 15,000 RPM for 5 min after separating from the nanocomposite pellet. Following both centrifugations, the supernatant was collected and used for quantification of unbound peptide. The resuspended HCIONP-AuNP-PEG-N_3 pellet was analyzed by DLS.

Peptide quantification with Bradford assay: Peptide quantification was performed according to the manufacturer's microassay protocol for the Quick Start Bradford Protein Assay (Bio-Rad), using absorbance measurements from a BioTek microplate reader (Synergy 2). The concentration of unbound peptide concentration in the click chemistry supernatant was

calculated from a standard curve of the 9-mer-alkyne at limiting dilutions but with a constant concentration of click chemistry reagents equal to that used in the click chemistry reaction.

Statistical Analysis: Data are represented as mean ± standard deviation. The significance values of data sets with two groups were calculated by a student's t-test. A $p \leq 0.05$ was considered statistically significant.

5.6 Figures

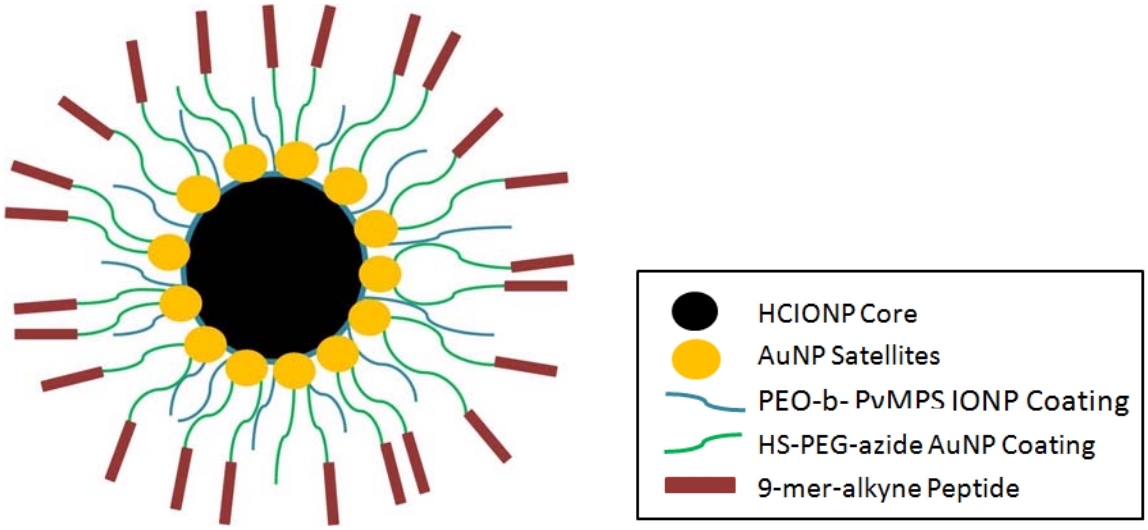

Scheme 5.1. Schematic of HCIONP-AuNP core-satellite nanocomposites with clickable peptides for targeted photothermal therapy

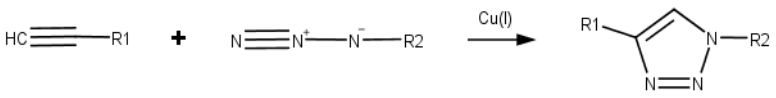

Scheme 5.2. Schematic (MarvinSketch) of copper-catalyzed alkyne-azide cycloaddition (CuAAC) to form a triazole product.

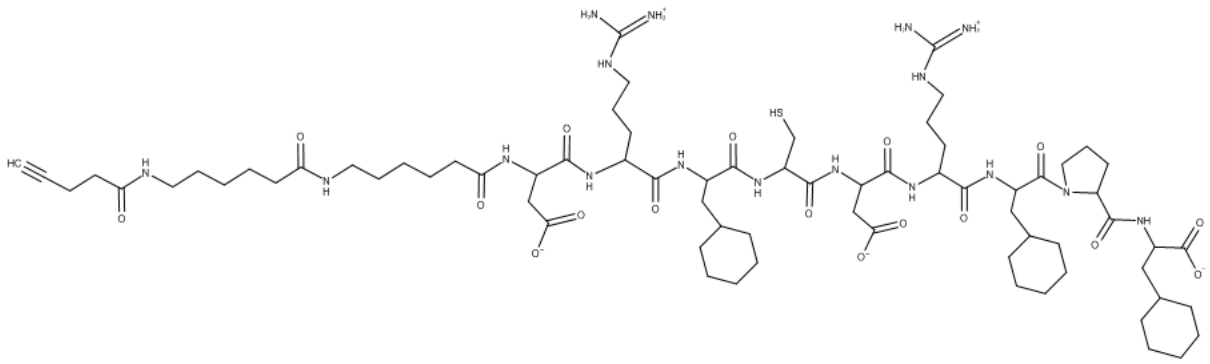

Scheme 5.3. Schematic (MarvinSketch) of 9-mer (DRFCDRFPF) with N-terminal alkyne (4-pentynoic acid) spaced by two 6-aminohexanoic acid linkers.

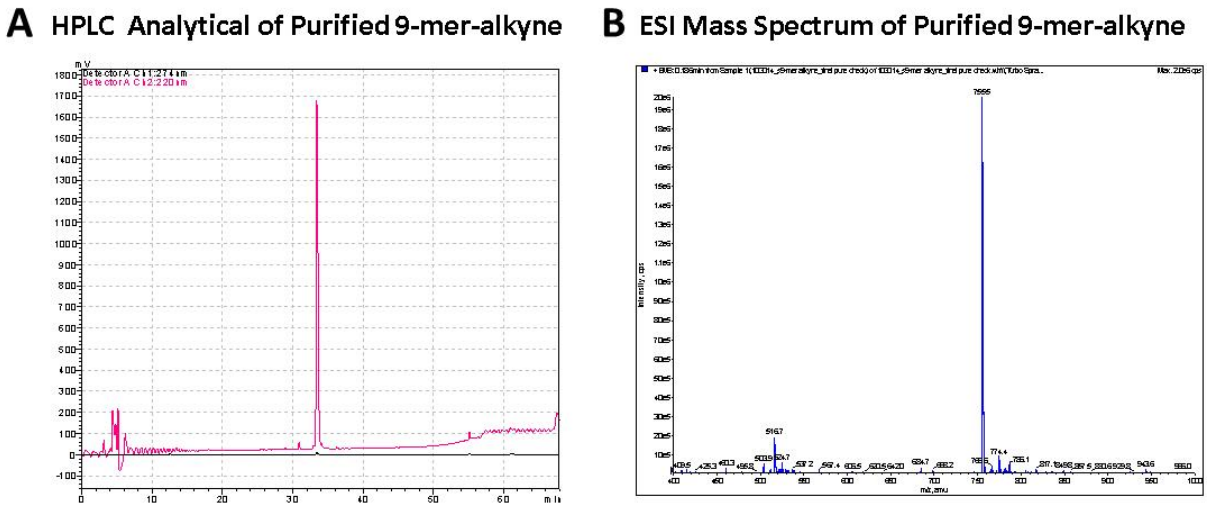

Figure 5.1. (A) Single peak from the analytical run of the purified 9-mer-Ahx-Ahx-Alkyne (MW ~1509 g/mol). (B) Confirmation of the correct mass by electrospray ionization (ESI) mass spectroscopy, revealing the +2 peak at 755.5 m/z.

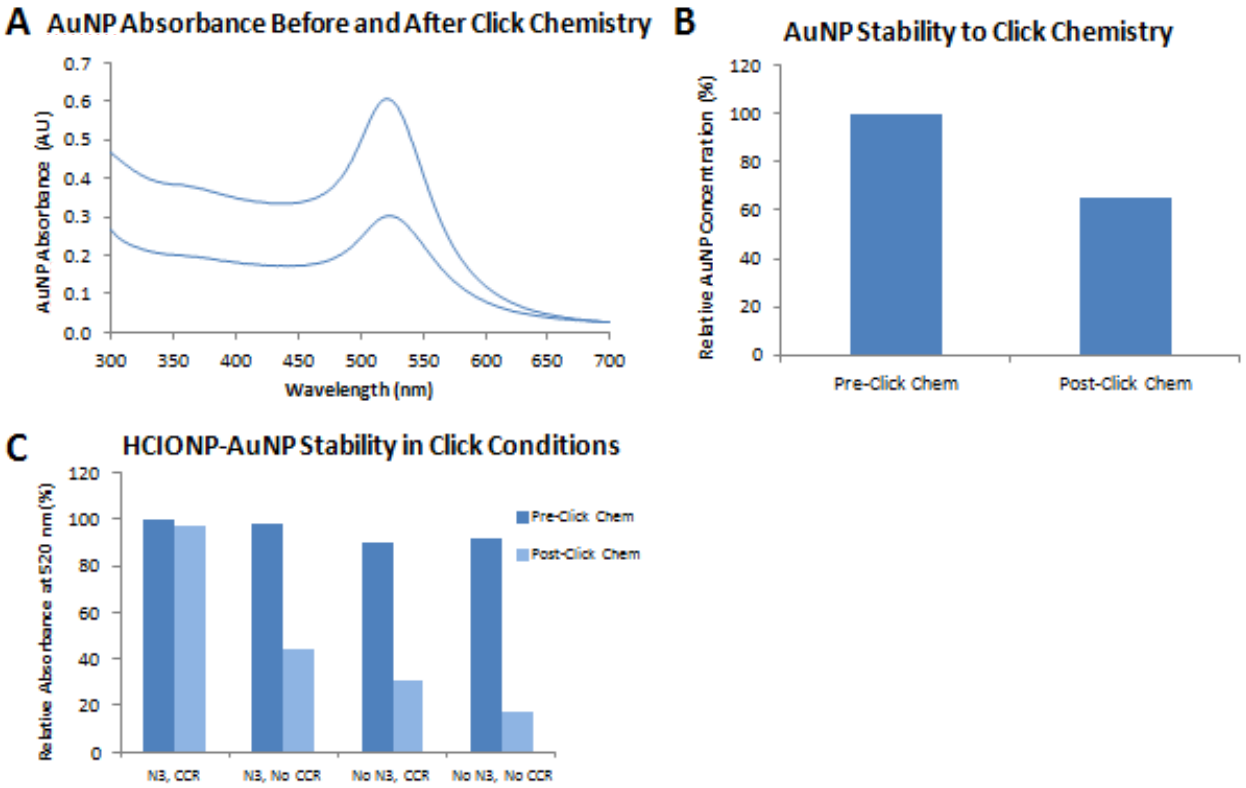

Figure 5.2. (A) Absorbance curves of azide-PEG-coated AuNPs before and after overnight click chemistry reaction with alkyne-peptide. (B) Relative concentration of azide-PEG-coated AuNPs before and after overnight click chemistry reaction with alkyne-peptide. After determining the AuNP concentration from the absorbance using the Beer-Lambert Law, the post-click concentration was adjusted to account for the dilution that occurred when mixing with peptide and click chemistry reagents. (C) Stability of HCIONP-AuNPs, with and without PEG-N_3 coating, to click chemistry reagents (CCR) as determined by relative absorbance shown before and after overnight mixing with alkyne-5-FAM.

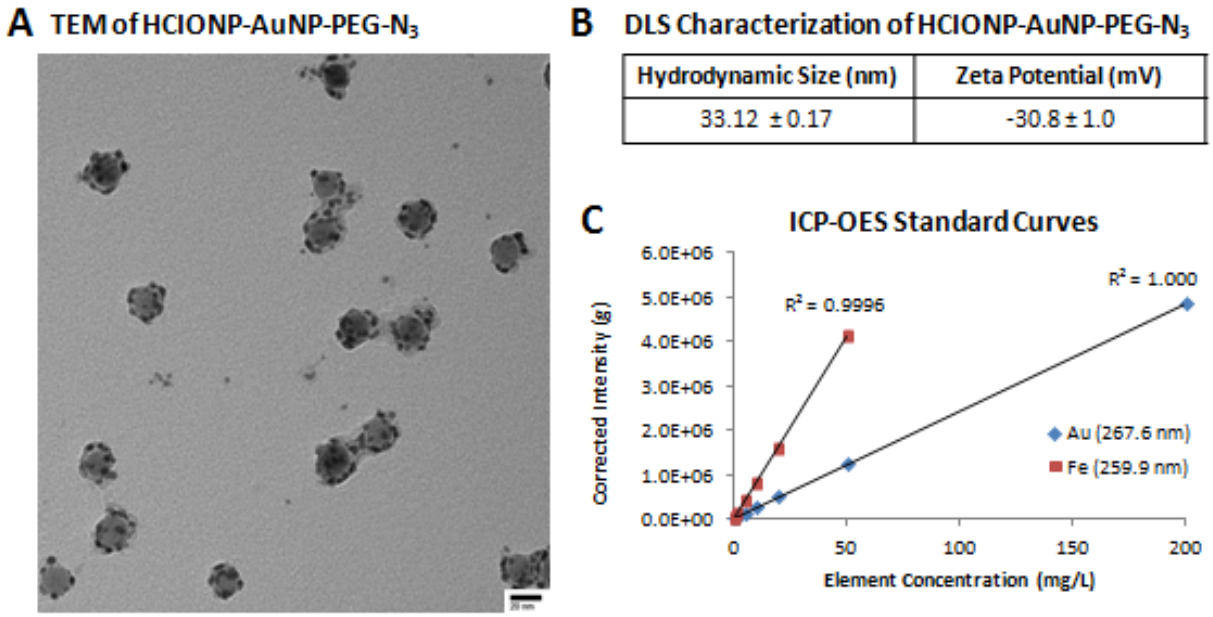

Figure 5.3. (A) TEM of core-satellite structure of azide-PEG-coated HCIONP-AuNPs before overnight click chemistry reaction with alkyne-peptide (scale bar = 20 nm). (B) Hydrodynamic size and zeta potential (average ± standard deviation) of HCIONP-AuNP-PEG-N_3 before click chemistry reaction, obtained using dynamic light scattering. (C) ICP-OES elemental standard curves of iron (Fe) and gold (Au) used to calculate the HCIONP and AuNP concentrations of the azide-PEG-coated HCIONP-AuNPs digested overnight in aqua regia.

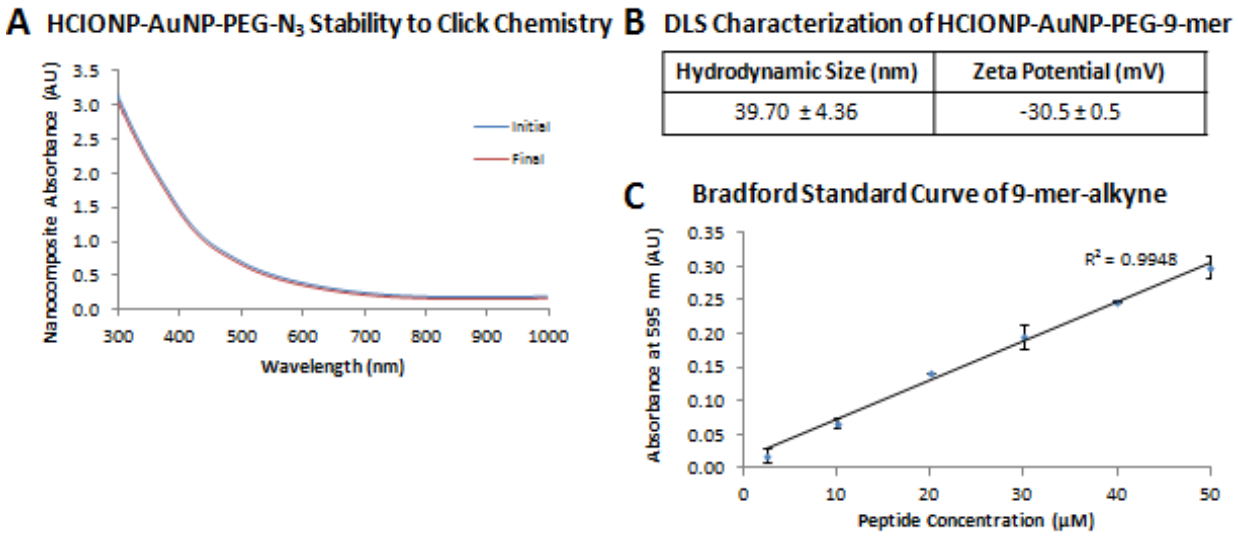

Figure 5.4. (A) Absorbance curves of azide-PEG-coated HCIONP-AuNP nanocomposites before and after overnight click chemistry reaction with alkyne-peptide. Note as the PTT-mediating AuNP satellites become ultra-small, they no longer express the 520 nm peak. (B) Hydrodynamic size and zeta potential (average ± standard deviation) of HCIONP-AuNP-PEG-N_3 after click

chemistry addition of alkyne-peptide, obtained using dynamic light scattering. (C) Bradford standard curves of 9-mer-alkyne in presence of 200 μM copper sulfate and 1 mM sodium ascorbate, used to calculate the concentration of unbound alkyne-peptide in the supernatant after click chemistry addition to the of HCIONP-AuNP-PEG-N_3 nanocomposite.

5.7 Acknowledgements

Others who contributed to this work include Nicholas O. Stevers, Hongwei Chen, and Duxin Sun in the Pharmaceutical Sciences department at the University of Michigan. I would also like to thank Mitchell Smith and Anne McNeil in the University of Michigan Chemistry Department for their gel permeation chromatography support. This work was supported in part by the NIH Pharmacological Sciences Training Program (H. Paholak), the American Foundation for Pharmaceutical Education Pre-Doctoral Fellowship (H. Paholak), and the University of Michigan Rackham Pre-Doctoral Fellowship (H. Paholak).

5.8 References

1. Chandasana, H., et al., *Corneal targeted nanoparticles for sustained natamycin delivery and their PK/PD indices: an approach to reduce dose and dosing frequency.* Int J Pharm, 2014. **477**(1-2): p. 317-25.

2. Shegokar, R., *Nanotechnology in Diagnosis, Treatment and Prophylaxis of Infectious Diseases.* Nanotechnology in Diagnosis, Treatment and Prophylaxis of Infectious Diseases, 2015: p. 233-249.

3. Milane, L., Z.F. Duan, and M. Amiji, *Pharmacokinetics and biodistribution of lonidamine/paclitaxel loaded, EGFR-targeted nanoparticles in an orthotopic animal model of multi-drug resistant breast cancer.* Nanomedicine, 2011. **7**(4): p. 435-44.

4. Chen, H., et al., *Anti-HER2 antibody and ScFvEGFR-conjugated antifouling magnetic iron oxide nanoparticles for targeting and magnetic resonance imaging of breast cancer.* Int J Nanomedicine, 2013. **8**: p. 3781-94.

5. Adolphi, N.L., et al., *Imaging of Her2-targeted magnetic nanoparticles for breast cancer detection: comparison of SQUID-detected magnetic relaxometry and MRI.* Contrast Media Mol Imaging, 2012. **7**(3): p. 308-19.

6. Gormley, A.J., et al., *Biological evaluation of RGDfK-gold nanorod conjugates for prostate cancer treatment.* J Drug Target, 2011. **19**(10): p. 915-24.

7. Polyak, D., et al., *Development of PEGylated doxorubicin-E-[c(RGDfK)(2)] conjugate for integrin-targeted cancer therapy.* Polymers for Advanced Technologies, 2011. **22**(1): p. 103-113.

8. Choi, H., et al., *Iron oxide nanoparticles as magnetic resonance contrast agent for tumor imaging via folate receptor-targeted delivery.* Acad Radiol, 2004. **11**(9): p. 996-1004.

9. Madan, J., et al., *Enhanced noscapine delivery using estrogen-receptor-targeted nanoparticles for breast cancer therapy.* Anticancer Drugs, 2014. **25**(6): p. 704-16.

10. Yue, J., et al., *Transferrin-conjugated micelles: enhanced accumulation and antitumor effect for transferrin-receptor-overexpressing cancer models.* Mol Pharm, 2012. **9**(7): p. 1919-31.

11. Oyelere, A.K., et al., *Peptide-conjugated gold nanorods for nuclear targeting.* Bioconjugate Chemistry, 2007. **18**(5): p. 1490-1497.

12. Porta, F., et al., *Folic acid-modified mesoporous silica nanoparticles for cellular and nuclear targeted drug delivery.* Adv Healthc Mater, 2013. **2**(2): p. 281-6.

13. Wang, L., et al., *CD44 antibody-targeted liposomal nanoparticles for molecular imaging and therapy of hepatocellular carcinoma.* Biomaterials, 2012. **33**(20): p. 5107-14.

14. Wang, C.H., et al., *Photothermolysis of glioblastoma stem-like cells targeted by carbon nanotubes conjugated with CD133 monoclonal antibody.* Nanomedicine, 2011. **7**(1): p. 69-79.

15. Torchilin, V.P., *Passive and active drug targeting: drug delivery to tumors as an example.* Handb Exp Pharmacol, 2010(197): p. 3-53.

16. Bertrand, N., et al., *Cancer nanotechnology: the impact of passive and active targeting in the era of modern cancer biology.* Adv Drug Deliv Rev, 2014. **66**: p. 2-25.

17. Wang, R.B., P.S. Billone, and W.M. Mullett, *Nanomedicine in Action: An Overview of Cancer Nanomedicine on the Market and in Clinical Trials.* Journal of Nanomaterials, 2013.

18. Molina, M.A., et al., *Trastuzumab (herceptin), a humanized anti-Her2 receptor monoclonal antibody, inhibits basal and activated Her2 ectodomain cleavage in breast cancer cells.* Cancer Res, 2001. **61**(12): p. 4744-9.

19. Russo, E., *The birth of biotechnology.* Nature, 2003. **421**(6921): p. 456-7.

20. *The Role of Anti-PD-L1 Immunotherapy in Cancer.* OncLive, 2014.

21. Deng, L., et al., *Irradiation and anti-PD-L1 treatment synergistically promote antitumor immunity in mice.* J Clin Invest, 2014. **124**(2): p. 687-95.

22. Kim, J.W. and J.P. Eder, *Prospects for targeting PD-1 and PD-L1 in various tumor types.* Oncology (Williston Park), 2014. **28 Suppl 3**: p. 15-28.

23. Postow, M.A., M.K. Callahan, and J.D. Wolchok, *Immune Checkpoint Blockade in Cancer Therapy.* J Clin Oncol, 2015. **33**(17): p. 1974-82.

24. Alley, S.C., N.M. Okeley, and P.D. Senter, *Antibody-drug conjugates: targeted drug delivery for cancer.* Curr Opin Chem Biol, 2010. **14**(4): p. 529-37.

25. Yao, S., *FDA approves new treatment for late-stage breast cancer.* FDA.gov, 2013.

26. Jefferson, E., *FDA approves Adcetris to treat two types of lymphoma.* FDA.gov, 2011.

27. Mas-Moruno, C., F. Rechenmacher, and H. Kessler, *Cilengitide: the first anti-angiogenic small molecule drug candidate design, synthesis and clinical evaluation.* Anticancer Agents Med Chem, 2010. **10**(10): p. 753-68.

28. Thundimadathil, J., *Cancer treatment using peptides: current therapies and future prospects.* J Amino Acids, 2012. **2012**: p. 967347.

29. Schally, A.V., et al., *Use of analogs of peptide hormones conjugated to cytotoxic radicals for chemotherapy targeted to receptors on tumors.* Curr Drug Deliv, 2011. **8**(1): p. 11-25.

30. Libutti, S.K., et al., *Phase I and pharmacokinetic studies of CYT-6091, a novel PEGylated colloidal gold-rhTNF nanomedicine.* Clin Cancer Res, 2010. **16**(24): p. 6139-49.

31. Powell, A.C., G.F. Paciotti, and S.K. Libutti, *Colloidal gold: a novel nanoparticle for targeted cancer therapeutics.* Methods Mol Biol, 2010. **624**: p. 375-84.

32. *Aurolase Therapy.* Nanospectra.

33. Zou, P., et al., *Superparamagnetic iron oxide nanotheranostics for targeted cancer cell imaging and pH-dependent intracellular drug release.* Mol Pharm, 2010. **7**(6): p. 1974-84.

34. Murthy, N., et al., *Bioinspired pH-responsive polymers for the intracellular delivery of biomolecular drugs.* Bioconjug Chem, 2003. **14**(2): p. 412-9.

35. Murthy, N., et al., *Design and synthesis of pH-responsive polymeric carriers that target uptake and enhance the intracellular delivery of oligonucleotides.* J Control Release, 2003. **89**(3): p. 365-74.

36. Muhammad, F., et al., *pH-Triggered controlled drug release from mesoporous silica nanoparticles via intracelluar dissolution of ZnO nanolids.* J Am Chem Soc, 2011. **133**(23): p. 8778-81.

37. Hua, D., et al., *Potent tumor targeting drug release system comprising MMP-2 specific peptide fragment with self-assembling characteristics.* Drug Des Devel Ther, 2014. **8**: p. 1839-49.

38. Roomi, M.W., et al., *Patterns of MMP-2 and MMP-9 expression in human cancer cell lines.* Oncol Rep, 2009. **21**(5): p. 1323-33.

39. Foda, H.D. and S. Zucker, *Matrix metalloproteinases in cancer invasion, metastasis and angiogenesis.* Drug Discov Today, 2001. **6**(9): p. 478-482.

40. Cai, W., et al., *Applications of gold nanoparticles in cancer nanotechnology.* Nanotechnol Sci Appl, 2008. **2008**(1).

41. Montet, X., et al., *Multivalent effects of RGD peptides obtained by nanoparticle display.* J Med Chem, 2006. **49**(20): p. 6087-93.

42. Hamley, I.W., *PEG-peptide conjugates.* Biomacromolecules, 2014. **15**(5): p. 1543-59.

43. Chen, H., et al., *Facile Fabrication of Near-Infrared-Resonant and Magnetic Resonance Imaging-Capable Nanomediators for Photothermal Therapy.* ACS Appl Mater Interfaces, 2015. **7**(23): p. 12814-23.

44. *Chemistry of Crosslinking.* ThermoFisher Scientific, 2015.

45. Chen, J., et al., *Hypoxia potentiates Notch signaling in breast cancer leading to decreased E-cadherin expression and increased cell migration and invasion.* Br J Cancer, 2010. **102**(2): p. 351-60.

46. D'Angelo, R.C., et al., *Notch reporter activity in breast cancer cell lines identifies a subset of cells with stem cell activity.* Mol Cancer Ther, 2015. **14**(3): p. 779-87.

47. Le Droumaguet, B. and K. Velonia, *Click chemistry: A powerful tool to create polymer-based macromolecular chimeras.* Macromolecular Rapid Communications, 2008. **29**(12-13): p. 1073-1089.

48. Sletten, E.M. and C.R. Bertozzi, *From Mechanism to Mouse: A Tale of Two Bioorthogonal Reactions.* Accounts of Chemical Research, 2011. **44**(9): p. 666-676.

49. Nwe, K. and M.W. Brechbiel, *Growing Applications of "Click Chemistry" for Bioconjugation in Contemporary Biomedical Research.* Cancer Biotherapy and Radiopharmaceuticals, 2009. **24**(3): p. 289-302.

50. von Maltzahn, G., et al., *In vivo tumor cell targeting with "Click" nanoparticles.* Bioconjugate Chemistry, 2008. **19**(8): p. 1570-1578.

51. Lu, J., M. Shi, and M.S. Shoichet, *Click Chemistry Functionalized Polymeric Nanoparticles Target Corneal Epithelial Cells through RGD-Cell Surface Receptors.* Bioconjugate Chemistry, 2009. **20**(1): p. 87-94.

52. Huang, X.H., et al., *Cancer cell imaging and photothermal therapy in the near-infrared region by using gold nanorods.* Journal of the American Chemical Society, 2006. **128**(6): p. 2115-2120.

53. Huang, X.H., et al., *Determination of the minimum temperature required for selective photothermal destruction of cancer cells with the use of immunotargeted gold nanoparticles.* Photochemistry and Photobiology, 2006. **82**(2): p. 412-417.

54. Hirsch, L.R., et al., *Nanoshell-mediated near infrared photothermal tumor therapy.* Proceedings of the 25th Annual International Conference of the Ieee Engineering in Medicine and Biology Society, Vols 1-4, 2003. **25**: p. 1230-1231.

55. Loo, C., et al., *Immunotargeted nanoshells for integrated cancer imaging and therapy.* Nano Letters, 2005. **5**(4): p. 709-711.

56. Mahmood, U. and R. Weissleder, *Near-infrared optical imaging of proteases in cancer.* Molecular Cancer Therapeutics, 2003. **2**(5): p. 489-496.

57. Eustis, S. and M.A. El-Sayed, *Why gold nanoparticles are more precious than pretty gold: Noble metal surface plasmon resonance and its enhancement of the radiative and nonradiative properties of nanocrystals of different shapes.* Chemical Society Reviews, 2006. **35**(3): p. 209-217.

58. Chen, H.W., et al., *Living' PEGylation on gold nanoparticles to optimize cancer cell uptake by controlling targeting ligand and charge densities.* Nanotechnology, 2013. **24**(35).

59. Dreaden, E.C., et al., *Beating cancer in multiple ways using nanogold.* Chem Soc Rev, 2011. **40**(7): p. 3391-404.

60. Liu, X., et al., *Extinction coefficient of gold nanoparticles with different sizes and different capping ligands.* Colloids Surf B Biointerfaces, 2007. **58**(1): p. 3-7.

61. Chen, H.W., et al., *Highly crystallized iron oxide nanoparticles as effective and biodegradable mediators for photothermal cancer therapy.* Journal of Materials Chemistry B, 2014. **2**(7): p. 757-765.

62. Chen, H.W., et al., *Reducing non-specific binding and uptake of nanoparticles and improving cell targeting with an antifouling PEO-b-P gamma MPS copolymer coating.* Biomaterials, 2010. **31**(20): p. 5397-5407.

63. Levin, C.S., et al., *Determining the conformation of thiolated poly(ethylene glycol) on Au nanoshells by surface-enhanced Raman scattering spectroscopic assay.* Analytical Chemistry, 2006. **78**(10): p. 3277-3281.

64. Lü, X.L., Dejun; Huang, Yan; Zhang, Yiyun, *Application of a modified Coomassie brilliant blue protein assay in the study of protein adsorption on carbon thin films.* Surface & Coatings Technology, 2007. **201**: p. 6843-6846.

65. *Pilot Study of AuroLase(tm) Therapy in Refractory and/or Recurrent Tumors of the Head and Neck.* ClinicalTrials.gov.

66. *Efficacy Study of AuroLase Therapy in Subjects With Primary and/or Metastatic Lung Tumors.* ClinicalTrials.gov.

67. Toraya-Brown, S., et al., *Local hyperthermia treatment of tumors induces CD8(+) T cell-mediated resistance against distal and secondary tumors.* Nanomedicine, 2014. **10**(6): p. 1273-85.

68. Wang, C., et al., *Immunological Responses Triggered by Photothermal Therapy with Carbon Nanotubes in Combination with Anti-CTLA-4 Therapy to Inhibit Cancer Metastasis.* Advanced Materials, 2014. **26**(48): p. 8154-8162.

69. Bear, A.S., et al., *Elimination of metastatic melanoma using gold nanoshell-enabled photothermal therapy and adoptive T cell transfer.* PLoS One, 2013. **8**(7): p. e69073.

CHAPTER 6. SUMMARY

Rapid advances in bioinformatics and nanotechnology have led to an exciting time in the history of medicine; pre-clinical cancer research is booming with development of innovative therapies with promise to transform clinical approaches to cancer therapy, which for decades has been dominated by surgery, chemotherapy, and radiation. Cancer nanomedicine is a broad field of research that offers tremendous potential to be combined with current cancer therapies to overcome key challenges that stem from the inherent properties of cancer cells. Here we highlight a few of these challenging features of cancer, and present nanoparticle-mediated photothermal therapy as a multifunctional platform to address the obstacles they pose for cancer medicine.

First, cancer cells are highly adaptable for survival, which often allows them to rely on alternate signaling in response to cancer therapy and can lead to acquired resistance [1-3]. Second, cells comprising solid tumors can be heterogeneous in type(e.g., cancer-associated fibroblasts), and can differ more subtly in terms of genetic or epigenetic changes that alter phenotype and can lead to varying functional roles to sustain tumors [4, 5]. Consequently, these cellular differences may necessitate more than one therapeutic target for effective elimination [6]. In the last decade cancer stem cells (CSCs) have attracted increasing attention as a critical target, given the growing body of evidence suggesting a role in driving tumor initiation, tumor

growth, metastasis, and resistance to conventional therapies [7-13]. Third, for tumor growth and metastasis to occur, cancer cells adapt to escape recognition and destruction by immune cells [14, 15].

These features of cancer pose significant obstacles in achieving lasting effects from conventional therapies alone, such as chemotherapy and radiation which generally aim to kill rapidly dividing cells but offer little specificity. While many localized cancers caught early enough are not fatal, efficacy of treatment is severely impaired when cancer cells are no longer localized but have disseminated from the primary tumor site and established metastatic growths [16].

The overall goal of this work is to develop a nanoparticle approach to address two key challenges of cancer medicine: enhancing efficacy in metastatic settings and increasing specificity to reduce associated toxicity. As such, we developed two objectives utilizing nanoparticle-mediated photothermal therapy as a multifunctional platform: 1) to inhibit cancer stem cells and tumor-mediated immunosuppressive signaling as vital drivers of tumor growth and metastasis, and 2) to enhance targeting specificity of therapy.

In the first section of this dissertation (Chapters 2 and 3), we investigate the efficacy of employing nanoparticle-mediated photothermal therapy (PTT) to inhibit cancer stem cells and tumor-mediated immunosuppressive signaling – vital drivers of cancer growth and metastasis. Combination therapy incorporating nanoparticle-mediated PTT, as we present here, or modification of the nanoparticles themselves for multimodal therapy (e.g., PTT and drug delivery) may be utilized to enhance treatment efficacy and mitigate acquired resistance. In addition to serving as a multifunctional platform to address key challenges of cancer therapy,

another major advantage of nanoparticle-mediated PTT is its potential to improve the specificity and efficiency of cancer cell destruction by being localized and targeted. Given the lack of specificity and off-target toxicity of mainstream cancer therapy (e.g., chemotherapy), we dedicated the second section of this dissertation (Chapters 4 and 5) to the development of optimized formulations of targeted nanoparticles for photothermal cancer therapy.

In Chapter 2, we evaluate the ability of photothermal therapy via highly crystallized iron oxide nanoparticles (HCIONPs) to inhibit breast cancer stem cells (BCSCs) to prevent metastasis following treatment of the primary tumor. We conduct rigorous, translational studies to evaluate the effect of PTT via HCIONPs on epithelial-like (ALDH+) and mesenchymal-like (CD44+/CD24-) BCSCs in triple negative breast cancer *in vitro* and *in vivo*, and combine PTT with surgical resection to prevent lymph node and other metastasis. We reveal *in vitro* that PTT ALDH+ BCSCs are more sensitive to PTT than CD44+/CD24- BCSCs, and identify conditions in which both populations are eliminated preferentially to differentiated cancer cells. For the first time, we show that PTT inhibits breast cancer stem cell self-renewal *in vitro*. Through secondary implantation we demonstrate that PTT impedes BCSC-driven tumor formation in immune-compromised mice. Finally, we show that PTT before surgery significantly reduces metastasis development in triple negative breast cancer. Taken together, these results suggest the potential to combine nanoparticle-mediated photothermal therapy with current clinical treatments such as surgery to enhance CSC destruction and improve long-term survival in breast cancer patients.

In Chapter 3, we sought to inhibit breast cancer stem cells and prevent metastasis in immune-competent mice with photothermal therapy using HCIONPs, and to conduct initial studies of the ability to induce a systemic (BCSC-specific) immune response when used in

conjunction with immunotherapy. In 4T1 metastatic breast cancer cells, twenty minute HCIONP-mediated PTT significantly reduces ALDH+ BCSCs *in vitro*. In 4T1 tumor-bearing mice ALDH+ BCSCs are significantly inhibited by PTT when given as monotherapy and in combination with PD-L1 antibody. Combination treatment with PTT and PD-L1 antibody reveals promising reductions in tumor growth and formation of lung macrometastases. Increases of key inflammatory cytokines (IL-6) and immune cell-attracting chemokines (CXCL-1, CXCL-9, CXCL-10) in serum of dual treated mice suggest the potential to enhance the population of tumor-infiltrating effector T-cells, which will be confirmed with quantitative immunophenotyping of saved tumor tissues. The preliminary data summarized here lays a foundation for continued experiments to demonstrate conditions in which localized PTT, when combined with immune checkpoint blockade, effectively prevents metastasis through inhibition of BCSCs and eliminates existing metastases by triggering a systemic, cancer (stem) cell-specific immune response. Successful development of such translational nanomedicine to extend immunotherapy to metastatic breast cancer patients would have potential to significantly improve survival of a widespread and currently incurable disease.

In Chapter 4, we report a new technique – 'living' PEGylation – that allows control of the density and composition of heterobifunctional PEG (HS-PEG-R) on gold nanoparticles (AuNPs), and demonstrate potential applications in cancer nanomedicine including photothermal therapy. We first establish 'living' PEGylation by incubating HS-PEG-COOH with AuNPs at increasing molar ratios from zero to 2000. This causes the hydrodynamic layer thickness to differentially increase up to 26 nm. The controlled, gradual increase in PEG-COOH density is revealed after centrifugation, based on the ability to re-suspend the pellet and increase the AuNP absorption. Using a fluorescamine-based assay we quantify differential HS-PEG-NH_2 binding to AuNPs,

revealing it is highly efficient until AuNP saturation. Furthermore, the zeta potential incrementally changes from −44.9 to +52.2 mV and becomes constant upon saturation. Using 'living' PEGylation we prepare AuNPs with different ratios of HS-PEG-RGD and incubate them with U-87 MG and non-target cells, demonstrating that targeting ligand density is critical to maximizing the targeting efficiency of AuNPs to cancer cells. The ability to minimize non-specific binding/uptake by healthy cells could further improve targeted nanoparticle efficacy. Consequently, we sequentially control the HS-PEG-R density to develop multifunctional nanoparticles, conjugating positively-charged HS-PEG-NH_2 at increasing ratios to AuNPs containing negatively-charged HS-PEG-COOH to reduce uptake by macrophage cells. Application of this facile PEGylation technique to PTT-mediating nanoparticles to enhance the ratio of uptake by target versus non-target cells could significantly improve patient response and decrease both the dose and cost of treatment. Furthermore, future work to enhance formulation of such stealthy, targeted nanoparticles to confer imaging capabilities could potentially enable PTT to be applied to metastatic cancers.

In Chapter 5, we describe a facile, optimized design for actively targeted, theranostic nanocomposites with a core-satellite structure for photothermal therapy and magnetic resonance imaging (MRI). A small, "clickable" targeting peptide facilely synthesized with an N-terminal alkyne separated by two 6-aminohexanoic acid spacers enables precise control over attachment to the nanoparticles to prevent steric hindrance and optimize binding with the target receptor. The PTT nanoparticle formulation consisting of azide-coated nanocomposites with a HCIONP core (17 nm) and ultra-small AuNP satellites (4 nm) results in enhanced stability with highly efficient conjugation of the targeting peptide by azide-alkyne click chemistry. This was determined by changes in hydrodynamic size (33.1 to 39.7 nm) and peptide quantification via the

Bradford assay. The high stability of the HCIONP-AuNP-PEG-N_3 nanocomposite makes it ideal for controlled conjugation of cysteine-containing peptides which would otherwise directly attach to the AuNP surface. Furthermore, compared to AuNPs often used for PTT, the HCIONP core of the nanocomposite enables purification by magnet if desired. MRI capabilities allow *in vivo* visualization of tumor tissue by MRI before and after treatment, and may even enable PTT at metastatic sites. The HCIONP-AuNP nanocomposites with tumor-targeting, clickable peptides for PTT and MRI presented here exemplify controlled delivery of localized therapy to reduce off-target toxicity and consequently increase both patient tolerance and response to cancer treatment.

Ideally, future studies inspired by this work would focus on developing targeted photothermal therapy to engage patients' own immune systems to fight metastatic cancers. The theranostic HCIONP-AuNP nanocomposites formulated via click chemistry for multivalent display of peptides, discussed in Chapter 5, could be used to demonstrate efficient PTT targeting to BCSCs, perhaps utilizing the Notch receptor-targeting 9-mer peptide studied in Appendix A. To achieve long-term efficacy, therapy utilizing PTT should be designed to inhibit local and distal BCSCs. Building off of the work described in Chapter 3, PTT via the nanocomposites could be evaluated for its ability to kill both differentiated cancer cells and BCSCs located in primary tumors and consequently train T-cells to recognize and kill remaining cells at the tumor and metastatic sites. As in Chapter 3, the potential to enhance this effect following PTT could be studied by combination with cancer immunotherapy such as antibodies for T-cell checkpoint inhibition. Furthermore, the ability for MRI via the targeted HCIONP-AuNP nanocomposites would facilitate studies to detect the nanocomposites bound to distal cancer cells and conduct PTT at certain metastatic sites, such as the lungs.

Following such efficacy studies, additional studies to demonstrate safety would be critical to pushing the therapy described here into clinical trials. The actively targeted nanoparticles for externally controlled photothermal therapy combines multiple approaches for delivering localized therapy that when applied in the clinic could reduce off-target toxicity and increase patient tolerance to treatment. Clinical translation of this nanomedicine approach to stimulate patients' immune systems to eliminate differentiated cancer cells and CSCs at both local and distal sites could lead to viable treatment options for multiple types of metastatic cancer, with significant potential to improve long-term survival in patients considered incurable with current therapies.

References

1. Logue, J.S. and D.K. Morrison, *Complexity in the signaling network: insights from the use of targeted inhibitors in cancer therapy.* Genes Dev, 2012. **26**(7): p. 641-50.
2. Ribeiro, J.R. and R.N. Freiman, *Estrogen signaling crosstalk: Implications for endocrine resistance in ovarian cancer.* J Steroid Biochem Mol Biol, 2014. **143**: p. 160-73.
3. Yamaguchi, H., et al., *Signaling cross-talk in the resistance to HER family receptor targeted therapy.* Oncogene, 2014. **33**(9): p. 1073-81.
4. Marusyk, A., V. Almendro, and K. Polyak, *Intra-tumour heterogeneity: a looking glass for cancer?* Nat Rev Cancer, 2012. **12**(5): p. 323-34.
5. Zellmer, V.R. and S. Zhang, *Evolving concepts of tumor heterogeneity.* Cell Biosci, 2014. **4**: p. 69.
6. Korkaya, H. and M.S. Wicha, *Selective targeting of cancer stem cells: a new concept in cancer therapeutics.* BioDrugs, 2007. **21**(5): p. 299-310.
7. Wicha, M.S., S. Liu, and G. Dontu, *Cancer stem cells: an old idea--a paradigm shift.* Cancer Res, 2006. **66**(4): p. 1883-90; discussion 1895-6.
8. Reya, T., et al., *Stem cells, cancer, and cancer stem cells.* Nature, 2001. **414**(6859): p. 105-11.

9. Liu, S., et al., *Breast cancer stem cells transition between epithelial and mesenchymal states reflective of their normal counterparts.* Stem Cell Reports, 2014. **2**(1): p. 78-91.

10. Atkinson, R.L., et al., *Thermal enhancement with optically activated gold nanoshells sensitizes breast cancer stem cells to radiation therapy.* Sci Transl Med, 2010. **2**(55): p. 55ra79.

11. Bao, S., et al., *Glioma stem cells promote radioresistance by preferential activation of the DNA damage response.* Nature, 2006. **444**(7120): p. 756-60.

12. Conley, S.J., et al., *Antiangiogenic agents increase breast cancer stem cells via the generation of tumor hypoxia.* Proc Natl Acad Sci U S A, 2012. **109**(8): p. 2784-9.

13. Korkaya, H., et al., *Activation of an IL6 inflammatory loop mediates trastuzumab resistance in HER2+ breast cancer by expanding the cancer stem cell population.* Mol Cell, 2012. **47**(4): p. 570-84.

14. Dunn, G.P., L.J. Old, and R.D. Schreiber, *The three Es of cancer immunoediting.* Annu Rev Immunol, 2004. **22**: p. 329-60.

15. Schreiber, R.D., L.J. Old, and M.J. Smyth, *Cancer immunoediting: integrating immunity's roles in cancer suppression and promotion.* Science, 2011. **331**(6024): p. 1565-70.

16. Hunter, K.W., N.P. Crawford, and J. Alsarraj, *Mechanisms of metastasis.* Breast Cancer Res, 2008. **10 Suppl 1**: p. S2.

APPENDIX A. EVALUATION OF JAGGED1 PEPTIDES TO TARGET BREAST CANCER STEM CELLS THROUGH NOTCH RECEPTOR EXPRESSION

A.1 Abstract

Recent advances in nanoparticle development offer great potential to enhance efficacy of cancer therapies against treatment-resistant cancer stem cells. Given the advancement of nanoparticle-mediated photothermal therapy (PTT) to clinical trials and preliminary pre-clinical reports of efficacy at eliminating breast cancer stem cells (BCSCs), we sought to develop targeted nanoparticles to specifically direct photothermal therapy to BCSCs. Here we present our work to evaluate peptides to target PTT-mediating nanoparticles to Notch receptors over-expressed on BCSCs. Various peptides ranging in size from nine to 23 amino acids were selected based on sequences in the Delta/Serrate/Lag-2 (DSL) and epidermal growth factor (EGF) regions of the endogenous Notch ligand Jagged1. Following synthesis and purification, the effect of peptide incubation on Notch activity was determined by a Luciferase assay following six hour incubation with Notch-expressing breast cancer cell lines (MDA-MB-231, ZR-75-1) transduced with a Notch reporter. None of the Jagged1 peptides caused a significant difference in the luminescence signal compared to non-treated cells, mitigating concerns of potential stimulation of Notch activity. Fluorescent forms of each peptide, with Fluorescein added to the N-terminus separated by two 6-aminohexanoic acid spacers, were also synthesized

to determine peptide binding affinity for Notch receptors. First fluorescence imaging was conducted of MDA-MB-231 cells and negative control H520 cells incubated with fluorescent peptides. Next, fluorescence imaging was conducted following a competition study in MDA-MB-231 cells, which were incubated with fluorescent peptides following pre-treatment with unlabeled peptide to assess specificity of binding. In both experiments the nine amino acid peptide appeared to have favorable binding properties over the other peptides, with higher fluorescence observed in the first imaging study and lower non-specific fluorescence following pre-treatment with unlabeled peptide in the competition study. Competition studies with the 9-mer and fluorescent 9-mer were then repeated in four Notch-expressing breast cancer cell lines for quantitative analysis via flow cytometry. However, pre-treatment with unlabeled 9-mer did not affect the fluorescence signal compared to cells incubated only with fluorescent 9-mer. Our data suggest that Jagged1 peptides, when incubated freely in solution, have low binding affinities for Notch receptors, requiring relatively high concentrations for *in vitro* studies. Presentation of the Jagged1 peptides on a nanoparticle surface, enabling a multivalent effect in which simultaneous interactions with the cell surface occur, may improve peptide binding affinity and potentially enhance uptake of nanoparticles by Notch-expressing cells, meriting further study.

A.2 Introduction

Despite only comprising a small portion of solid tumors, by their resilient nature and critical role in driving multiple events in cancer progression, cancer stem cells (CSCs) present one of the greatest obstacles in developing effective therapies that lead to long-term patient survival. Cancer stem cells were first discovered in 1997 in acute myeloid leukemia by Dick and

colleagues [1]. While evidence of the existence of CSCs has been reported for multiple types of solid cancers [2-6], those in breast cancer remain among the most extensively studied largely in part to Wicha and colleagues [2, 7-15]. An increasing body of research supports a model in which tumors arise from transformed stem or progenitor cells that normally exist in healthy tissues to support tissue maintenance and repair. These relatively long-lived stem cells have a greater susceptibility to acquiring mutations, which, through alterations in regulation of self-renewal and differentiation, results in an ability to drive tumor formation [16, 17]. Furthermore, the literature supports a model for metastasis in which CSCs are the only type of disseminated cancer cell with the ability to drive growth of macrometastases at distal sites [16, 18, 19]. As recently reported by the Wicha lab, breast cancer stem cells (BCSCs) can transition between epithelial-like and mesenchymal-like states traceable by aldehyde dehydrogenase (ALDH+) and CD44+/CD24- markers, respectively. Their data suggest that mesenchymal-like BCSCs may play a more dominant role in dissemination and migration, while epithelial-like BCSCs are more proliferative and more likely to drive tumor growth at the site of origin and distal sites [13]. As expected given the key role of stem cells in ensuring maintenance and survival of healthy tissue, CSCs also exhibit resilient qualities. For instance, features such as resistance to apoptosis and increased transporter activity [16] facilitate increased resistance to conventional therapies such as chemotherapy and radiation [9, 20-22]. While success of cancer therapies varies widely by type and stage of the disease, incorporating a component specifically aimed to eliminate CSCs may be a critical factor to prevent development of acquired resistance, recurrence, and progression of the disease [23, 24].

Various strategies have been explored to develop CSC-specific therapies. Agents such as all-trans retinoic acid may be used to induce stem cell differentiation into cancer cells which are

more responsive to subsequent treatment with conventional therapies [24-26]. Another strategy to incorporate agents selective to CSCs is to inhibit key CSC signaling pathways, such as Wnt, Hedgehog, and Notch that modulate self-renewal [16, 17, 24, 27-29]. In 2012 Genentech's Vismodegib, an inhibitor of Smoothened (SMO) in the Sonic Hedgehog (SHH) pathway, was approved in 2012 by the Food and Drug Administration (FDA) for basal-cell carcinoma (BCC) [29]. Like Vismodegib, most other SHH-targeting agents in clinical trials are cyclopamine-competitive antagonists of SMO, including Sonidegib and Saridegib. Notch inhibitors in development aim to block signaling at various points in the pathway including binding of the Delta-like (DLL) and Jagged ligands, and activity of the γ-secretase enzyme which plays a key role in trafficking that leads to transcription of Notch target genes [30-32]. Clinical trials of Notch-targeting agents include several γ-secretase inhibitors (GSIs) produced by various companies as well as monoclonal antibodies to block ligand binding, including anti-Notch 1, 2, and 3 antibodies and multiple anti-DLL4 antibodies [29]. Additional methods that have been explored include inhibitors of various cytokine pathways; both inhibitors of intracellular targets (e.g., Perifosine to inhibit AKT [33, 34]) and extracellular signaling from the tumor microenvironment (e.g., Repertaxin to inhibit IL-8 signaling through the CXCR1 receptor [12, 33]).

While few nanoparticle-based therapies, and none targeting CSCs, have advanced to clinical trials, recent advances in nanoparticle development offer great potential to combine strategies to enhance cancer treatment efficacy against CSCs. In 2010, nanoparticle-mediated hyperthermia was reported to improve efficacy of ionizing radiation (IR) against BCSCs [20]. The authors used light-activated gold nanoshells to induce photothermal therapy (PTT), one of few nanoparticle-based treatments to advance to clinical trials. They found PTT impairs the

ability to repair double-stranded breaks in DNA caused by IR, which was suggested to be the result of changes in heat shock protein expression caused by PTT. In a subsequent study, carbon nanotube-mediated PTT was found to sensitize breast cancer stem-like cells to hyperthermia over comparable heating via water bath [35]. While rapid heat transfer from PTT causes the overall solution temperature to become mildly hyperthermic [36], the cytotoxic effect is amplified by the presence of nanoparticles in close proximity to the cells as the heat transfer is significantly greater at the nanoparticle surface [37].

With this in mind, we sought to direct photothermal therapy to BCSCs through Notch-targeted nanoparticles. While Notch-targeting antibodies have been commercially developed [29, 38, 39], production and purification is expensive and their relatively large size limits the potential loading capacity of a therapeutic drug onto the nanoparticle surface. A design to maximize both targeting efficiency and potency of drug-loaded nanoparticles would be ideal for multimodal therapy with PTT and extending applications to CSC-targeted drug delivery. High affinity peptides derived from the binding region of an antibody are cheaper and simpler to produce and purify, and would allow more room on the nanoparticle surface for attachment of a drug. A previously reported 17-amino acid peptide derived from the Jagged1 ligand [30] served as a basis for design and exploration of Notch-binding peptides intended to target nanoparticle-mediated therapies, PTT in particular, to BCSCs.

A.3 Results and Discussion

Following the discovery of breast CSCs as the first solid tumor CSCs, Dontu et al. demonstrated the involvement of Notch signaling in mammary stem/progenitor cell self-renewal

and differentiation and proposed that dysregulation of the pathway could give rise to breast CSCs [30]. Additional studies since have demonstrated a crucial role for Notch signaling in other types of CSCs [40-42]. The Notch receptor family is composed of four mammalian homologs (Notch1-4). Signaling can be activated by binding of Delta-like (DLL1, DLL3, DLL4) or Jagged (Jagged1, Jagged2) ligands on a neighboring cell. This induces a series of receptor cleavage events involving A Disintegrin and Metalloproteinase (ADAM) and γ-secretase enzymes, resulting in release of the Notch Intracellular Domain (NICD) which traffics to the nucleus and relieves repression of transcription factors for genes such as those in the *HES* family [30-32].

Of the various Notch receptors, the correlation between Notch1 and Notch4 receptor expression and poor clinical outcome has been most predominantly studied in breast and other cancers. Notch2 expression has been associated with better clinical outcome than the other Notch receptors [30, 43-49]. Each human Notch receptor homolog contains a variable number of epidermal growth factor (EGF) domains that compose the majority of the extracellular region. All Jagged and Delta-like ligands contain several EGF domains as well as an N-terminal Delta/Serrate/Lag-2 (DSL) domain [50, 51]. A 17 amino acid peptide derived from the DSL region of the Jagged1 ligand (amino acids #187-203) has been previously used to study Notch signaling [30, 52, 53]. Upon detailed study of the Notch1-Jagged1 interaction, Cordle et al. reported five critical residues on the Jagged1 ligand. These five residues are spread out over consecutive amino acids (#199-207) that overlap with the commercial 17-mer peptide, and are highly conserved among Notch ligands. In selecting peptide sequences for our Notch-targeting peptide, we consequently chose 17-mer and 9-mer peptides using amino acids 187-203 and 199-207, respectively. As the EGF1 and 2 domains are also considered important for Jagged1 ligand binding [50, 54], we also tested a 23-mer peptide from the EGF1 domain of human Jagged1. As

this peptide was shown to be less effective in blocking granulocyte colony-stimulating factor-induced differentiation than the 17-mer described above [52], it was our hope that this peptide may be able to interact with Notch receptors without stimulating Notch activity. Various peptides with reverse or scramble sequences were also evaluated in our studies, as detailed in Table A.1.

Peptides were synthesized by FMOC chemistry, by hand if composed of nine amino acids or on an ABI 433 peptide synthesizer if longer. Each was purified by reverse phase high performance liquid chromatography (RP-HPLC). Analytical runs of the final purified products were conducted for detection of a single peak, and correct molecular weights were confirmed by electrospray ionization mass spectroscopy. Representative results for the 17-mer peptide are shown in Figure A.1.

Not wanting to stimulate Notch signaling upon binding, we investigated the effect of Jagged1 peptides on Notch activity following incubation with Notch-expressing MDA-MB-231 breast cancer cells. To quantify Notch activity, MDA-MB-231 cells were transduced with a lentiviral vector containing either a pGreenFire1-Notch plasmid or a pGreenFire1-mCMV (negative control) plasmid. Cells were incubated with the Jagged1 peptides and a human Jagged1 disulfide-linked homodimer as a positive control. After six hours, Notch activation was quantified by luminescence using a Luciferase assay as shown in Figure A.2. As expected, luminescence was negligible in the mCMV cells. Evaluating luminescence signals in the MDA-MB-231 Notch cells, none of the Jagged1 peptides produced significantly different results when compared to non-treated cells. Comparable effects of peptide incubation were obtained in ZR-75-1 Notch and mCMV cells (data not shown).

After determining that Jagged1 peptides do not stimulate Notch activity in breast cancer cells, we sought to analyze the ability of peptides to target Notch receptors. We first considered examining the ability of the peptides to increase nanoparticle uptake in Notch-expressing MDA-MB-231 cells (non-transduced); H520 lung cancer cells with negligible Notch expression [55] were selected as a negative control. We desired to follow a similar experimental design as described in Chapter 4 using Living PEGylation [56], in which we had stably controlled the ratio of RGD targeting peptide onto laser-produced gold nanoparticles (AuNPs). However, in this previous design the RGD peptide was conjugated to the end of thiolated poly(ethylene glycol) (HS-PEG-RGD); this would not work here with our cysteine-containing peptides bearing thiol groups that could attach directly to the AuNP surface, as we would not be able to ensure the peptides would be presented at the free end of the PEG to enable receptor interaction. With some reservations about the design, we conducted a quick experiment using a slightly different approach to Living PEGylation: to first partially PEGylate laser-produced AuNPs from IMRA America (20 nm) with neutral PEG molecules ($HS\text{-}PEG_{5000}\text{-}OCH_3$), and then conjugate Jagged1 peptides directly to the AuNP surface before incubating with cells (2.5 nM AuNPs, 8 h). While higher Au uptake was observed in MDA-MB-231 cells than H520 control cells as expected, AuNPs containing Jagged1 peptides did not have increased cellular uptake compared to AuNPs bearing only PEG (data not shown). As we expected may happen, potential formulation issues, such as whether the larger PEG molecules could mask the smaller peptides and whether direct conjugation of the peptides to the AuNP surface via cysteine residues would affect the peptide conformation necessary for binding to Notch receptors [57], made it difficult to conclude whether our observations were true reflections of the peptide targeting abilities. Following this quick experiment, we decided to alter our approaches for future studies: 1) to study peptide

binding affinity via competition studies of labeled and unlabeled peptides [58, 59], and 2) to formulate targeted nanoparticles with thiol-containing peptides using specific chemistry to control peptide conjugation onto nanoparticles already coated with PEG molecules (HS-PEG-R, R = chemically reactive group for peptide attachment). The first study is described in the remainder of the work presented in this chapter. The second study formed the basis for the work presented in Chapter 5, in which "clickable" peptides were synthesized for attachment to PTT-mediating, AuNP-containing nanocomposites by azide-alkyne click chemistry.

For the work presented here, fluorescently-labeled versions of each peptide were synthesized for qualitative fluorescence imaging and quantitative flow cytometry following cellular incubation. Like the design of alkyne-peptides described in Chapter 5 (Scheme 5.3), two 6-aminohexanoic acid spacers were used to separate the peptide amino acids from the Fluoescein molecule at the N-terminus. Representative images from incubation of the fluorescent Jagged1 peptides with MDA-MB-231 and H520 cells are shown below for the 9-mer-FL peptide (Figure A.3A). In the H520 cell line, none of the fluorescent peptides showed increased staining compared to non-treated cells. In the MDA-MB-231 cell line the 9-mer-FL and 17-mer-FL showed the greatest increase in fluorescence in the FITC channel compared to non-treated cells, while the 23-mer-FL showed the least. Oddly, the scramble 9-mer-FL showed higher FITC fluorescence comparable to the 9-mer-FL and the 17-mer-FL peptides. Next, a competition study was performed with unlabeled peptides to distinguish specific versus non-specific peptide binding. Similar studies have been performed with either fluorescent or radio-labeled peptides. If binding is specific, pre-treatment with unlabeled peptides will block binding of labeled peptides. Representative images of MDA-MB-231 cells from incubation of the fluorescent Jagged1 peptides following pre-treatment with 100-fold concentrated unlabeled peptides are

shown below for the 9-mer-FL and 9-mer peptides (Figure A.3B). Appearing to be one of the best peptides, with less non-specific binding and a higher binding affinity relative to the others, the 9-mer-FL peptide was chosen for quantitative analysis via flow cytometry.

Competition studies at multiple peptide concentrations were repeated to obtain quantitative data via flow cytometry. Images of MDA-MB-231 cells from incubation of the fluorescent 9-mer following pre-treatment with 100-fold concentrated unlabeled 9-mer are shown below (Figure A.4). Pre-treatment with unlabeled 9-mer at 50-fold concentrations of fluorescent 9-mer was also performed in ZR-75-1, MCF7, and SUM159 breast cancer cells, all shown to have expression of multiple Notch receptors [60, 61]. In all four cell lines, fluorescence values increase proportionally with concentration of fluorescent 9-mer. Slightly higher values were observed in MCF-7 and ZR-75-1 cells than MDA-MB-231 and SUM159 cells (data not shown). However, pre-treatment with unlabeled peptide did not reduce the fluorescence signal in cells incubated with fluorescent peptide without pre-treatment. By evaluating multiple cell lines, successful demonstration of specific-binding was not limited by a particular Notch receptor homolog expression of a particular cell line. Consequently, our data suggest that the binding affinity of the Jagged1 peptides is low when presented as single peptides in cell culture medium and that the majority of binding observed is non-specific.

Several factors may influence ligand binding to Notch receptors. First, in canonical Notch signaling, the presented Notch ligand is attached to a neighboring cell rather than existing free in solution [32]. While the DSL domain of the Jagged1 ligand is considered the essential Notch-binding region, the EGF1 and EGF2 domains have been reported to be important for binding [50, 62]. (This may also be reflected in the fact that the Notch receptors exist in an autoinhibited state, and upon ligand binding a significant force is required to induce a

conformational change that exposes the site of the first enzymatic cleavage event in the negative regulatory region (NRR) [63].) When Shimizu et al. analyzed Notch2 binding with different truncations of mouse Jagged1, held in dimerized form by hIgG Fc fragment, they reported profoundly lower binding affinity for the truncation containing only the DSL domain compared to the truncation that also contained the EGF1 and EGF2 domains [54]. Second, it has been suggested that the DSL domain from which the Jagged1 17-mer peptide is derived may be stabilized by disulfide bonds, and that the high cysteine content of the 17-mer peptide may potentially result in aggregation and loss of biological activity given the fact that relatively high concentrations are required in *in vitro* studies [64]. Many studies conducted with Notch peptides have used concentrations of 10 μM or higher [30, 52-54], which may reduce peptide dissociation from the receptors. Third, as Jagged1-Notch binding is known to be calcium-dependent, elevated calcium levels may be beneficial; one group maintained cells in culture with 2 mM calcium for Jagged1 peptide studies [53]. Fourth, Fc fusion proteins in dimer form may benefit from a multivalent effect [65, 66]. Indeed, the commercially available human Jagged1 Fc fusion protein purchased for our Notch affinity studies exists in a disulfide-linked homodimer form [67]. It is possible that presenting the peptides on the surface of nanoparticles will result in a beneficial multivalent effect and significantly improve binding affinity due to simultaneous interactions with the cell surface [68, 69], at which point the potential to stimulate Notch activity may need to be reevaluated.

A.4 Conclusions

Various peptides derived from the DSL and EGF regions of the endogenous Notch ligand Jagged1 were evaluated for their ability to serve as targeting ligands for BCSCs expressing Notch receptors. Following synthesis and purification of peptides ranging in size from nine to 23 amino acids, the effect of peptide incubation on Notch activity was determined by a Luciferase assay following six hour incubation with Notch-expressing breast cancer cell lines (MDA-MB-231, ZR-75-1) transduced with a Notch reporter. None of the Jagged1 peptides caused a significant difference in the luminescence signal compared to non-treated cells, mitigating concerns of potential stimulation of Notch activity. Fluorescent forms of each peptide, with Fluorscein added to the N-terminus separated by two 6-aminohexanoic acid spacers, were also synthesized to determine peptide binding affinity for Notch receptors. First, fluorescence imaging was conducted of MDA-MB-231 cells and negative control H520 cells incubated with fluorescent peptides. Next, fluorescence imaging was conducted following a competition study in MDA-MB-231 cells, which were incubated with fluorescent peptides following pre-treatment with unlabeled peptide to assess specificity of binding. In both experiments the nine amino acid peptide appeared to have favorable binding properties over the other peptides, with higher fluorescence observed in the first imaging study and lower non-specific fluorescence following pre-treatment with unlabeled peptide in the competition study. Competition studies with the 9-mer and fluorescent 9-mer were then repeated in four Notch-expressing breast cancer cell lines for quantitative analysis via flow cytometry. As pre-treatment with unlabeled 9-mer did not affect the fluorescence signal compared to cells incubated only with fluorescent 9-mer, it was determined the majority of binding is non-specific. Our data suggest that Jagged1 peptides, when incubated freely in solution, have low binding affinities for Notch receptors, requiring

relatively high concentrations for *in vitro* studies. Presentation of the Jagged1 peptides on a nanoparticle surface, enabling a multivalent effect in which simultaneous interactions with the cell surface occur, may improve peptide binding affinity and potentially enhance uptake of nanoparticles by Notch-expressing cells, meriting further study.

A.5 Materials and Methods

Synthesis of peptides: Unlabeled and fluorescently-labeled Jagged1 peptides were produced via FMOC solid phase synthesis using chlorotrityl resin as the solid support. Those composed of nine amino acids were synthesized manually; 17-mer and 23-mer peptides were produced on an ABI 433 peptide synthesizer. Similar to synthesis of the alkyne-peptide in Chapter 5, fluorescent peptides were labeled at the N-terminus as follows: two 6-aminohexanoic acid spacers were added via FMOC chemistry, followed by NHS-Fluoescein (ThermoScientific) before cleavage from the resin. Purification of the peptides was performed via reverse phase high performance liquid chromatography (RP-HPLC) with a C-18 column (Sunfire, 19 mm × 150 mm, 5 μm), and electrospray ionization mass spectroscopy confirmed the correct mass.

Cell culture: MDA-MB-231, ZR-75-1, MCF-7, and SUM159 breast cancer cells were grown as adherent monolayers incubated at 37 °C with 5% CO_2. For MDA-MB-231 and ZR-75-1, RPMI medium was supplemented with 10% fetal bovine serum and 1% antibiotic-antimycotic. For MCF-7 cells, DMEM was medium supplemented with 10% fetal bovine serum and 1% antibiotic-antimycotic. For SUM159 cells, Ham's F12 medium was supplemented with 5% fetal bovine serum, 1% antibiotic-antimycotic, 5 μg/mL insulin, 1 μg/mL hydrocortisone, and 4 μg/mL gentamicin.

Notch activity studies: MDA-MB-231 and ZR-75-1 cells with Notch activity reporters were a gift from the Wicha laboratory and were generated as previously described [70]. Briefly, MDA-MB-231 cells were transduced with a lentiviral vector containing either a pGreenFire1 (pGF1)-Notch or a pGF1-mCMV (negative control) plasmid from System Biosciences. The pGreenFire1 plasmid enables reporter activity through both green fluorescent protein (GFP) and Luciferase. Cells were incubated with the Jagged1 peptides (0.5 μM) for six hours (n=3), after which Notch activation was quantified using a standard Luciferase assay (Promega) and a BioTek micro-plate reader (Synergy 2). Human Jagged1 Fc chimera protein (R&D Systems) was used as a positive control.

In vitro fluorescence imaging: For initial images of binding of fluorescent Jagged1 peptides, MDA-MB-231 and H250 cells were incubated with peptides (1 μM) for 2 h. Incubation was performed on ice to prevent receptor internalization upon ligand binding. Cells were then washed with PBS, fixed, and stained with DAPI for cell viability. Binding of Fluorescein to cells was viewed through the FITC channel; nuclear DAPI staining was viewed through the DAPI channel. For competition studies in MDA-MB-231 cells, unlabeled Jagged1 (100 μM) peptides were added for 1 h pre-treatment, cells were washed with PBS, and fluorescent Jagged1 peptides were added for 2 h. Cells were then washed with PBS, fixed, and stained with DAPI before imaging. Samples were imaged on an Olympus BX-51 fluorescence microscope.

In vitro flow cytometry: MDA-MB-231 cells were collected using trypsin, washed, and suspended for incubation with peptides on ice. Cells were pre-treated with unlabeled Jagged1 peptides (1000, 100, or 1 μM for 1 h) at concentrations 100-fold higher than fluorescent Jagged1 peptides (10, 1, or 0.1 μM for 2 h). This process was repeated for incubation with ZR-75-1,

MCF7, and SUM159 cells except pre-treatment concentrations of unlabeled 9-mer were 50-fold higher than fluorescent 9-mer. Samples were run on a Beckman Coulter Quanta SC and analyzed with Attune software.

Statistical Analysis: Data are represented as mean ± standard deviation. The significance values of data sets with two groups were calculated by a student's t-test. A $p < 0.05$ was considered statistically significant.

A.6 Figures

Table A.1. List of synthesized peptides with their molecular weight (MW), amino acid sequence, and the Jagged1 domain from which they originate.

Peptide	MW (g/mol)	Sequence	Jagged1 Domain
17-mer	2107	CDDYYYGFGCNKFCRPR	DSL
23-mer	2484	CRQGCSPKHGSCKLPGDCRCQYG	EGF1
Reverse 23-mer	2484	GYQCRCDGPLKCSGHKPSCGQRC	EGF1
9-mer	1202	FCRPRDDFF	DSL
Reverse 9-mer	1202	FFDDRPRCF	DSL
Scramble 9-mer	1202	DRFCDRFPF	DSL

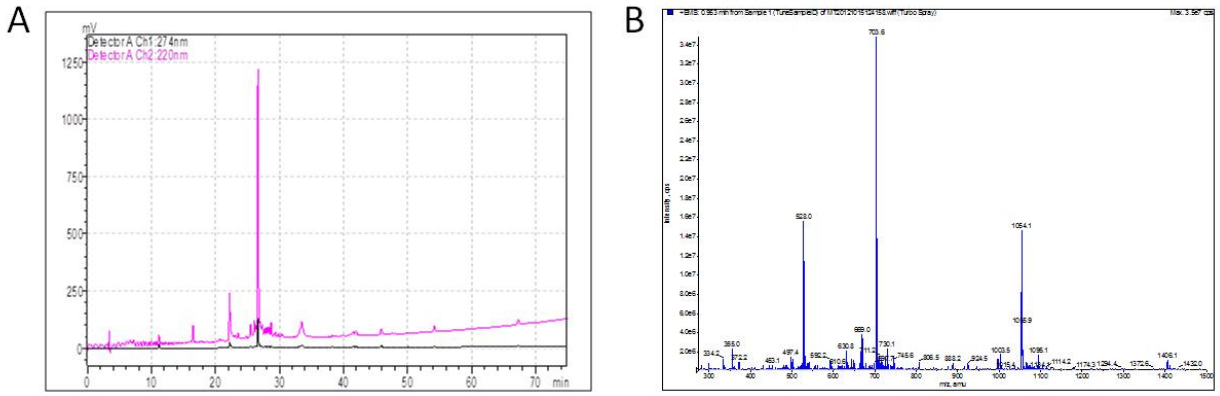

Figure A.1. (A) Single peak from the analytical run of the purified 17-mer (MW ~2107 g/mol). (B) Confirmation of the correct mass by electrospray ionization (ESI) mass spectroscopy, revealing the +2 peak at ~1054 m/z, +3 peak at ~703 m/z, and +4 peak at ~528 m/z.

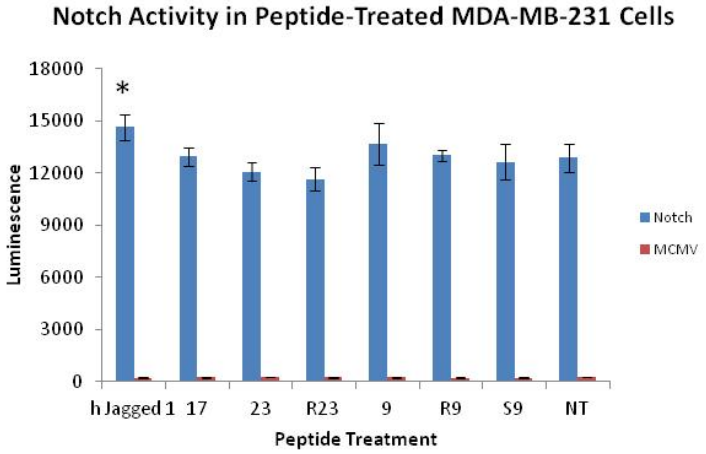

Figure A.2. Notch reporter activity quantified via Luciferase in transduced MDA-MB-231 breast cancer cells following treatment with Jagged1 peptides (0.5 μM). Notch = pGF1-Notch plasmid, MCMV = pGF1-mCMV plasmid. *$p < 0.05$.

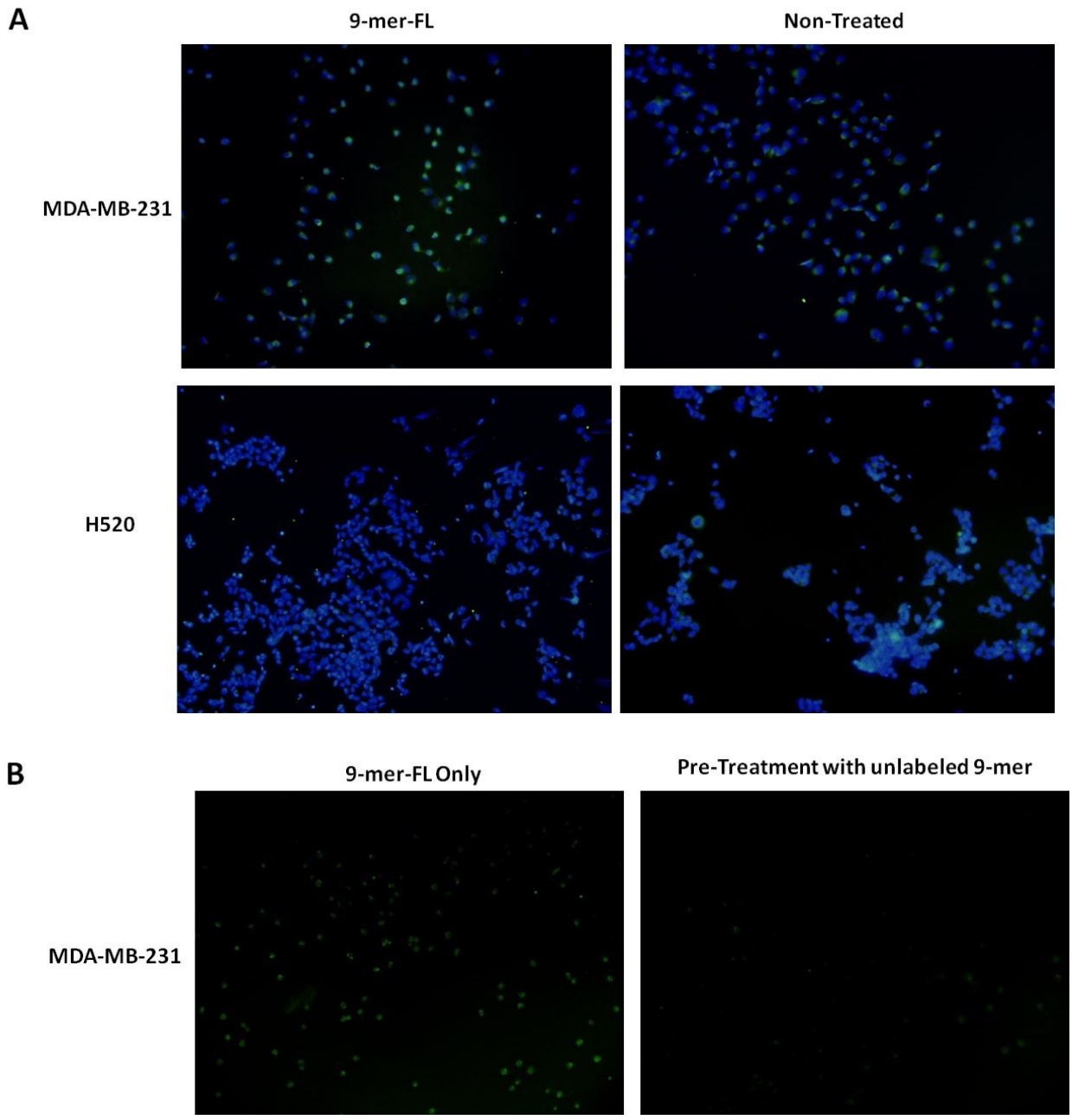

Figure A.3. (A) Fluorescence images (FITC/DAPI overlays) of 9-mer-FL peptide incubated with MDA-MB-231 Notch-expressing cells and H520 negative control cells. (B) Fluorescence images (FITC) of competition of fluorescent and unlabeled 9-mer peptides to evaluate specific binding in MDA-MB-231 cells.

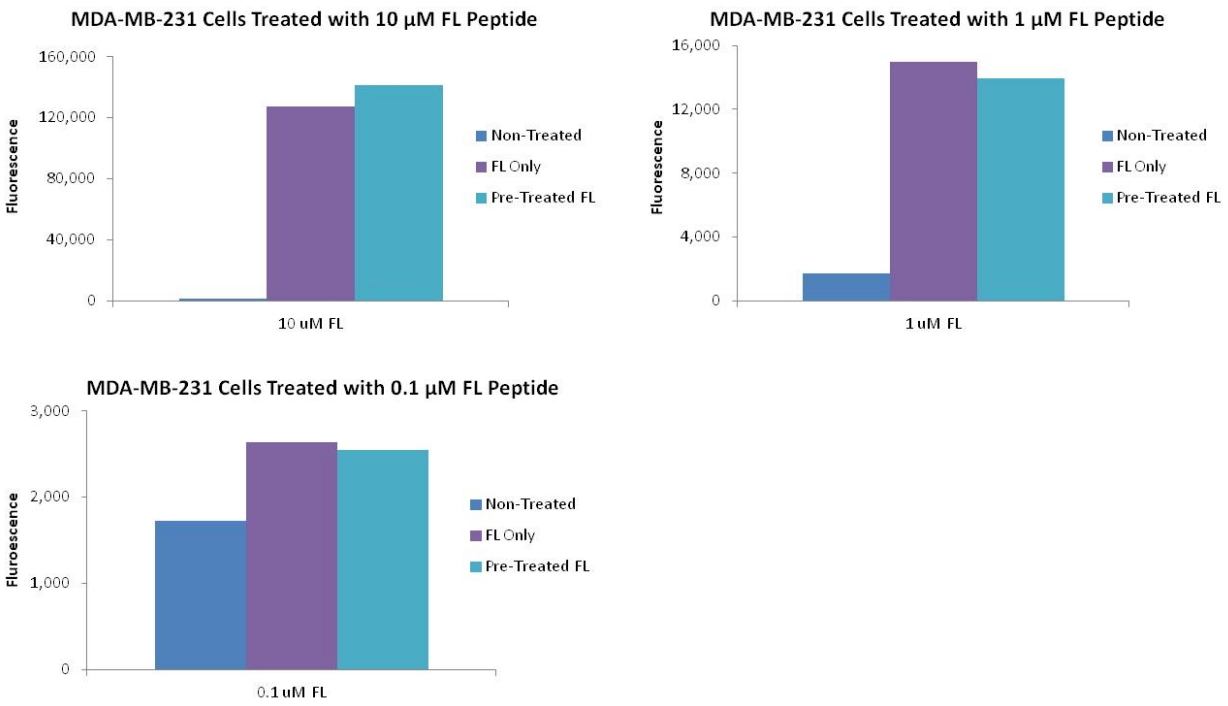

Figure A.4. Flow cytometry of MDA-MB-231 cells incubated with 9-mer-FL peptide at 10, 1, and 0.1 µM concentrations, with and without pre-treatment with unlabeled 9-mer (1000, 100, 10 µM) to evaluate specific binding.

A.7 Acknowledgements

Others who contributed to this work include Liang Zhang[2], Rebecca A. Reed[1], Xu Ran[3], Luo Wang[4], Nicholas O. Stevers[1], Hongwei Chen[1], and Greg M. Thurber[2], Shaomeng Wang[3], Max S. Wicha[4], and Duxin Sun[1] in the Pharmaceutical Sciences department at the University of Michigan. I would also like to thank Hacer Karatas[3], Ting Zhao[1], Ruijuan Luo[1], and Khaled A. Hassan[4] for their assistance and thoughtful input. This work was supported in part by the NIH Pharmacological Sciences Training Program (H. Paholak), the American Foundation for Pharmaceutical Education Pre-Doctoral Fellowship (H. Paholak).

[1]Pharmaceutical Sciences Department, University of Michigan
[2]Chemical Engineering Department, University of Michigan

[3]Medicinal Chemistry Department, University of Michigan
[4]Department of Internal Medicine, University of Michigan

A.8 References

1. Bonnet, D. and J.E. Dick, *Human acute myeloid leukemia is organized as a hierarchy that originates from a primitive hematopoietic cell.* Nat Med, 1997. **3**(7): p. 730-7.

2. Al-Hajj, M., et al., *Prospective identification of tumorigenic breast cancer cells.* Proc Natl Acad Sci U S A, 2003. **100**(7): p. 3983-8.

3. Singh, S.K., et al., *Identification of a cancer stem cell in human brain tumors.* Cancer Res, 2003. **63**(18): p. 5821-8.

4. Collins, A.T., et al., *Prospective identification of tumorigenic prostate cancer stem cells.* Cancer Res, 2005. **65**(23): p. 10946-51.

5. Li, C., et al., *Identification of pancreatic cancer stem cells.* Cancer Res, 2007. **67**(3): p. 1030-7.

6. Prince, M.E., et al., *Identification of a subpopulation of cells with cancer stem cell properties in head and neck squamous cell carcinoma.* Proc Natl Acad Sci U S A, 2007. **104**(3): p. 973-8.

7. Dontu, G., et al., *Stem cells in normal breast development and breast cancer.* Cell Prolif, 2003. **36 Suppl 1**: p. 59-72.

8. Ginestier, C., et al., *ALDH1 is a marker of normal and malignant human mammary stem cells and a predictor of poor clinical outcome.* Cell Stem Cell, 2007. **1**(5): p. 555-67.

9. Conley, S.J., et al., *Antiangiogenic agents increase breast cancer stem cells via the generation of tumor hypoxia.* Proc Natl Acad Sci U S A, 2012. **109**(8): p. 2784-9.

10. Dontu, G., et al., *In vitro propagation and transcriptional profiling of human mammary stem/progenitor cells.* Genes Dev, 2003. **17**(10): p. 1253-70.

11. Charafe-Jauffret, E., et al., *Breast cancer cell lines contain functional cancer stem cells with metastatic capacity and a distinct molecular signature.* Cancer Res, 2009. **69**(4): p. 1302-13.

12. Ginestier, C., et al., *CXCR1 blockade selectively targets human breast cancer stem cells in vitro and in xenografts.* J Clin Invest, 2010. **120**(2): p. 485-97.

13. Liu, S., et al., *Breast cancer stem cells transition between epithelial and mesenchymal states reflective of their normal counterparts.* Stem Cell Reports, 2014. **2**(1): p. 78-91.

14. Korkaya, H., et al., *Activation of an IL6 inflammatory loop mediates trastuzumab resistance in HER2+ breast cancer by expanding the cancer stem cell population.* Mol Cell, 2012. **47**(4): p. 570-84.

15. Liu, S., et al., *Hedgehog signaling and Bmi-1 regulate self-renewal of normal and malignant human mammary stem cells.* Cancer Res, 2006. **66**(12): p. 6063-71.

16. Wicha, M.S., S. Liu, and G. Dontu, *Cancer stem cells: an old idea--a paradigm shift.* Cancer Res, 2006. **66**(4): p. 1883-90; discussion 1895-6.

17. Reya, T., et al., *Stem cells, cancer, and cancer stem cells.* Nature, 2001. **414**(6859): p. 105-11.

18. Liao, W.T., et al., *Metastatic cancer stem cells: from the concept to therapeutics.* Am J Stem Cells, 2014. **3**(2): p. 46-62.

19. Li, F., et al., *Beyond tumorigenesis: cancer stem cells in metastasis.* Cell Res, 2007. **17**(1): p. 3-14.

20. Atkinson, R.L., et al., *Thermal enhancement with optically activated gold nanoshells sensitizes breast cancer stem cells to radiation therapy.* Sci Transl Med, 2010. **2**(55): p. 55ra79.

21. Creighton, C.J., et al., *Residual breast cancers after conventional therapy display mesenchymal as well as tumor-initiating features.* Proc Natl Acad Sci U S A, 2009. **106**(33): p. 13820-5.

22. Bao, S., et al., *Glioma stem cells promote radioresistance by preferential activation of the DNA damage response.* Nature, 2006. **444**(7120): p. 756-60.

23. Logue, J.S. and D.K. Morrison, *Complexity in the signaling network: insights from the use of targeted inhibitors in cancer therapy.* Genes Dev, 2012. **26**(7): p. 641-50.

24. Korkaya, H. and M.S. Wicha, *Selective targeting of cancer stem cells: a new concept in cancer therapeutics.* BioDrugs, 2007. **21**(5): p. 299-310.

25. Zeng, W.G., et al., *[All-trans retinoic acid effectively inhibits breast cancer stem cells growth in vitro].* Zhonghua Zhong Liu Za Zhi, 2013. **35**(2): p. 89-93.

26. Degos, L. and Z.Y. Wang, *All trans retinoic acid in acute promyelocytic leukemia.* Oncogene, 2001. **20**(49): p. 7140-5.

27. Liu, S. and M.S. Wicha, *Targeting breast cancer stem cells.* J Clin Oncol, 2010. **28**(25): p. 4006-12.

28. Takebe, N., et al., *Targeting cancer stem cells by inhibiting Wnt, Notch, and Hedgehog pathways.* Nat Rev Clin Oncol, 2011. **8**(2): p. 97-106.

29. Takebe, N., et al., *Targeting Notch, Hedgehog, and Wnt pathways in cancer stem cells: clinical update.* Nat Rev Clin Oncol, 2015. **12**(8): p. 445-64.

30. Dontu, G., et al., *Role of Notch signaling in cell-fate determination of human mammary stem/progenitor cells.* Breast Cancer Res, 2004. **6**(6): p. R605-15.

31. Garvalov, B.K. and T. Acker, *Cancer stem cells: a new framework for the design of tumor therapies.* J Mol Med (Berl), 2011. **89**(2): p. 95-107.

32. Fortini, M.E., *Notch signaling: the core pathway and its posttranslational regulation.* Dev Cell, 2009. **16**(5): p. 633-47.

33. McDermott, S.P. and M.S. Wicha, *Targeting breast cancer stem cells.* Mol Oncol, 2010. **4**(5): p. 404-19.

34. Korkaya, H., et al., *Regulation of mammary stem/progenitor cells by PTEN/Akt/beta-catenin signaling.* PLoS Biol, 2009. **7**(6): p. e1000121.

35. Burke, A.R., et al., *The resistance of breast cancer stem cells to conventional hyperthermia and their sensitivity to nanoparticle-mediated photothermal therapy.* Biomaterials, 2012. **33**(10): p. 2961-70.

36. Huang, H.C., K. Rege, and J.J. Heys, *Spatiotemporal temperature distribution and cancer cell death in response to extracellular hyperthermia induced by gold nanorods.* ACS Nano, 2010. **4**(5): p. 2892-900.

37. Lee, S.E., et al., *Remote optical switch for localized and selective control of gene interference.* Nano Lett, 2009. **9**(2): p. 562-70.

38. Sharma, A., et al., *A monoclonal antibody against human Notch1 ligand-binding domain depletes subpopulation of putative breast cancer stem-like cells.* Mol Cancer Ther, 2012. **11**(1): p. 77-86.

39. *OncoMed Pharmaceuticals Advances Two Notch Pathway Product Candidates in Clinical Development.* FierceBiotech.

40. Bao, B., et al., *Notch-1 induces epithelial-mesenchymal transition consistent with cancer stem cell phenotype in pancreatic cancer cells.* Cancer Lett, 2011. **307**(1): p. 26-36.

41. Hovinga, K.E., et al., *Inhibition of notch signaling in glioblastoma targets cancer stem cells via an endothelial cell intermediate.* Stem Cells, 2010. **28**(6): p. 1019-29.

42. McAuliffe, S.M., et al., *Targeting Notch, a key pathway for ovarian cancer stem cells, sensitizes tumors to platinum therapy.* Proc Natl Acad Sci U S A, 2012. **109**(43): p. E2939-48.

43. Chu, D., et al., *Notch1 and Notch2 have opposite prognostic effects on patients with colorectal cancer.* Ann Oncol, 2011. **22**(11): p. 2440-7.

44. Graziani, I., et al., *Opposite effects of Notch-1 and Notch-2 on mesothelioma cell survival under hypoxia are exerted through the Akt pathway.* Cancer Res, 2008. **68**(23): p. 9678-85.

45. Touplikioti, P.C., Dafni;nZiouti, Fani, Koubanaki, Melanie; Haitoglou, Konstantinos; Kouvatseas, George; Papazisis, Konstantinos T., *Expression of Notch Receptors in Primary Breast Cancer and Correlation with Pathological Features.* Clin Exp Pharmacol, 2012. **2**(1).

46. Parr, C., G. Watkins, and W.G. Jiang, *The possible correlation of Notch-1 and Notch-2 with clinical outcome and tumour clinicopathological parameters in human breast cancer.* Int J Mol Med, 2004. **14**(5): p. 779-86.

47. Speiser, J., et al., *Notch-1 and Notch-4 biomarker expression in triple-negative breast cancer.* Int J Surg Pathol, 2012. **20**(2): p. 139-45.

48. Clementz, A.G., et al., *NOTCH-1 and NOTCH-4 are novel gene targets of PEA3 in breast cancer: novel therapeutic implications.* Breast Cancer Res, 2011. **13**(3): p. R63.

49. Callahan, R. and A. Raafat, *Notch signaling in mammary gland tumorigenesis.* J Mammary Gland Biol Neoplasia, 2001. **6**(1): p. 23-36.

50. Cordle, J., et al., *A conserved face of the Jagged/Serrate DSL domain is involved in Notch trans-activation and cis-inhibition.* Nat Struct Mol Biol, 2008. **15**(8): p. 849-57.

51. Pintar, A., et al., *Exon 6 of human JAG1 encodes a conserved structural unit.* BMC Struct Biol, 2009. **9**: p. 43.

52. Li, L., et al., *The human homolog of rat Jagged1 expressed by marrow stroma inhibits differentiation of 32D cells through interaction with Notch1.* Immunity, 1998. **8**(1): p. 43-55.

53. Nickoloff, B.J., et al., *Jagged-1 mediated activation of notch signaling induces complete maturation of human keratinocytes through NF-kappaB and PPARgamma.* Cell Death Differ, 2002. **9**(8): p. 842-55.

54. Shimizu, K., et al., *Mouse jagged1 physically interacts with notch2 and other notch receptors. Assessment by quantitative methods.* J Biol Chem, 1999. **274**(46): p. 32961-9.

55. Baumgart, A., et al., *ADAM17 regulates epidermal growth factor receptor expression through the activation of Notch1 in non-small cell lung cancer.* Cancer Res, 2010. **70**(13): p. 5368-78.

56. Chen, H.W., et al., *Living' PEGylation on gold nanoparticles to optimize cancer cell uptake by controlling targeting ligand and charge densities.* Nanotechnology, 2013. **24**(35).

57. Fu, P., et al., *Synthesis, conformation, receptor binding and biological activities of monobiotinylated human insulin-like peptide 3.* J Pept Res, 2004. **63**(2): p. 91-8.

58. Reiner, T., et al., *Accurate measurement of pancreatic islet beta-cell mass using a second-generation fluorescent exendin-4 analog.* Proc Natl Acad Sci U S A, 2011. **108**(31): p. 12815-20.

59. Bunzow, J.R., et al., *Characterization and distribution of a cloned rat mu-opioid receptor.* J Neurochem, 1995. **64**(1): p. 14-24.

60. Chen, J., et al., *Hypoxia potentiates Notch signaling in breast cancer leading to decreased E-cadherin expression and increased cell migration and invasion.* Br J Cancer, 2010. **102**(2): p. 351-60.

61. D'Angelo, R.C., et al., *Notch reporter activity in breast cancer cell lines identifies a subset of cells with stem cell activity.* Mol Cancer Ther, 2015. **14**(3): p. 779-87.

62. Rebay, I., et al., *Specific EGF repeats of Notch mediate interactions with Delta and Serrate: implications for Notch as a multifunctional receptor.* Cell, 1991. **67**(4): p. 687-99.

63. Gordon, W.R., et al., *Structural basis for autoinhibition of Notch.* Nat Struct Mol Biol, 2007. **14**(4): p. 295-300.

64. Zlobin, A., M. Jang, and L. Miele, *Toward the rational design of cell fate modifiers: notch signaling as a target for novel biopharmaceuticals.* Curr Pharm Biotechnol, 2000. **1**(1): p. 83-106.

65. Czajkowsky, D.M., et al., *Fc-fusion proteins: new developments and future perspectives.* EMBO Mol Med, 2012. **4**(10): p. 1015-28.

66. Mammen, M.C., SK; Whitesides, GM, *Polyvalent interactions in biological systems: Implications for design and use of multivalent ligands and inhibitors.* ANGEWANDTE CHEMIE-INTERNATIONAL EDITION, 1998. **37**(20): p. 2755-2794.

67. *Recombinant Human Jagged 1 Fc Chimera.* R&D Systems, 2012.

68. Cai, W., et al., *Applications of gold nanoparticles in cancer nanotechnology.* Nanotechnol Sci Appl, 2008. **2008**(1).

69. Montet, X., et al., *Multivalent effects of RGD peptides obtained by nanoparticle display.* J Med Chem, 2006. **49**(20): p. 6087-93.

70. Hassan, K.A., et al., *Notch pathway activity identifies cells with cancer stem cell-like properties and correlates with worse survival in lung adenocarcinoma.* Clin Cancer Res, 2013. **19**(8): p. 1972-80.